Domain wall and skyrmion dynamics in perpendicular magnetic anisotropic thin films

By

Brindaban Ojha

Enrolment No. PHYS11201704011

National Institute of Science Education and Research, Bhubaneswar

A thesis submitted to the

Board of Studies in Physical Sciences

In partial fulfillment of requirements

for the Degree of

DOCTOR OF PHILOSOPHY

of

HOMI BHABHA NATIONAL INSTITUTE

May 2024

Homi Bhabha National Institute[1]

Recommendations of the Viva Voce Committee

As members of the Viva Voce Committee, we certify that we have read the dissertation prepared by **Brindaban Ojha** entitled **"Domain wall and skyrmion dynamics in perpendicular magnetic anisotropic thin films"** and recommend that it may be accepted as fulfilling the thesis requirement for the award of Degree of Doctor of Philosophy.

Chairman - Prof. Bedangadas Mohanty	15/5/2024
Guide / Convener - Prof. Subhankar Bedanta	15/05/2024
Co-guide - Name & Signature with date (if any)	
Examiner - Prof. Chandrasekhar Murapaka	15/05/2024
Member 1- Dr. Ajay Kumar Nayak	15/05/2024
Member 2- Dr. Ashis Kumar Nandy	15/05/2024
Member 3- Dr. Debakanta Samal	

Final approval and acceptance of this thesis is contingent upon the candidate's submission of the final copies of the thesis to HBNI.

I/We hereby certify that I/we have read this thesis prepared under my/our direction and recommend that it may be accepted as fulfilling the thesis requirement.

Date: 15/05/2024

Place: Jatni

Signature
Co-guide (if any)

Signature 15/05/2024
Guide

[1] This page is to be included only for final submission after successful completion of viva voce.

STATEMENT BY AUTHOR

This dissertation has been submitted in partial fulfillment of requirements for an advanced degree at Homi Bhabha National Institute (HBNI) and is deposited in the library to be made available to borrowers under rules of the HBNI.

Brief quotations from this dissertation are allowable without special permission, provided that accurate acknowledgement of source is made. Requests for permission for extended quotation from or reproduction of this manuscript in whole or in part may be granted by the Competent Authority of HBNI when in his or her judgment the proposed use of the material is in the interests of scholarship. In all other instances, however, permission must be obtained from the author.

Brindaban Ojha

DECLARATION

I, hereby declare that the investigation presented in the thesis has been carried out by me. The work is original and has not been submitted earlier as a whole or in part for a degree / diploma at this or any other Institution / University.

Brindaban Ojha

CERTIFICATION ON ACADEMIC INTEGRITY

Undertaking by the Student:

1. I, **Brindaban Ojha**, HBNI Enrolment No. **PHYS11201704011** hereby undertake that the Thesis, titled "**Domain wall and skyrmion dynamics in perpendicular magnetic anisotropic thin films**" is prepared by me and is the original work undertaken by me.
2. I also hereby undertake that this document has been duly checked through a plagiarism detection tool and the document is found to be plagiarism free as per the guidelines of the Institute/UGC.

3. I am aware and undertake that if plagiarism is detected in my thesis at any stage in the future, suitablepenalty will be imposed as applicable as per the guidelines of the Institute/UGC.

Brindaban Ojha
16.05.24
Signature of the Student with date

Endorsed by the Thesis Supervisor:

I certify that the thesis written by the Researcher is plagiarism free as mentioned above by the student.

Subhankar Bedanta 16/05/2024.
Signature of the Thesis Supervisor with date

Name: Prof. Subhankar Bedanta
Designation: Professor
Department/ Centre: School of Physical Sciences
Name of the CI/ OC: National Institute of Science Education and Research, Bhubaneshwar

List of Publications arising from the thesis

Journal

1. [#] "*Driving skyrmions with low threshold current density in Pt/CoFeB thin film*", **B. Ojha*,** S. Mallick*, S. Panigrahy, M. Sharma, A. Thiaville, S. Rohart and S. Bedanta, Physica Scripta **(2023)** 98, 035819**.**

2. [#] "*Unusual domain wall motion in the vicinity of the depinning field in a Pt/CoFeB/MgO film*" **B. Ojha,** B. B. Singh, M. Sharma, S. Mallick, V. Jeudy, A. Thiaville, S. Rohart and S. Bedanta, Applied Physics A **(2023)** 129 (10), 688.

Communicated

1. [#] "*Impact of Dzyaloshinskii–Moriya interaction and anisotropy on topological Hall effect*", **B. Ojha**. S. Mohanty and S. Bedanta, (submitted), (https://arxiv.org/abs/2405.05361v1).

Manuscript in preparation

1. [#] "*Effect of Re insertion on domain wall dynamics and interfacial Dzyaloshinskii-Moriya interactions*", **B. Ojha** and S. Bedanta *et al.*

2. [#] "*Field induced evolution of domain structures in Ta/[Pt/Co/Ru]$_7$/Pt thin films*", **B. Ojha** and S. Bedanta *et al.*

[#]Publications related to the thesis

Others

1. "*Observation of Topological Hall Effect and Skyrmions in Pt/Co/Ir/Co/Pt System*", S. Mohanty, **B. Ojha**, and S. Bedanta, Mater. Res. Express (**2024**) 11, 046406.

2. "*Study of domain wall dynamics in Pt/Co/Pt ultrathin films*", M. Sharma, **B. Ojha**, S. Mohanty, S. Pütter and S. Bedanta, Indian J. Phys. (**2024**) 1-7.

3. "*Emergence of sizeable interfacial Dzyaloshinskii-Moriya interaction at cobalt/fullerene interface*", E. Pandey, **B. Ojha**, and S. Bedanta, Physical Review Applied **(2023)** 19, 044013.

4. "*Device geometry dependent deterministic skyrmion generation from a skyrmionium*", A. Dash, **B. Ojha**, S. Mohanty, A. K. Moharana, and S. Bedanta, Nanotechnology **(2023)** 34, 185001.

5. "*Effect of fullerene on the anisotropy, domain size and relaxation of a perpendicularly magnetized Pt/Co/C_{60}/Pt system*", P. Sharangi, A. Mukhopadhyaya, S. Mallik, E. Pandey, **B. Ojha**, Md E. Ali, and S. Bedanta, Journal of Materials Chemistry C **(2022)** 10, 17236**.**

6. "*Magnetization reversal and domain structures in perpendicular synthetic antiferromagnets prepared on rigid and flexible Substrates*", S. Mohanty, M. Sharma, A. K. Moharana, **B. Ojha**, E. Pandey,B. B. Singh, and S. Bedanta, The Journal of The Minerals, Metals & Materials Society **(2022)** 74, 2319.

7. "*Effect of random anisotropy in stabilization of skyrmions and antiskyrmions*", G. Pradhan, **B. Ojha**, and S. Bedanta, Journal of Magnetism and Magnetic Materials **(2021)** 528, 167805.

Brindaban Ojha

Dedicated to my parents

ACKNOWLEDGEMENTS

I would like to express my heartfelt gratitude to my PhD supervisor, Prof. Subhankar Bedanta, for his assistance in all facets of my PhD journey. Without him, this thesis would not have been possible. Initially, I was really driven to work in magnetism, which got accelerated when he assigned me the fascinating topic of domain and skyrmion dynamics for my PhD research. His vast knowledge of magnetism and domain wall dynamics has greatly aided my understanding of the topic and raised the ability of doing good work. His continual support and assistance helped me learn how to identify a research problem, what feasible solutions exist, and how to implement them. His valuable comments, critiques, and suggestions were always helpful in improving the quality of the work. He also guided to write research papers in a concise manner while emphasizing the motive and underlying physics. Throughout my PhD, I immensely enjoyed his company at numerous academic, non-academic events and in various festivals. Without his consistent assistance and encouragement, I would not have been able to complete my research work. I will be eternally grateful for all of his advice and guidance, which helped to shine as a research scholar.

In addition, I would like to express my gratitude to the chairman of my thesis monitoring committee (TMC), Prof. Bedangadas Mohanty, and the other TMC members, Dr. Ajaya Kumar Nayak, Dr. Ashis Kumar Nandy, and Dr. Debakanta Samal for their timely evaluation, critical comments and suggestions which improved my understanding and helped me to complete the research work well.

I sincerely thank Prof. André Thiaville, Prof. Stanislas Rohart, and Prof. Vincent Jeudy from Université Paris-Saclay, CNRS-UMR, France, for their immense help with various experimental facilities, analysing the obtained results and suggestions to conclude the work done on domain and skyrmions dynamics.

I also sincerely thank Dr. Ashish Kumar Nandy (SPS-NISER) and Dr. Ritwik Das (ISM-Dhanbad) for their theoretical support and insightful remarks to understand the experimental result on chiral damping topic.

I also would like to thank all my collaborators Dr. Braj Bhushan Singh, Dr. Sougata Mallick, Dr. Sujit Panigrahy, Dr. Minaxi Sharma and Mr. Suvadip Ghosh for their valuable contribution in the experimental, theoretical work and suggestions regarding the research work.

I would like to express my sincere thanks to my collaborators, my senior and lab member Dr. Sougata Mallick. To me, he is like my elder brother. He helps me to understand the basics of the topics, in measurements and many ways. In particular, his help in making devices and subsequently MFM measurements to study the skyrmion dynamics is highly appreciated. He always gave me helpful advice in both my academic and daily life.

Further, I would like to thank my all lab members, Dr. Sougata Mallick, Dr. Srijani Mallik, Dr. Thiruvengadam Vijayabaskaran, Dr. Sagarika Nayak and Dr. Purbasha Sharangi for assisting me in understanding the basics of magnetism and the instrumental facilities available at NISER. I also thank Dr. Pushpendra Gupta, Mrs. Esita Pandey, Mr. Shaktiranjan Mohanty, Mr. Abhisek Mishra, Ms. Bhuvneshwari Sharma for their continuous support in various experiments, simulations, and analyses whenever needed. I also thank my other lab mates, Dr. Palash Kumar Manna, Dr. Anupama Swain, Dr. Bibhuti Bhushan Jena, Dr. Antarjami Sahoo, and Dr. Koustuv Roy for the numerous important discussions on a variety of topics. I also thank all my juniors Mr. Kshitij Singh Rathore, Ms. Swayang Priya Mahanta, and Ms. Rupalipriyadarsini Chhatoi for their help in many academic and non-academic work.

I am thankful to and fortunate enough to get constant encouragement, support, and cooperation from my best friend, lab mate and wife Mrs. Esita Pandey. She was always there for me in my difficult phases and she is the first person with whom I have shared all my problems and achievements. All our fruitful discussion helped a lot to enhance my understanding about the topic and improve my research skill. It would not be possible to complete the thesis work without her presence and support.

And finally, I would want to express my heartfelt gratitude to my parents, Mr. Pulin Bihari Ojha and Mrs. Gouri Rani Ojha, for their unwavering love, and support throughout this long trip. I also want to thank my sisters (Malini, Madhabi, Madhuri, Manasi) for being there always for me and my family

which helped me to continue my research carrier. I also extend my heartfelt thanks to my brother-in-law (Narayan and Rajat) for taking care of my family whenever any difficult time arises. Their presence and support towards my family helped me a lot to stay focused on my research work. I also would like to express my heartfelt gratitude to my father-in-law and mother in-law for their unwavering support during this journey. I am also grateful to have my dearest friends (Suman and Kaushik) beside me during different phases of this journey.

I sincerely acknowledge SPS-NISER, CIS-NISER, DAE, Govt. of India, Indo-French collaborative project (supported by CEFIPRA and the French National Research Agency), DST-Nanomission, DST-SERB and NFFA-Europe for providing the experimental facilities and research funding to carry the experimental work presented in my thesis.

CONTENTS

Summary

Perpendicular magnetic anisotropic thin films have been immensely investigated in the last few decades due to higher thermal stability and higher storage capacity. It has also drawn attraction on magnetic optic recording medium, various types of spintronic devices such as magnetic sensors, magnetoresistive random access memories (MRAM), high power magnetic oscillators, etc. In the case of thin film, the interfacial orbital hybridization of non-magnetic metal and ferromagnet (FM) promotes perpendicular magnetic anisotropy (PMA). Increasing the thickness of FM, the easy axis of thin films can be switched from out-of-plane to in-plane direction and above a critical thickness of FM, the 'spin reorientation transition' (SRT) occurs. A thin film with a low thickness of FM (far from SRT) exhibits square shaped out-of-plane hysteresis loop where PMA is much stronger than in-plane anisotropy. However, near SRT, PMA reduced in a film and a low remanence slanted hysteresis loop has been observed. Depending upon the strength of PMA, a magnetic thin film exhibits various types of domain structures. For a thin film with high PMA strength, i.e. Ku > Kd, circular bubble domains have been observed, where Ku and Kd are the uniaxial anisotropy density and demagnetization energy density, respectively. However, when Ku ~ Kd, Labyrinth domains, spin spiral state, or magnetic textures have been observed in the thin film.

The thesis works are summarized into five sections depending upon the strength of PMA by varying the thickness of FM. We have observed the bubble domain with PMA for low thickness FM and studied the DW dynamics whereas skyrmions have been identified when thickness increased near SRT in both Pt/CoFeB and Pt/Co thin film. For Pt/CoFeB thin film, an unusual behaviour in domain wall motion has been observed near the depinning field which is known as 'excess velocity'. The enhanced velocity has been modelled to a modified creep law by explaining the physical significance of a material-dependent parameter p. Using the boundary limit of p, the pinning parameters of the sample have also been predicted. Further, we have

studied the DW dynamics in Pt/Co/Re thin films. After insertion of a Re layer, the DW motion as well as interfacial Dzyaloshinskii-Moriya interactions (iDMI) constant enhances in the thin films. Hence, additive iDMI can be achieved using Pt and Re as heavy metals (HM) across a ferromagnet (FM). The chiral damping has been observed in the DW dynamics and it may depend on the strength of the out-of-plane bias field. With increasing the Co thickness near SRT, we have observed the low remanence slanted hysteresis loop which indicates the presence of chiral structure in Pt/Co/Ta and Pt/Co/Re samples. Further, by performing the topological Hall effect (THE) experiments, we have confirmed the existence of skyrmion in the sample. The Mumax micromagnetic simulations have been performed to verify the experimental results. As CoFeB is a low damping and low pinning material, we have also stabilized the skyrmion at room temperature and low magnetic field in Pt/CoFeB/MgO thin films. We have shown that our samples contain very low pinning energy which is confirmed via current induced motion of skyrmion. We able to drive the skyrmion using a low threshold current density of 0.8×10^{11} A/m^2 which is lower than the ones reported in the literature. It is observed that due to the presence of low dipolar energy the thermal stability of skyrmion is reduced and it is perturbed during magnetic force microscopy (MFM) scan even after using low moment tip. To solve the problem, we have prepared a thin film with $[Pt/Co/Ru]_7$ repetitive layers and observed a low remanence slanted out-of-plane hysteresis loop. MFM scan shows a worm to thread-like domain transformation by increasing magnetic field. Micromagnetic simulations confirm that the presence of low iDMI energy generates such achiral DWs and by enhancing the iDMI value further skyrmions can be stabilized in this system.

List of Figures

2.1: A schematic of the sputtering deposition technique in a vacuum chamber. The violet colour solid cone represents the plasma. Different atoms, involved in the process, are shown in different colour. Different components of a sputter deposition chamber are shown.

2.2: (a) Multi deposition chamber manufactured by MANTIS present in our lab at NISER. (b) Top view of the system. The numbers correspond to different deposition sources. 1-3 are the DC sputtering sources, 4 is the MAT60, 5-6 are the Rf sputtering sources, 7 is the e-beam evaporator, 8 is the NanoGen source and 9 is the thermal evaporator.

2.3: Schematic of the E-beam lithography (EBL) process.

2.4: (a) A schematic of the X-ray diffraction phenomenon. (b) The automated multipurpose X-ray diffractometer (SmartLab) is manufactured by Rigaku at NISER.

2.5: Schematic of X-ray reflection method in specular geometry and k_i, k_f and k_t are the wave vector of the incident, reflected and transmitted X-rays, respectively. (b) A typical XRR spectrum where the intensity of the reflected beam is plotted as a function of 2θ.

2.6: (a) A schematic representation of SQUID magnetometer. (b) The MPMS3 SQUID available in our lab at NISER.

2.7: (a) Illustration of magneto-optical interaction in longitudinal geometry. The magnetization (m) of the sample is parallel to the plane of incidence of polarised light. The electric field (E) of incident light combined with m of the sample generates the Lorentz motion (vLor) of the electrons. The Kerr amplitude (K) is obtained by projecting the vLor onto the plane perpendicular to the direction of propagation of the reflected light. (b) The relative configuration of the analyzer and polarizer are displayed with respect to the normally reflected amplitude (N) and Kerr amplitude (K). The picture is taken from ref. [116].

2.8: Schematic representation of different geometry of MOKE microesope.

2.9: (a) A conventional domain image formation method. In image plane two different colours represent the two opposite domain state. (b) Image of Kerr microscope set up available in our lab at NISER.

2.10: A schematic representation of DW velocity measurement protocol.

2.11: (a) and (b) Schematic of a tilted and tilt-corrected in-plane electromagnet, respectively. The tilt of the electromagnet is corrected via a rotating screw of the stage on which the magnet is placed.

2.12: (a) Schematic of symmetric DW propagation and corresponding DW velocity as a function of H_x for no iDMI case. (b) Schematic of asymmetric DW propagation and corresponding DW velocity as a function of H_x for sizeable iDMI case. Here, the velocity of left (v_L) and right (v_R) side DW shifted oppositely w.r.t $H_x = 0$.

2.13: (a) Illustration of basic principle of MFM. (b) Image of a magnetic hard drive bits measured via MFM. The dark and bright spot represents the repulsive and attractive force between stray fields of the magnetic tip and sample, respectively.

2.14: (a) Schematic representation of BLS measurement geometry. (b) Image of a typical BLS spectrum. The finite frequency shift between the S and AS lines indicates the presence of iDMI in a sample.

2.15: (a) and (b) Illustration of anti-stokes (AS) and stokes (S) process due to the inelastic scattering between photon and magnon, respectively. Magnon is created and annihilated in the stokes and anti-stokes process, respectively.

2.16: (a) Image of PPMS available at NISER. (b) and (c) Longitudinal and transverse transport measurements geometry. Four probe connections are utilized in longitudinal measurements, while five probe connections are used in transverse measurements.

3.1: Hysteresis loops measured along the out-of-plane direction of the sample using (a) p-MOKE microscope and (b) SQUID magnetometer.

3.2: (a) Subtracted domain image (by subtracting a nucleated image from a propagated image). The close red loops represent the nucleated and propagated domains. (b) Domain wall velocity (v) vs. field ($\mu_0 H$), and **(c)** $ln\ v$ vs $(\mu_0 H)^{-1/4}$ plot. To fit the measured data (using Eqs. 6 and 3), $\mu_0 H_d$ = 19 mT has been considered.

3.3: Three different field-dependent velocity regions are separated by the dotted vertical lines. The green dotted line and red line show the usual creep and modified creep law, respectively. The velocity prefactor is the same for all regions for the usual creep law but it varies for the modified creep law as shown in the figure [61].

3.4: (a)-(f) $ln\ v$ vs $(\mu_0 H)^{-1/4}$ plot considering $\mu_0 H_d$ between 16 to 25 mT. The red lines are the fit of the data using the modified creep law.

3.5: (a) BLS spectra of the sample at k_{sw}= 16.7 μm^{-1} and H_x= 420 mT, (b) plot of frequency difference (Δf) vs spin wave vector (k_{sw}).

4.1: (a) hysteresis loops of S1-S5 measured via polar MOKE microscopy, (b-d) K_{eff}, H_S, and M_S are obtained from hysteresis loops measured by SQUID magnetometer.

4.2: (a) DW velocity (v) vs. field ($\mu_0 H_z$) and (b) $ln\ v$ vs. $(\mu_0 H_z)^{-\frac{1}{4}}$ plots for S1-S5. The black dotted line is used in figure (a) to visualise the enhancement in v.

4.3: v_L and v_R as a function of H_x for S1 at (a) H_z=-9.75 mT and (b) H_z=-17.16 mT; for S2 at (c) H_z=-8.19 mT and (d) H_z=-13.65 mT.

4.4: v_L and v_R as a function of H_x for sample S3 at (a) H_z=-5.46 mT, (b) H_z= -7.02 mT and (c) H_z=-8.58 mT (c); for sample S4 at (d) H_z=-4.68 mT, (e) H_z =-5.85 mT and (f) H_z =-7.02 mT; for S5 at (g) H_z=-4.68 mT, (h) H_z=-5.85 mT and (i) H_z=-7.02 mT.

4.5: D_{eff} as a function of t_{Re}.

4.6: Subtracted domains of S1 at H_z=-9.3 mT (a), -14 mT (b), and -19 mT (c); for S3 at H_z=-4.6 mT (d), -5.1 mT (e) and -7.0 (f); for S5 at H_z=-4.6 mT (g), -5.1 mT (h) and -6.7 (i). Here, H_x = +100mT was fixed and the red arrow indicates the direction of H_x.

5.1: (a) Schematic of the sample structures. (b) Polar MOKE hysteresis loops of the samples S1-S3.

5.2: (a) Magnetization as a function of field for S1, S2 and S3 measured in out-of-plane mode. The out-of-plane and in-plane hysteresis loops of S1, S2 and S3 are shown in (b), (c) and (d), respectively.

5.3: (a-d) Field-dependent MFM images exhibiting the process of skyrmion formation. The isolated skyrmions are observed at $H_z \geq 12$ mT.

5.4: (a) and (b) MFM images of S2 and S3 at demagnetized states, respectively.

5.5: (a), (c) and (e) AHE+THE and AHE contribution in ρ_{xy} as a function of field for S1, S2 and S3, respectively. (b), (d) and (f) plots of ρ_{THE} vs field for S1, S2 and S3, respectively. The black arrow sign represents the field sweep direction.

5.6: (a) and (e) simulated (cyan colour) and MOKE (violet colour) hysteresis loops of S1 and S2, respectively. (b-d) and (f-h) reveals the field-induced simulated domain images for S1 and S2, respectively.

5.7: (a) Plot of $\langle Q_{sk} \rangle \; vs \; \mu_0 H$ at a constant K_{eff}. (b) A phase plot of D vs K_{eff} which shows the single to double peak transition in $\langle Q_{sk} \rangle$ or ρ_{THE}. The red cross mark represents no skyrmion during the field sweep.

5.8: (a) A single peak in $\langle Q_{sk} \rangle$ for D= 2.0 mJ/m^2 and K_{eff} = 0.4 MJ/m^3. The blue arrows refer to the corresponding domain structures as shown in (b-g). The green arrow represents the field sweep direction.

5.9: (a) A double peak with opposite sign in $\langle Q_{sk} \rangle$ for D= 5.0 mJ/m^2 and K_{eff} = 0.4 MJ/m^3. The red arrows refer to the corresponding domain structures as shown in (b-g). The green arrow represents the field sweep direction.

6.1: (a) Schematic of sample structure. GIXRD measurements of the bare substrate and the samples S1 and S2 are shown in (b), (c) and (d), respectively. For proper comparison, the intensity axis scale is the same for all the plots.

6.2: EDX scan on sample S2 (t_{CoFeB}=1.6 nm) at three different areas.

6.3: (a) MOKE hysteresis loop for the sample with t_{CoFeB}= 1.1-1.7 nm in polar mode. (b) Hysteresis loops for the sample with t_{CoFeB}= 1.7 nm measured at room temperature longitudinal modes

6.4: (a) Measurements geometry of BLS technique. (b) BLS spectra of sample S2 measured at a constant applied field (μ_0H = 371 mT). (c) Plot of frequency difference (Δf) vs spin wave vector (k_{sw}).

6.5: (a) an AFM image of sample S1. (b) and (c) MFM images of sample S1 at demagnetized state and at an applied out-of-plane field of 1 mT, respectively. (d) MFM image of sample S2 at an applied field of 3 mT. The cyan circled area in (c) is a guide to the eye for the distorted shape of the skyrmion induced by tip perturbation (horizontal scanning).

6.6: MFM image of the CoFeB sample in the demagnetized state (zero field) using a 15 nm/20 nm (a-b) and a 5 nm/20 nm (same tip as in the manuscript) (c) CoCr/Cr bilayers tip. Images (a) and (b) show significant perturbation whereas image (c) shows the expected stripe phase. Note that the different scan directions (respectively x and y fast scan axis) between images (a) and (b) highlight the deformations due to the magnetic tips that show magnetic textures elongated along the slow scan axis. (d) Image obtained with a 3 mT applied field of the skyrmion state, using the 5 nm/20 nm (c) CoCr/Cr bilayers

tip. This image shows that in the skyrmion phase, perturbation cannot be avoided. A thinner magnetic coating prevents a good signal being obtained from the samples. The phase scale for all three images is the same (300 mDeg). The image scales are identical, with a scale bar shown in (d).

6.7: (a) Schematic of the setup for current induced motion experiment with the AFM image of three 1 μm wide nanotracks (blue) with Ti/Au contacts (light brown) microfabricated on sample S1 (t_{CoFeB}: 1.5 nm). (b) Circuit diagram of the sample considering capacitive short through the substrate. (c) Shape of the voltage pulse measured on the 50 Ω load of an oscilloscope and (d) processed current pulse flowing through the nanotracks, for a 20 ns long 2 V pulse (note that due to the impedance mismatch at the sample, 25% of the pulse is reflected before the sample and does not participate to the pulse).

6.8: (a) and (b) show the position (by coloured circles) and displacement (by coloured lines) of the skyrmions before and after application of one current pulse. The white dashed lines indicate the boundary of a single nanotrack in the MFM image. Above these images, the arrows indicate the current *J*, velocity *v*, and applied field *H*. (d) shows the average skyrmion velocity vs current density plot. Blue lines + points are the measured average velocity. The standard deviation is shown by the green error bar.

7.1: (a) Schematic of sample structure. (b) Polar-MOKE hysteresis loop of the sample.

7.2: (a)-(h) Field evolution of the domain structure. A worm-like phase (a) changes to a thread-like domain at a higher field (g-h).

7.3: Total Hall resistivity (a) and magnetization (b) as a function of field. (c) Plot of different components of Hall resistivity *vs* field. The flat blue line indicates the no signature of THE. The black arrow sign represents the field sweep direction.

7.4: Sample stack (a) experimentally prepared, and (b) considered in the simulation. Here, t_m is the thickness (0.95 nm) of the single FM layer, whereas tr is the thickness of one repetition of the Pt (1.0nm)/Co (0.95nm)/Ru (1.4 nm) layer. This t_r is considered as the thickness of the effective FM layer (t_m') in the simulation.

7.5: Red-coloured (dotted) hysteresis loops are p-MOKE hysteresis loops. The green-colored loops are simulated hysteresis loops for D= 0.5 mJ/m^2 (a), 1.0 mJ/m^2 (b), 1.5 mJ/m^2 (c).

7.6: (a)-(f) reveals the field-induced simulated domain images. Worm–thread–achiral bubble domain transformation is observed as a function of field.

7.7: (a)-(f) reveals the field-induced simulated domain images. Worm phase–thread phase–chiral textures (mixed phase skyrmion) transformation is observed as a function of the field.

List of Tables

List of Abbreviations

ACW	Anti-clockwise
AFM	Atomic force microscopy
AHE	Anomalous Hall effect
AS	Anti-stokes
BLS	Brillouin Light Scattering
CA	cubic anisotropy
CVD	Chemical vapor deposition
CCD	Charge-coupled device
CW	Clockwise
DC	Direct current
D-E	Damon-Eshbach
DW	Domain wall
DMI	Dzyaloshinskii-Moriya interaction
EA	Easy axis
EBL	Electron beam lithography
EDX	Energy Dispersive x-ray
FD	Finite-difference
FM	Ferromagnet
FP	Fabry-Perot
GIXRD	Grazing incidence x-ray diffraction
HA	Hard axis
HDD	Hard disk drive
HM	Heavy metal
IPA	Isopropanol
iDMI	Interfacial Dzyaloshinskii-Moriya interaction
LCD	Liquid crystal display
LED	Light-emitting diode
LL	Landau – Liftshitz
LLG	Landau-Liftshitz-Gilbert
LCP	Left circularly polarized

MA	Magnetic anisotropy
MFM	Magnetic force microscopy
MCE	Magnetocrystalline anisotropy energy
MCA	Magnetocrystalline anisotropy
MOKE	Magneto-optic Kerr effect
MIBK	Methyl isobutyl ketone
1D	One-dimensional
OHE	Ordinary Hall effect
PBC	Periodic boundary conditions
PMA	Perpendicular magnetic anisotropy
PMMA	Polymethyl methacrylate
PVD	Physical vapor deposition
PPMS	Physical properties measurement system
QCM	Quartz crystal microbalance
RAMAC	Random-access method of accounting and control
RCP	Right circularly polarized
RE	Rare earth
Rf	Radio frequency
RK	Runge-Kutta
RT	Room temperature
RPM	Rotations per minute
S	Stokes
SHE	Spin Hall effect
SO	Spin-orbit
SOC	Spin-orbit coupling
SOT	Spin-orbit torque
SP-STM	Spin-polarized scanning tunneling microscopy
STT	Spin-transfer-torque
SRT	Spin-reorientation transition
SQUID	Superconducting quantum interference device
THE	Topological Hall effect

TMs	Transition metals
TMP	Turbo molecular pump
2D	Two-dimensional
UA	Uniaxial anisotropy
XRD	X-ray diffractometer
XRR	X-ray reflectivity

Chapter 1

Introduction:

Recording information has been a very common passion of human beings since thousands of years. In ancient times, people used to write or store very useful information using pictographic writing [1]. With increasing the demands of human beings many advancements in storage have been made in previous years. In the Modern Era, magnetic materials brought a revaluation in storage technology. The revaluation started in 1956 when IBM commercially introduced the first random-access method of accounting and control (RAMAC) magnetic hard drive (HDD). The HDD employed magnetic paints, deposited by spin coating, to make in-plane magnetized disk media. The areal density (bits/in^2) of the HDD was 2 kbits/in^2. The areal density decides the storage capacity of a HDD. Further, the areal density of a HDD has been increased by using an in-plane granular magnetic material and a maximum areal density of ~100 Gbits/in^2 has been achieved by reducing the size of the grains [2,3]. Now, the magnetization of each grains switches from one stable state to another after overcoming an energy barrier ΔE (= $K_u V$) for writing an information, where the K_u, V is the uniaxial anisotropy, and volume of the grains, respectively. The stability of the recorded information is governed by ΔE. If the ΔE is not sufficiently high enough, the magnetization of the grains may reverse to opposite state due to thermal energy ($k_B T$). Such a phenomenon where the magnetization of a magnetic particle gets reversed due to the thermal energy and without applying any field is known as superparamagnetism [4]. The typical switching time (τ) in this case can be estimated via an Arrhenius law, $\tau = \tau_0 e^{\frac{\Delta E}{k_B T}}$, where τ_0, k_B, and T is a characteristic attempt time, Boltzmann

constant and temperature, respectively. Now the stored information should be stable for a specific time-period which is known as 'retention time ($t_{\text{retention}}$).' For a HDD, the data retention time is around 10 years. Therefore, the energy barrier must comply with, $\Delta E > k_B T \, log\left(\frac{t_{retention}}{\tau_0}\right)$. So, to achieve stability in the storage information, the stability factor (Δ) (ratio of magnetic anisotropy energy and thermal energy) should be greater than 60 i.e. $\Delta = \frac{\Delta E}{k_B T} = \frac{K_u V}{k_B T} > 60$ [3,5]. Thus, to achieve more areal density, the volume of the gains needs to be reduced. However, after a certain volume of grains in HDD, the thermal energy then excited the magnetization and reversed the saturation state. Also, in the inplane HDD with increasing the areal density, the distance between magnetic charges or poles decreases which enhances the demagnetizing field. Again, the bits lie laterally in the in-plane recording medium, it takes more space at least 3-5 times higher than vertical alignment. So, the research community has faced a lot of difficulty and limitations in enhancing areal density using in-plane HDD. The problem was solved by introducing perpendicular storage technology. In the case of a perpendicular medium, the demagnetizing field became significantly reduced and the uniaxial anisotropy is also higher than in-plane systems which gives better thermal stability. Thus, around 2005 first HDD using a perpendicular recording medium was commercially introduced. After this, the perpendicular magnetic system has brought great research interest to the spintronics community. As, the bits lie vertically in a perpendicular recording medium containing less space, further reducing the volume of grains the storage capacity is enhanced significantly. In today's HDD, the areal density is ~1.5 Tbits/in^2 which is roughly a billion times larger than the first HDD [3].

'Smaller, faster, and efficient' are three main aspects for the ever-increasing demand for storage technology. However, due to the superparamagnetic limit perpendicular recording medium also reached its saturation limit. Therefore, recently, it has been predicted that DW-based storage

technology can be used in next-generation memory devices. Using a nanowire of width, spacing, DW width, and domain length of 10 nm, an areal density of ~2.9 Tb/in^2 can be achieved which is approximately 2 times higher than recent HDD technology [5]. However, the stability of domains, DW pinning, and operational power consumption are the main challenges for DW-based memory devices. A small perturbation in terms of applied field or thermal energy may lead to DW motion in the storage device or collapse the domain which destroys the information. Also, inhomogeneity in the nanotracks or defects in a film may introduce DW pinning which reduces the DW speed. Thus, by introducing a uniform chirality in the DWs, stability can be increased. Recently, Parkin et al., have predicted the chiral DW-based racetrack memory 3.0 version [6].

Further, chiral structures like skyrmions have attracted great research interest to the spintronics community due to their unique topological property, high thermal stability, nanoscale size, and low driving critical current density than DW [7,8]. Also, it is less sensitive to the pinning of the system. Thus, it has been predicted that skyrmions are very promising candidates for enhancing the next-generation data storage density. Like DW, skyrmion racetrack memory is also successfully demonstrated [9]. Apart from the storage application, DWs and skyrmions have proven potential applications in logic devices, transistor-like devices, neuromorphic computing, etc. [10–15]. Thus, studying the DW and skyrmion dynamics in a perpendicular anisotropic system is essential for fundamental as well as practical application purposes.

The PMA systems are categorized mainly into three different types i.e. ferromagnetic multilayer, crystalline alloys, and amorphous rare earth transition metal alloys. For, the ferromagnetic multilayer, the PMA exists in a heavy metal (HM)/ferromagnet (FM) thin film system, where the FM thickness should be below than the spin reorientation transition (SRT). The interfacial hybridization between 5d and 3d orbital of HM and FM (i.e. Pt/Co, Pd/Co,

Au/Co, Ir/Fe, Pt/CoFeB, etc.), respectively, enhances the spin-orbit (SO) interaction in the FM and PMA arises in the multilayer stack [16–19]. For crystalline alloys, due to their tetragonal crystal structure ($L1_0$ ordering), a uniaxial anisotropy arises along the c-axis which gives rise to PMA in (001) oriented Heusler films [20]. In amorphous rare earth transition metal alloys, as a cause of perpendicular anisotropy, various mechanisms have been proposed i.e. presence of anisotropic chemical bonding between the 3d and 4f electrons of transition metal (TM) and rare earth (RE) materials, respectively; magnetostriction; structural effects; anisotropic pair correlations; etc. [21]. In this thesis work, we have considered the multilayer thin film having PMA (i.e. Pt/Co and Pt/CoFeB system).

For a thin film with high PMA strength, i.e. $K_u > K_d$, circular bubble domains have been observed, where K_u and K_d are the uniaxial anisotropy density and demagnetization energy density, respectively [22]. However, when $K_u \sim K_d$, labyrinthine domains, spin spiral state, or magnetic textures (like skyrmions) have been observed in the thin film [23,24]. Here, we have observed the bubble domain with PMA for low thickness FM, and skyrmions have been identified when thickness increased near SRT in both Pt/CoFeB and Pt/Co thin films. Further, we have studied the DW as well as skyrmion dynamics.

The first chapter of the thesis is the "introduction" where the basic ideas related to the thesis work have been explained. In chapter 2, all the experimental methods have been discussed which are used in the thesis work. In chapter 3, field-induced DW motion has been studied in the Pt/CoFeB/MgO thin film. An enhancement in DW motion has been observed near the depinning field. Further, the value of interfacial Dzyaloshinskii–Moriya interaction (iDMI) has been quantified in such asymmetric thin film. In chapter 4, we have determined the iDMI value by varying Re thickness (t_{Re}) in the Pt/Co/Re (t_{Re})/Ta thin films and studied the effect of iDMI on DW dynamics. In chapter 5, increasing the Co layer thickness near SRT, we found the

topological Hall effect which confirms the presence of chiral texture in Pt/Co/Ta and Pt/Co/Re samples. Further, via micromagnetic simulations, we have confirmed the existence of skyrmions in those samples. In chapter 6, skyrmions at room temperature and low applied magnetic field have been stabilized in Pt/CoFeB/MgO samples. Further, the current-induced motion of skyrmions has been studied. We are able to drive the skyrmions via a lower critical current density through a nano-track. In chapter 7, we have observed a worm-to-thread-like domain transformation by increasing the magnetic field in $[Pt/Co/Ru]_7$ thin film. Micromagnetic simulations confirm that the presence of low iDMI energy generates such achiral DWs and by enhancing the iDMI value further skyrmions can be stabilized in this system. In Chapter 8, we present the conclusion of this thesis work and future prospects in this research topic.

1.1 Spin-orbit interaction:

Spin-orbit (SO) interaction is a coupling between the spin (**S**) and orbital angular momentum (**L**) of an atom. SO interaction plays a pivotal role in the spin relaxation, various interactions, and anisotropy of a magnetic system. The SO interaction is explained as follows. In reality, electrons are moving around the nucleus of an atom. However, from the electron frame of reference, it can be considered that the electron is fixed and the nucleus is moving around it in a relativistic approach (see figure 1.1). Therefore, the orbiting nucleus constitutes a current that produces a magnetic field at the center according to the Biot-Savart law which is written as:

$$\mathbf{B} = \frac{\boldsymbol{\varepsilon}\times\mathbf{v}}{c^2} \tag{1.1}$$

where $\boldsymbol{\varepsilon} = -\nabla V(r) = -\frac{\mathbf{r}}{r}\frac{dV(r)}{dr}$ is the electric field exerted on the electron due to the nucleus and V(r) is the corresponding potential. The magnetic field, **B**, interacts with the spin of the electron and the Hamiltonian can be written as [25].

$$H_{SO} = -\frac{1}{2}\mathbf{m}\cdot\mathbf{B} = \frac{e\hbar^2}{2m_e c^2 r}\frac{dV(r)}{dr}\mathbf{S}\cdot\mathbf{L} \tag{1.2}$$

where $\hbar\mathbf{L} = m_e\mathbf{r}\times\mathbf{v}$ and magnetic moment, $\mathbf{m} = \left(\frac{ge\hbar}{2m}\right)\mathbf{S}$. Now considering the Coulomb field for a hydrogen-like atom, $\frac{1}{r}\frac{dV(r)}{dr} = \frac{Ze}{4\pi\varepsilon_0 r^3}$ and $\langle r^{-3}\rangle = \frac{Z^3}{a_0^3 n^3 l\left(l+\frac{1}{2}\right)(l+1)}$, n and l are the principal and orbital quantum number of electrons. Therefore, the SO energy can be written as,

$$\langle H_{SO}\rangle = \frac{Z^4 e^2\hbar^2\langle\mathbf{S}\cdot\mathbf{L}\rangle}{4\pi\varepsilon_0 a_0^3 n^3 l\left(l+\frac{1}{2}\right)(l+1)}. \tag{1.3}$$

It should be noted that the SO energy is proportional to the Z^4. So, the heavy metal with a high atomic number (Z) shows high spin-orbit coupling (SOC). From equation 1.3 it is noticed that while **S** and **L** are parallel, the minimum energy state is favourable and energy maximizes when **S** is perpendicular to **L**. Therefore, if the direction of **L** lies along a specific crystallographic axis of a material, the energy will be the difference between the favoured and unfavoured orientations.

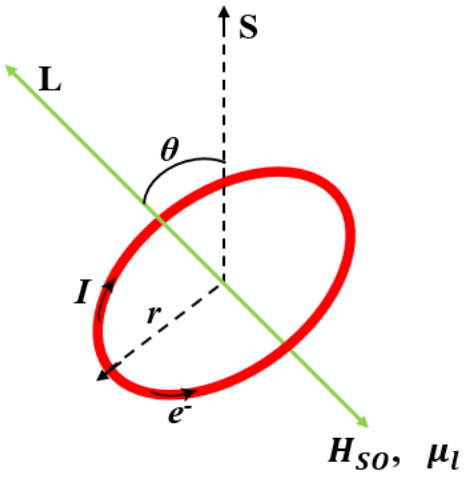

Figure 1.1: Schematic of spin-orbit interaction where the orbital angular momentum arises due to the current carrying loop.

1.2 Magnetic anisotropy:

Magnetic anisotropy (MA) is a directional-dependent magnetic property of a magnetic system. The Heisenberg exchange energy is isotropic in nature. Therefore, in the absence of any other energy the magnetization of a material would vanish at zero applied field. Also, the magnetic moment in a material cannot be rotated by applying any infinitesimal energy. Thus, some energy related to the anisotropy of the system defines the ferromagnetism of a system. Magnetic anisotropy decides the alignment of spontaneous magnetization in a ferromagnetic material. Thus, along a specific direction, it is easier to align all the moments of magnetic materials known as the 'Easy axis' (EA). Similarly, it is more difficult to magnetize the sample along another axis termed as the 'Hard axis' (HA). The MA energy is the difference between the EA and HA energies. Different types of magnetic anisotropy may present in a system which are discussed as follows:

1.2.1 Magneto crystalline anisotropy:

The most important contribution to the anisotropy of a system comes from magnetocrystalline anisotropy which arises due to the SO interaction of the electrons. The orbital of an electron is linked with the crystal structure of a material and prefers to align along a certain crystallographic axis. Along the particular direction, it is easier to magnetize the sample. The strength of magnetocrystalline anisotropy (MCE) energy is usually lower than the exchange energy. However, the direction of magnetization solely depends on anisotropy energy because exchange energy only tries to align the moments parallelly or anti-parallelly irrespective of its directions. The direction of magnetization $m = \boldsymbol{M}/|\mathbf{M}|$ can be defined by the direction cosine α_i as $m = (\alpha_1, \alpha_2, \alpha_i)$ and $\alpha_1 = \sin\theta\cos\phi$, $\alpha_2 = \sin\theta\sin\phi$, $\alpha_3 = \cos\theta$. Here, θ is the angle between the magnetization direction and z-axis and ϕ is the azimuthal angle. The direction cosines fulfill

the normalization condition as, $\alpha_1^2 + \alpha_2^2 + \alpha_3^2 = 1$. The MCA energy per unit volume can be written as [26],

$$E_{MCA} = E_0 + \sum_i b_i\alpha_i + \sum_{ij} b_{ij}\alpha_i\alpha_j + \sum_{ijk} b_{ijk}\alpha_i\alpha_j\alpha_k + \sum_{ijkl} b_{ijkl}\alpha_i\alpha_j\alpha_k\alpha_l + \Gamma(\alpha^5) \quad (1.4)$$

The higher order term, $\Gamma(\alpha^5)$, is very small so it can be neglected and b is the coefficient of anisotropy. The energies of opposite magnetized states are equal in amplitude i.e. $E(\alpha_i) = E(-\alpha_i)$. Hence, all the odd terms of the equation 1.4 cancel out and rewritten as,

$$E_{MCA} = E_0 + \sum_{ij} b_{ij}\alpha_i\alpha_j + \sum_{ijkl} b_{ijkl}\alpha_i\alpha_j\alpha_k\alpha_l \quad (1.5)$$

There are various types of MCA observed in a magnetic system such as uniaxial anisotropy, cubic anisotropy, hexagonal anisotropy, etc.

For uniaxial anisotropy (UA), the EA of a system aligns along one direction only over a 180° interval. As $E(\alpha_i) = E(-\alpha_i)$ all the cross terms $\alpha_i\,\alpha_j$ will cancel out each other i.e. $b_{ij}=0$ for $i \neq j$. If the EA of a system is considered along the z-axis, then the energy can be expressed as,

$$E_{UA} = E_a + b_{xx}{m_x}^2 + b_{yy}{m_y}^2 = E_a + b_{xx}\left({m_x}^2 + {m_y}^2\right), as\ b_{xx} = b_{yy}\ . \quad (1.6)$$

Thus, the uniaxial energy density can be written as $E_{UA} = b_{xx}\,sin^2\theta$, where b_{xx} is the uniaxial anisotropy constant.

For cubic anisotropy (CA), two EA axes exist which are mutually perpendicular to each other. In such cases, indices i = 1, 2, 3 are undistinguishable in systems with cubic symmetry, i.e. $b_{11} = b_{22} = b_{33}$. After simplifying the equation 1.5, the cubic anisotropy energy density can be represented as,

$$E_{CA} = K_0 + K_1(\alpha_1^2\alpha_2^2 + \alpha_1^2\alpha_3^2 + \alpha_2^2\alpha_3^2) + K_2\alpha_1^2\alpha_2^2\alpha_3^2 + \cdots\cdots \quad (1.7)$$

with the coefficients, K_i is the anisotropy constant and function of the b.

1.2.2 Shape anisotropy:

Shape anisotropy is another source of anisotropy in a system. For a spherical shape sample, the demagnetizing field is uniform in all directions. But for a non-spherical sample, one or more EA may present due to the shape of the sample. Since the demagnetization energy is lower along the long axis than the short axis, so, it is easier to magnetize a sample along the long axis. The reason behind this is that the induced poles are far apart from each other along the long axis. The poles at the surface of the samples generate a stray field outside the sample. Consequently, the existence of a stray field induces a demagnetization field inside the sample. Therefore, the energy of the sample associated with the stray field or demagnetization field can be written as [26],

$$E_{demag} = -\frac{1}{2}\int \mu_0 \boldsymbol{M}.\boldsymbol{H}_{demag}\, dV \tag{1.8}$$

where H_{demag} represents the demagnetizing field of the sample. For an ellipsoid, the demagnetizing field can be written as, $H_{demag}= N\ \boldsymbol{M}$ with N= demagnetizing factor. Now equation 1.8 is modified as [26],

$$E_{demag} = \frac{1}{2}\int \mu_0 \boldsymbol{M}.N\boldsymbol{M}dV = \frac{1}{2}V\mu_0 \boldsymbol{M}.N\boldsymbol{M} \tag{1.9}$$

where V is the total volume of the sample. If the semiaxes of the ellipsoid are considered as the axes of coordinated system then the N is a diagonal tensor with trace (N)=1. The tensor N represents as [26],

$$N = \begin{pmatrix} N_x & 0 & 0 \\ 0 & N_y & 0 \\ 0 & 0 & N_z \end{pmatrix}$$

Now the stray field energy is rewritten as [26],

$$E_{demag} = \frac{1}{2}V\mu_0\left(N_x m_x^2 + N_y m_y^2 + N_z m_z^2\right) \tag{1.10}$$

For an ellipsoid N_x=N_y along the equatorial axis and the equation 1.10 reduced to [26],

$$E_{demag} = \frac{1}{2}V\mu_0(N_x \sin^2\theta + N_z \cos^2\theta) = \frac{1}{2}V\mu_0(N_x - N_z)\sin^2\theta = KV\sin^2\theta \quad (1.11)$$

where $K = \frac{1}{2}\mu_0 M_S^2(N_x - N_z)$ defines the strength of the shape anisotropy of a system.

1.2.3 Surface anisotropy:

In the case of ferromagnetic thin film, the inversion symmetry is broken at the interface which leads to an interfacial or surface energy in the total effective anisotropy. The lower-order energy terms are permitted in such thin 2D films. Therefore, the effective anisotropy constant, K_{eff}, can be divided into two parts one describes the surface (K_s) and another volume (K_v) contribution [16,26]:

$$K_{eff} = K_v + \frac{2K_s}{t} \quad (1.12)$$

where t is the thickness of ferromagnetic (FM) film. The factor of two comes due to the two interfaces. The 2nd term of the equation 1.12 is inversely proportional to t. Thus, for low t only, it is important for a thin film. Equation 1.12 can be rewritten as,

$$K_{eff}t = K_v t + 2K_s \quad (1.13)$$

Now, plotting the $K_{eff}\,t$ as a function of t, one can estimate the K_v and K_s values. The slope and intercept of equation 1.13 give the K_v and K_s values, respectively. With increasing the t, K_s decreases while K_v increases. Therefore, for a particular thickness of FM i.e. $t = t_c$, K_{eff} becomes zero and the surface and volume contribution to anisotropy become equal. This critical thickness is called 'spin reorientation transition' (SRT) with $t_c = -\frac{2K_s}{K_v}$. For $t > t_c$, in-plane magnetization is present in a system. Whereas, for $t < t_c$, out-of-plane magnetization is favourable. So, volume anisotropy dominates in a thick film and prefers in-plane magnetization. In the contrary, surface anisotropy dominates in low thickness of film, and out-

of-plane or perpendicular magnetization stabilizes in a system. Figure 1.2 shows a typical example of such a plot for Co/Pd multilayers [16].

1.3 Magnetic interactions:

In magnetic materials, different kinds of magnetic interactions act between the magnetic moments (such as atomic or molecule spins). A combined effect of them decides the ground energy state of a system. The various types of interactions are discussed as follows:

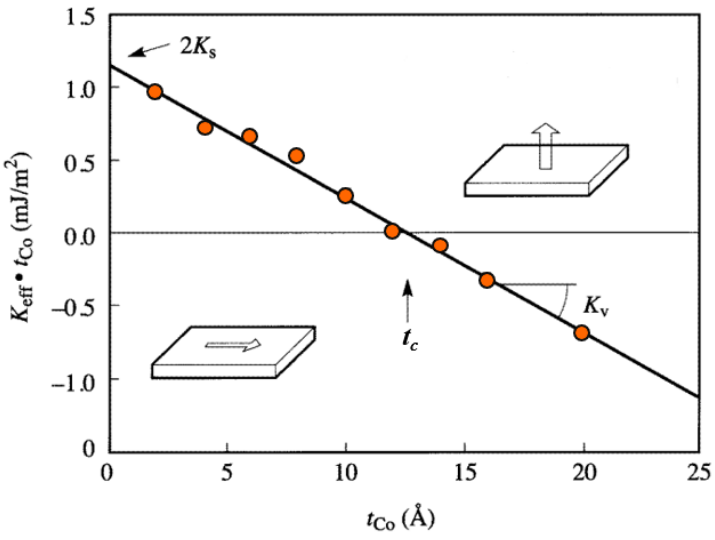

Figure 1.2: Effective anisotropy times thickness of Co layers versus individual Co layer thickness for a Co/Pd multilayer. This figure is taken from Ref. [27].

i. **Exchange interaction:** The exchange interactions act between two neighbouring spins of atoms. The exchange energy of a system can be written as [25],

$$E_{ex} = -\sum_{ij} J_{ij}\, \boldsymbol{S}_i \cdot \boldsymbol{S}_j \qquad (1.14)$$

where $\boldsymbol{S}_i$ and $\boldsymbol{S}_j$ are two neighbouring spins and J_{ij} is the exchange constant. This is a short-range and strongest interaction that always tries to keep the neighbouring spin co-linearly. For $J_{ij} > 0$, the neighbouring spins align parallelly which leads to

ferromagnetic ordering. For $J_{ij} < 0$, the neighbouring spins align anti-parallelly which leads to anti-ferromagnetic ordering.

ii. **Dipolar interaction:** If two magnetic dipoles μ_1 and μ_2 are separated by a distance r, the dipolar energy can be written as [25,28].

$$E_{dipolar} = \frac{\mu_0}{4\pi r^3}\left[\mu_1 \cdot \mu_2 - \frac{3}{r^2}(\mu_1 \cdot r)(\mu_2 \cdot r)\right] \quad (1.15)$$

This is a long-range interaction and depends upon the mutual alignment of the dipole moments.

iii. **RKKY interaction:** This is an indirect exchange interaction where the two metallic magnetic ions interact via a conduction electron [29–31]. It is called the RKKY interaction by taking the first letters of the surnames of its discoverers, i.e. Ruderman, Kittel, Kasuya, and Yosida. Here, the magnetic moment of a metallic ion generates spin-polarization in the conduction electrons, which subsequently coupled with the nearby magnetic ion at a distance of r. It is a long-range oscillatory interaction whose magnitude is determined by the distance r between the magnetic ions, as shown below,

$$J_{RKKY}(r) \propto \frac{cos(2k_F r)}{r^3} \quad (1.16)$$

where k_F is the radius of spherical Fermi surface.

iv. **Double exchange:** This interaction arises between the magnetic ions in different oxidation states through an itinerant "extra" electron. The electron can move back and forth between two species. During the movement, the electron always maintains the orientation of its spin. Thus, a strong spin polarization effect arises in double exchange which favours the ferromagnetic ordering [25]. This interaction is found in $La_{1-x}Sr_xMnO_3$, magnetite (Fe_3O_4), etc.

v. **Superexchange interaction:** This is an indirect exchange interaction. It occurs between two non-neighbouring magnetic ions mediated by an intermediated non-

magnetic ion. Thus, it is not a short-range exchange interaction and known as "superexchange" interaction [25,32]. This kind of interaction is mainly observed in ionic oxides or fluorides. For example, in MnO, two Mn^{2+} ions interact via an O^{2-} ion.

vi. **Dzyaloshinskii-Moriya interaction:** It is an anti-symmetric exchange interaction. This interaction presents in a system having a non-centrosymmetric crystal structure with large SOC atoms i.e. B20 types of materials. The Hamiltonian of the interaction can be written as [33,34],

$$H_{DMI} = -\sum_{ij} \boldsymbol{D}_{ij} \cdot (\boldsymbol{S}_i \times \boldsymbol{S}_j) \tag{1.17}$$

where $\boldsymbol{S}_i$ and $\boldsymbol{S}_j$ are two neighbouring spins and $\boldsymbol{D}_{ij}$ is the DMI constant. This interaction always tries to keep the neighbouring spins perpendicular to each other to achieve the lowest energy state. Recently, this interaction has been explored at the HM/FM interface, known as the interfacial Dzyaloshinskii-Moriya interaction (iDMI), as shown in figure 1.3 [35]. In the HM/FM case, the symmetry is broken at the interface and HM acts as a large spin-orbit coupling source.

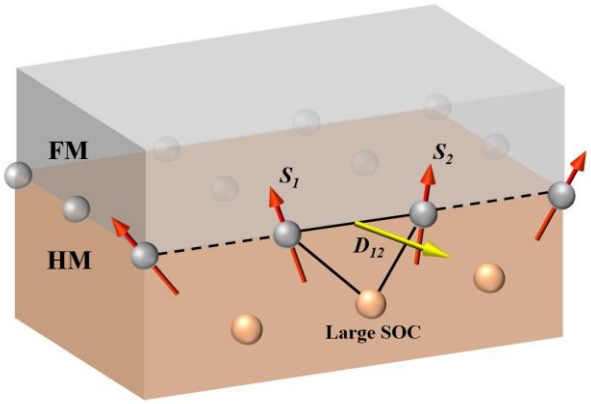

Figure 1.3: A schematic representation of interfacial Dzyaloshinskii-Moriya interaction (iDMI). The HM provides a large SOC in the interaction.

vii. **Zeeman interaction:** The Zeeman effect describes the splitting of atomic energy levels into two or more components in the presence of an intense magnetic field. An external magnetic field ($\boldsymbol{B}$) exerts a torque on a magnetic dipole ($\boldsymbol{\mu}$) and the corresponding energy associated with this interaction can be expressed as [25,28],

$$E_{zeeman} = -\boldsymbol{\mu} \cdot \boldsymbol{B} \tag{1.18}$$

The applied field always tries to align the moments along its direction to minimize the system energy.

The combined effect of all the above-mentioned energies decides the various magnetic properties i.e. magnetization reversal, domain structures, and size, magnetization dynamics, etc., in a magnetic system. Hence, the total energy of the system can be written as,

$$E_{total} = E_{ex} + E_{demag} + E_{ani} + E_{zeeman} + E_{DMI} \tag{1.19}$$

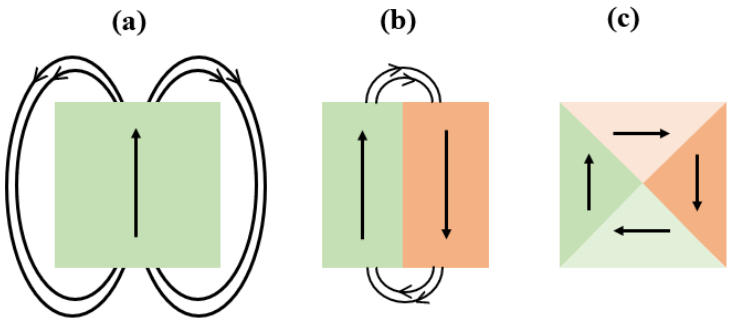

Figure 1.4: Flux closer property of magnetic domain to reduce the stray field energy. (a) single domain state (exhibiting the high stary field). (b) two domain states with reduced stray field energy by a factor of 2. (c) Flux closed domain with zero stray field.

1.4 Magnetic domains and domain walls:

A magnetic domain is a region in a magnetic material where all the moments align parallelly in the same direction which was first proposed by Pierre Weiss in 1907 [36]. A magnetic material contains several domains having randomly oriented magnetization to achieve the

lowest possible energy state. The neighbouring domains are separated by a region known as a domain wall (DW). In an ideal case, a system with finite exchange and anisotropy energies should exhibit a single domain state, in which all the moments are spontaneously magnetized parallel to the easy axis. Then free opposite poles are formed on the ends and induce a large stray field which increases the total energy of the system (see figure 1.4(a)). Now, if the system consists of two oppositely aligned domain states the energy can be reduced by a factor of 2 because the north and south poles come closer to one another leading to a decrease in the spatial extent of the stray field (see figure 1.4(b)). Therefore, by splitting the material into flux closer-type multi-domain states the magnetostatic energy again decreases significantly and the domain size also gets reduced (see figure 1.4(c)) [37]. However, the division cannot be continued indefinitely because of the DW formation energy which adds to the energy of the system. Hence an equilibrium domain state is achieved.

As DW separates two differently magnetized domains, the magnetization direction into the DW cannot change abruptly. Due to the exchange energy, the spins in DW rotate continuously at a small angle to maintain the energy minimization [28,38]. Hence, exchange energy always favours a wider DW structure. On the other hand, anisotropy always favours a thin DW structure as the magnetic moment prefers to align along EA minimizing the energy. Therefore, a competition between exchange and anisotropy energy decides the width of the domain wall. As the moments in the DW are neither aligned parallelly nor aligned along the EA, so it possesses some finite energy which is known as DW formation energy (σ_{DW}). Now considering the continuum model, the DW width and energy can be evaluated for a thick film and the exchange energy can be expressed as [28,39],

$$E_{ex} = -2A\,cos\left(\frac{d\varphi}{dx}\right) \tag{1.20}$$

where φ is the angle between two neighbouring spins, $A\left(=\frac{nJS^2}{a}\right)$ is the exchange constant with n = no. of atoms per unit cell and a = lattice parameter. Here, $\frac{d\varphi}{dx}$ defines the rate change of local magnetization w.r.t position inside the DW. Now, $cos\left(\frac{d\varphi}{dx}\right)$ can be expressed via a series expansion and the higher order term can be neglected (as φ is a small angle), then the equation 1.20 modified as [39],

$$E_{ex} = -2A + A\left(\frac{d\varphi}{dx}\right)^2 \tag{1.21}$$

The first term of R.H.S. is a constant and the second term is associate with exchange energy. Further, the anisotropy energy can be written in a generalized way, as:

$$E_K = g(\varphi) \tag{1.22}$$

Now, for a finite DW width, the torque arises from exchange and anisotropy energy balance each other such that the net resulting torque is zero at equilibrium. The torque arises due to the exchange energy,

$$L_{ex} = \frac{\partial E_{ex}}{\partial \varphi} = A\frac{\partial\left(\frac{d\varphi}{dx}\right)^2}{\partial \varphi} = 2A\frac{\partial \varphi}{\partial x}\frac{\partial^2 \varphi}{\partial x^2}\frac{\partial x}{\partial \varphi} = 2A\frac{d^2\varphi}{dx^2} \tag{1.23}$$

The torque arises due to the anisotropy energy [39],

$$L_K = \frac{\partial E_K}{\partial \varphi} = \frac{\partial g(\varphi)}{\partial \varphi} \tag{1.24}$$

At equilibrium condition, the resulting torque is zero, thus,

$$2A\frac{d^2\varphi}{dx^2} + \frac{\partial g(\varphi)}{\partial \varphi} = 0 \tag{1.25}$$

Now multiplying the equation 1.25 by $\frac{\partial \varphi}{\partial x}$ and integrating over *x,* the equation modified as

$$A\left(\frac{d\varphi}{dx}\right)^2 = g(\varphi) \tag{1.26}$$

Therefore, the DW formation energy can expressed as [39],

$$\sigma_{DW} = \sigma_{ex} + \sigma_K = \int_{-\infty}^{+\infty} \left[A \left(\frac{d\varphi}{dx} \right)^2 + g(\varphi) \right] dx \tag{1.27}$$

Using the value $A \left(\frac{d\varphi}{dx} \right)^2$ in the above equation, σ_{DW} is modified as,

$$\sigma_{DW} = \int_{-\infty}^{+\infty} 2g(\varphi)\, dx \tag{1.28}$$

Now, $g(\varphi) = K_U \sin^2 \varphi$ for uniaxial anisotropy, thus the σ_{DW} for a 180° DW can be defined as [39],

$$\sigma_{DW} = 2\sqrt{AK_U} \int_0^{\pi} sin\varphi \; d\varphi = 4\sqrt{AK_U} \tag{1.29}$$

Now the thickness of DW is defined considering the value of $\frac{d\varphi}{dx}$ obtained at the center of the DW. For uniaxial anisotropy, $\frac{d\varphi}{dx} = \sqrt{\frac{A}{K_U}}$ at the center of the DW. Thus, the DW thickness or width can be defined as [39],

$$\delta_{DW} = \pi \sqrt{\frac{A}{K_U}} \tag{1.30}$$

where A and K_U are the exchange and uniaxial anisotropy constants, respectively. There are two types of DW are observed in a magnetic material depending upon the rotation of magnetization inside the DW i.e., Neél wall and Bloch wall. For the Néel wall, the magnetization rotates in a plane perpendicular to the plane of the DW (see figure 1.5(a)) [40] whereas the magnetization rotates in a plane parallel to the plane of the DW for the Bloch wall (see figure 1.5(b)) [39].

Now for in-plane magnetized thin films, the Neél wall is energetically favourable than the Bloch wall because a Bloch wall creates the surface charge leading to a large magnetostatic energy related to the stray field in this case. In the contrary, for out-of-plane magnetized thin

film, the magnetic charge in the volume or DW plane is not accumulated by the Bloch wall, whereas it is accumulated by the Néel wall leading to a higher stary field. Therefore, the Bloch wall is energetically favourable for perpendicularly magnetized films. In this case, the domain

[40] [39]wall formation energy is expressed as, $\sigma_{BW} = 4\sqrt{AK_U}$. Now if a finite iDMI is present in a PMA system, the lowest energy domain wall configuration is determined by the competition between DMI, anisotropy and exchange energy. DMI induces a homochiral (right-handed chiral or left-handed chiral) Neél walls in a PMA film and the sign of iDMI vector defines the chirality of the DWs. In this scenario, the domain wall formation energy is modified as, $\sigma_{DW} = 4\sqrt{AK_U} \pm \pi D$, where D is the iDMI constant [40].

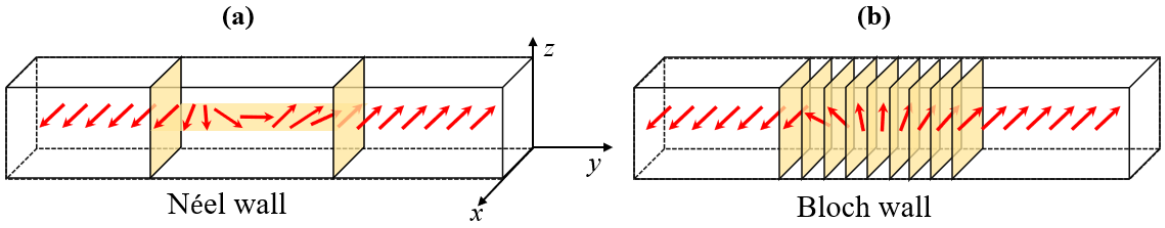

Figure 1.5: (a) and (b) A schematic of Néel and Bloch domain walls. The red arrows represent the magnetization directions.

1.5 Magnetization dynamics:

The time and space evaluation of magnetization under the application of an external field can be explained via the Landau-Lifshitz Gilbert (LLG) equation. Landau and Lifshitz first proposed this equation [37] and later Gilbert modified it [41]. Let's consider an electron is moving in a circular loop with radius r, then the magnetic moment of the electron can be written as, μ=iA. The associated angular momentum of the electron is, $L = m_e(\boldsymbol{v} \times \boldsymbol{r})$ while m_e = mass of electron. Thus, the moment can be modified as,

$$\mu = iA = -\frac{e}{t}A = -\frac{e\boldsymbol{v}}{2\pi r} \times \pi \boldsymbol{r}^2 = \frac{e\boldsymbol{v}\times\boldsymbol{r}}{2} = -\frac{e}{2m_e}\boldsymbol{L} = -\gamma \boldsymbol{L} \tag{1.31}$$

where $\gamma = \frac{e}{2m_e}$ is the gyromagnetic ratio. Differentiating equation 1.31, we can obtain,

$$-\frac{1}{\gamma}\frac{d\mu}{dt} = \frac{dL}{dt} = \tau \tag{1.32}$$

Here, τ is the torque applied to the magnetic moments. Under the application of a magnetic field the electron will experience a torque, $\tau = \boldsymbol{M} \times \boldsymbol{H}_{\text{eff}}$ and start presession around H_{eff} by forming a cone. Here, M is the total magnetic moment of a ferromagnet having N atomic spins and $M = N\mu$. The effective field ($\boldsymbol{H}_{\text{eff}}$) can be expressed as,

$\boldsymbol{H}_{\text{eff}} = \boldsymbol{H}_{\text{external}} + \boldsymbol{H}_{\text{exchnage}} + \boldsymbol{H}_{\text{anisotropy}} + \boldsymbol{H}_{demag}$.

The equation 1.32 can be modified as [37,41],

$$\frac{dM}{dt} = -\gamma\left(M \times H_{eff}\right) \tag{1.33}$$

The RHS of equation 1.33 is the damp-free precessional motion of magnetization around $\boldsymbol{H}_{\text{eff}}$. However, in a real system, the motion cannot be damped free and after a certain time, the magnetization aligns the applied field direction. Therefore, a damping term is introduced in equation 1.33, and Landau – Liftshitz (LL) modified the equation as:

$$\frac{dM}{dt} = -\gamma\left(M \times H_{eff}\right) - \frac{\lambda}{M_S^2}\left[M \times \left(M \times H_{eff}\right)\right] \tag{1.34}$$

here, λ and M_s represent a phenomenological LL damping term and saturation magnetization, respectively. The 2nd term of equation 1.34 defines the damping-like torque and acts towards the center of the precessional motion of magnetization. Later, Gilbert introduced a dimensionless damping parameter (α) and modified the equation as:

$$\frac{dM}{dt} = -\gamma\left(M \times H_{eff}\right) + \frac{\alpha}{M_S}\left(M \times \frac{dM}{dt}\right) \tag{1.35}$$

where $\alpha = \frac{\lambda}{\gamma M_S}$ is the damping constant. Equation 1.35 is known as the LLG equation. A schematic of the magnetization precession with all the torque is shown in figure 1.6. The LLG equation plays an important role in understanding the magnetization reversal and DW dynamics of a ferromagnetic system.

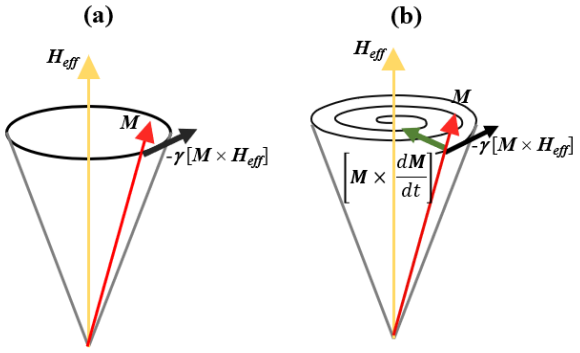

Figure 1.6: (a) and (b) Magnetization precession in the absence and presence of damping, respectively.

1.6 Domain wall (DW) dynamics:

DW in a magnetic thin film can be moved by applying a magnetic field [42–44], electric field [45], spin transfer torque (STT) [46,47], spin-orbit torque (SOT) [48], spin wave, etc. Among these, we have studied the magnetic field-induced DW motion in this thesis work.

1.6.1 Field-driven DW motions:

Initially, the DW motions are predicted in defect-free magnetic system by considering the 1D model. Walker first categorized the DW dynamics in two different regimes i.e., steady state, and precessional regime, as shown in figure 1.7 (a). In the steady state, the DW velocity linearly increases with the applied field. After a critical field, known as Walker field ($H_W = \frac{\alpha M_S}{2}$), the magnetization inside the DW starts to oscillate [49,50]. Thus, the DW velocity decreases and

enters to precessional regime. Further, increasing the field the DW velocity again starts increasing and reaches in the steady state regime.

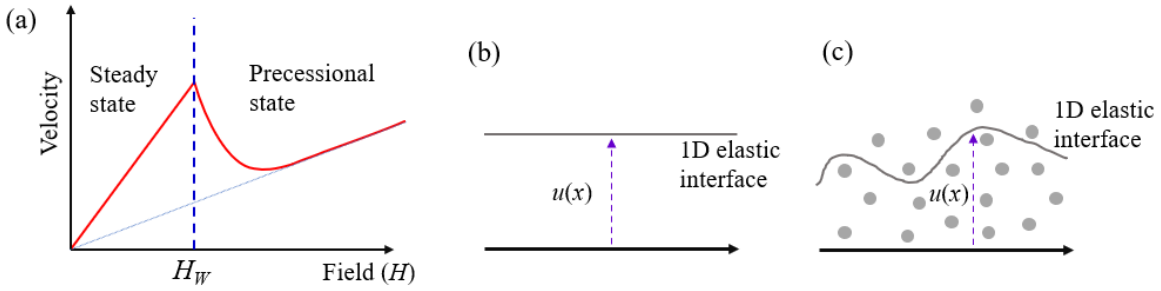

Figure 1.7: (a) DW velocity as a function of the field considering DW moving through a defect-free magnetic system. (b) An elastic DW surface moving without any defects or disorder. (c) DW surface experiences pinning due to defects or disorder during its motion.

In reality, a magnetic thin film cannot be defect-free and DW behaves differently in such a disordered medium. Therefore, DW is considered as a 1D interface in a 2D disordered medium as shown in figure 1.7 (b-c). In the absence of disorder, only elastic energy adds to the total energy of the system. As the DW deformations are associated with elastic energy, therefore DW surface remains flat (figure 1.7 (b)). However, disorder introduces extra pinning energy in the system thus in the presence of disorder the DW finds a configuration minimizing both elastic and pinning energy, as shown in figure 1.7 (c). Let's consider a DW in a disordered medium at a height $u(x)$. A rough interface can be characterized by studying fluctuations in the height $u(x)$ of the interface as a function of the length of the interface (see figure 1.7 (c)). Now the correlations between the DW heights at different positions (separated by a distance, L) along the wall length can be measured using the height correlation function, $u(x)$, as [51,52]:

$$C^2(L) = \langle [u(x) - u(x+L)]^2 \rangle \tag{1.36}$$

Now in the absence of a magnetic field at zero temperature, the equation 1.36 can be modelled in a scaling law considering a wandering exponent, ζ:

$$C^2(L) \propto \left(\frac{L}{L_C}\right)^{2\zeta} \tag{1.37}$$

here, ζ=2/3 and L_c is the Larkin length which defines the length over which deformations induced by the disorder are energetically favourable. The value of ζ depends on the random disorder force, interface, and dimensionality of the system [53,54] The elastic energy associated with a DW segment L can be defined as, $E_{elastic} \approx \varepsilon_{el}\frac{\xi}{L}$ and the corresponding pinning energy acting on the wall is $E_{pinning} \approx \varepsilon_{pin}\xi^{\frac{3}{2}}(n_i L)^{\frac{1}{2}}$, here ξ, n_i, ε_{el}, and ε_{pin} are the characteristic length over which the point defects act, defects density, elastic, and pinning constant, respectively. Therefore, the gain in pinning energy grows as $L^{1/2}$ and the cost in elastic energy reduces as $1/L$. Hence, above a critical length, L_c, the gain in pinning energy overcomes the elastic energy associated with a DW segment. Shorter than L_c, the elastic energy will dominate and DWs remain flat [55]. So, disorder in a system plays an important role in determining the DW dynamics. The disorder may arise due to the pinning sites coming from nanoscale defects, grain boundaries, interface roughness, variation in stress, etc. At T=0 K, due to the absence of thermal energy, the DWs are strongly pinned by the pinning potential of the system. With increasing the applied field, the DWs start moving beyond a critical field which is known as the depinning field (H_d), as shown in figure 1.8. However, for $T\neq0$ K, a combined effect of thermal and Zeeman energy controls the DW motion, and three different regimes (i.e., creep, depinning, and flow) are observed as a function of an externally applied field.

i. Creep regime: When $T\neq0$ K, the thermal energy helps in DW propagation at a low driving force. In this region, DW moves very slowly and increases exponentially with the applied field. Thus, the DW velocity can be represented by the Arrhenius law:

$$v \sim e^{-\frac{\Delta E}{k_B T}} \tag{1.38}$$

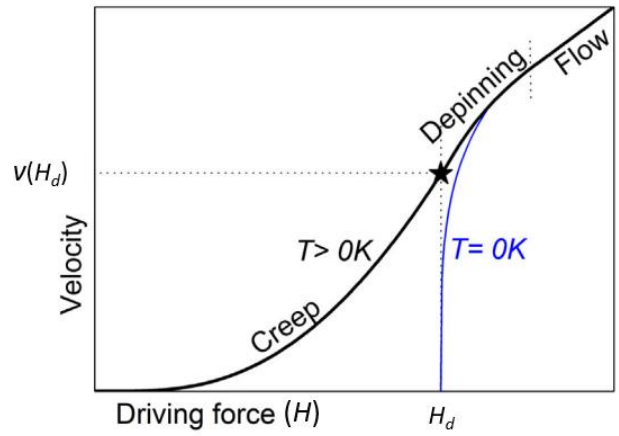

Figure 1.8: Motion of pinned elastic interfaces. The blue and black curve shows the DW motion at T= 0 K and T>0 K, respectively. The image is taken from Ref. [56].

here ΔE and $k_B T$ represent pinning potential and thermal activation energy, respectively. Now the phenomenological scaling theory [57,58] and functional renormalization group [59]define the $\Delta E \sim H^{-\mu}$ while a 1D interface moves through a 2D disorder medium, where μ is the creep exponent. Therefore, for small applied field $H < H_d$, the pinning potential is represented as

$$\Delta E\ (\mathrm{H} \to 0) = k_B T_d \left(\frac{H}{H_d}\right)^{-\mu} \tag{1.39}$$

If d is the dimensionality of the system, then $\mu = \frac{d-2+2\zeta}{2-\zeta}$. For DW, d =1 and ζ= 2/3, thus μ =1/4 is a universal creep exponent. T_d is the depinning temperature. For large field value, (near to H_d), equation 1.39 is not applicable and it needs modifications. In particular, when it becomes equal to H_d the pinning barrier should vanish. In that case [$0 < H \leq H_d(T)$] the pinning potential scales as [56],

$$\Delta E = k_B T_d \left[\left(\frac{H}{H_d}\right)^{-\mu} - 1\right] \tag{1.40}$$

Hence, the DW motion in the creep region is represented as [43,60],

$$v = v_0 e^{-\frac{T_d}{T}\left[\left(\frac{H}{H_d}\right)^{-\mu}-1\right]} \quad (1.41)$$

where $v_0 = v(H_d, T)$ is the velocity at H_d. It has been observed that the ratio $\Delta E/k_B T_d$ vs H/H_d (reduced field) follows a universal behaviour over the whole creep regime ($0 < H \leq H_d$) which is independent of materials and temperature [56]. The creep regime is observed for both the field and current-induced DW dynamics [61].

ii. Depinning regime: For $H > H_d$, with the help of thermal energy the DW motion gets free from the pinning sites of the sample. The DW velocity gets suddenly enhanced and the slope of the *v-H* curve gets changed. This region in DW dynamics is known as the depinning regime. At the depinning threshold i.e., at $H = H_d$, the DW velocity can be expressed by an asymptotic power law [43,62,63]:

$$v(H_d, T) = v_T \left(\frac{T}{T_d}\right)^{\psi} \quad (1.42)$$

However, above H_d [$H_d(T) < H < H_u(T)$], at $T << T_d$, the DW motion varies with the magnetic field and is written as:

$$v(H, T \ll T_d) = v_H \left(\frac{H-H_d}{H_d}\right)^{\beta} \quad (1.43)$$

Here v_T and v_H are depinning velocities. ψ (=0.15) and β (=0.25) are universal depinning and thermal exponents, respectively. H_u is the upper limit of the depinning regime. The Equations 1.42 and 1.43 can be combined using a generalized homogeneous function, as [63]:

$$y = g\left(\frac{x}{x_0}\right) \quad (1.44)$$

where the dimensionless variables, y and x, are represented as, $y=(v/v_T)(T/T_d)^{-\psi}$ and $x = [(H-H_d)/H_d]^{\beta}(T/T_d)^{-\psi}$ with $x_0 = v_T / v_H$. The function g is predicted to be universal within a given class of universality. For $x << x_0$, $g(x/x_0) \rightarrow 1$ corresponds to temperature-dependent depinning

velocity which is basically equation 1.42. For $x>>x_0$, $g(x/x_0)\rightarrow x/x_0$ corresponds to field-dependent DW velocity at zero temperature like equation 1.43. The parameters v_T, v_H, H_d, and T_d are nonuniversal and temperature-dependent. The values of v_T and v_H should be in the same order and $x_0 = 0.65 \pm 0.04$ is a universal constant [63].

iii. Flow regime: Now, further increasing the field, for $H>H_u$ the DW motion moves to the flow regime and is independent of temperature as well as pinning. Therefore, the DW dynamics in this region can be expressed as [42]:

$$v = mH \tag{1.45}$$

where m is the mobility of DW motion. Rather than disorder, dissipation also controls the DW motion flow regime. The dissipation is represented by the damping constant, α, which is related to the DW mobility, m. Due to a change in the internal dynamics of the wall, two different mobilities can be observed in the DW motion in the flow region. Below a critical field known as the Walker field, H_W, m can be expressed as $m = \gamma\Delta/\alpha$. This is called steady state region as discussed earlier. Sufficiently above H_W, the magnetization within the DW starts precession and enters the 2nd steady state region known as the precessional flow regime. In this region, the DW mobility is lower than the previous case and can be expressed as $m = \gamma\Delta/(\alpha + \alpha^{-1})$. Therefore, the complete flow region consists of two different linear flow regions connected by a non-linear intermediate region. The DW mobility m is completely material dependent, thus, the v follows a non-universal class.

To summarize the above discussion, DW motion follows a universal function in creep and depinning transition regimes below the universality limit $(H\leq H_u)$. Now, for $H>H_u$ the DW motion enters to flow regime, depends on materials, and follows a non-universal class [43].

1.6.2 DW motion in the presence of both in-plane and out-of-plane fields:

As discussed earlier, an asymmetric thin film structure of HM/FM/oxide (metal) can originate iDMI at the HM/FM interface. DMI energy combined with anisotropy, exchange, and demagnetization energies determine magnetization configuration in a system. In a magnetic system, two neighbouring DWs may have the same or different chirality as shown in figure 1.9 (a). However, iDMI induces a fixed chirality in the DWs of a magnetic system [64,65]. If a PMA system possesses sufficient iDMI, then the NW can be observed instead of the BW. In the case of chiral NW, the core magnetizations of two adjacent DWs align oppositely. Therefore, the iDMI field comes from DMI interaction which acts on the DWs oppositely in the in-plane direction. So, in a PMA thin film having a bubble domain, the iDMI field maintains the rotational symmetry with respect to the axis parallel to the out-of-plane magnetic field. Therefore, an isotropic domain expansion is observed in the absence of an in-plane field (see figure 1.9 (b)). However, under the application of an in-plane bias field, the rotational symmetry is broken and the domain expands anisotropically, as shown in figure 1.9 (c). Depending upon the direction of the applied field and DMI field, the left and right side DW will experience different forces as shown in figure 1.9 (c) which causes the anisotropic expansion. First, Je et al. have proposed this method to quantify the iDMI considering the DW dynamics limited only to the creep regime. In this context, a modified creep theory has been proposed incorporating the in-plane field (H_x) dependency into the energy barrier scaling parameter. The modified creep law can be expressed as [66,67]:

$$v_{DW}(H_x) = v_0 e^{-\zeta H_Z^{-\mu}} \tag{1.46}$$

where μ=1/4 and $\zeta = \zeta_0 \left(\frac{\sigma(H_x)}{\sigma_0}\right)^{-1/4} = \frac{T_d}{T} H_d^{1/4} \left(\frac{\sigma(H_x)}{\sigma_0}\right)^{-1/4}$. ζ_0 depends on the pinning potential of the sample in the absence of H_x. The H_x dependent energy, $\sigma(H_x)$ can be written as:

$$\sigma(H_x)|_{B-N} = \sigma_0 - \frac{\delta(\pi\mu_0 M_S)^2}{8K_D}(H_x + H_D)^2 \text{ for } |H_x + H_D| < \frac{4K_D}{\pi\mu_0 M_S}$$

$$\sigma(H_x)|_N = \sigma_0 + 2K_D\delta - \pi\delta\mu_0 M_S|H_x + H_D|, \text{otherwise} \quad (1.47)$$

where $\sigma_0 = 2\pi\sqrt{Ak_{eff}}$ is the Bloch wall energy, $\delta = \sqrt{A/k_{eff}}$ is the DW width and $K_D = t\ ln(2)\frac{\mu_0 M_S^2}{2\pi\delta}$ is the DW anisotropy energy density.

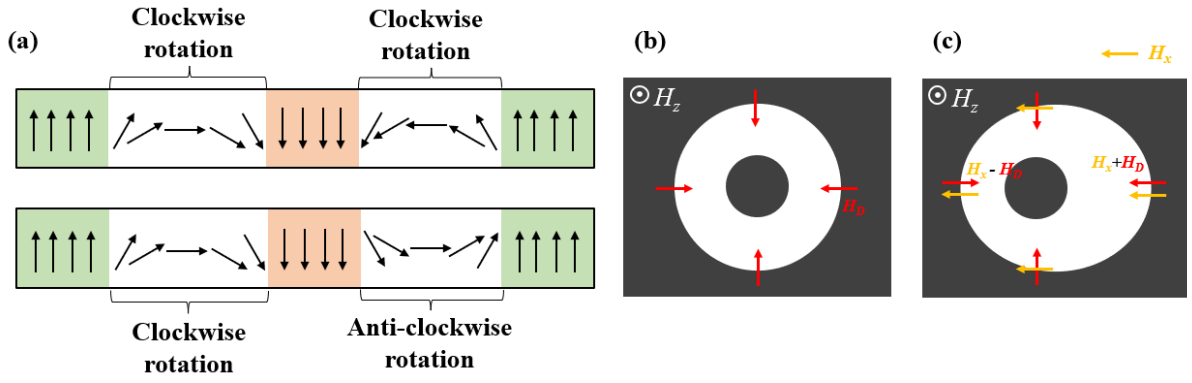

Figure 1.9: (a) Different chirality in DWs. A fixed chirality appears due to iDMI. (b) symmetric expansion of DWs in the absence of an in-plane field (H_x). (c) Applied in-plane field breaks the rotational symmetry of the DMI field (H_D) which leads to asymmetric expansion of DWs. The red and yellow arrows indicate the direction of H_D and H_x, respectively.

1.7 Skyrmions:

Skyrmion was first introduced in Nuclear physics by Tony Skyme in 1961 to describe a topological soliton of the pion field as a model of the nucleon [68]. Later, Bogdanov et al., predicted that the skyrmions may be observed in ferromagnetic materials [69,70]. In 2009, first

skyrmions were investigated experimentally in MnSi bulk materials (B20 type) via neutron scattering [71]. Further, due to practical application purposes, it has been stabilized in a multilayer thin film having perpendicular anisotropy [7,72–75]. Magnetic skyrmions are two-dimensional, topologically protected, localized, swirling spin textures with a core magnetization pointing in a direction opposite to its surrounding.

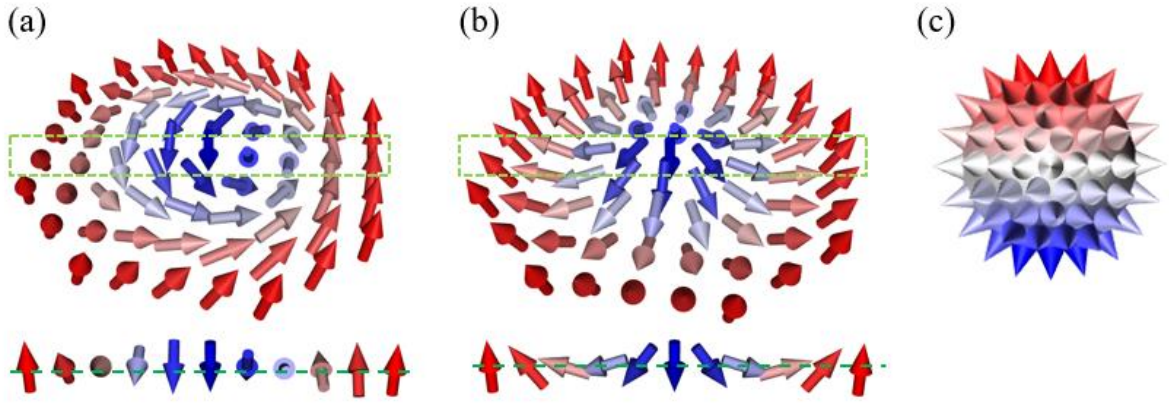

Figure 1.10: Schematic of Bloch (a) and Néel skyrmions (b). The cross-sectional views of the skyrmions are shown along the green dotted square loops. (c) Mapping of a skyrmion on a unit sphere. The skyrmion images are generated using Spirit [76].

1.7.1 Bloch and Néel skyrmions:

DM interaction plays a very important role in stabilizing a skyrmion. Depending upon the nature of DM interaction, there are two types of skyrmions have been observed in a magnetic system i.e., Bloch and Néel skyrmions. For non-centrosymmetric bulk material, bulk DMI stabilizes the Bloch skyrmions (shown in figure 1.10(a)). Whereas, interfacial iDMI, originating from HM/FM interface, stabilizes the Neel skyrmion in a thin film system (shown in figure 1.10(b)). It is found that the reversal of spin profile will be helicoidal in Bloch skyrmions (like for Bloch domain wall, figure 1.5(b)) and cycloidal in Néel skyrmions (like for

Néel domain wall, figure 1.5(a)). Via stereographic projection both the skyrmions can be mapped on a sphere (figure 1.10(c)) and exhibit the exact same topological properties.

1.7.2 Topological properties of skyrmion:

Skyrmions exhibit unique, non-trivial, topological properties due to which many interesting features appear. Topology is a mathematical concept where the property will be invariant under a continuous deformation. It is possible to understand topology by looking at the windings in the solution space of the field. Therefore, the magnetization of texture can be modeled by a space-varying function **m**(x,y) in an infinite plane, which defines the normalized magnetization direction locally. The topological number (Q_{sk}) (or winding number or skyrmion number) of a texture can be obtained by integrating **m**(x,y) over the space which is basically a measure of the local winding of **m**, as [7,77,78]:

$$Q_{sk} = \frac{1}{4\pi} \iint \mathbf{m} \cdot \left(\frac{\partial \mathbf{m}}{\partial x} \times \frac{\partial \mathbf{m}}{\partial y} \right) dxdy \tag{1.48}$$

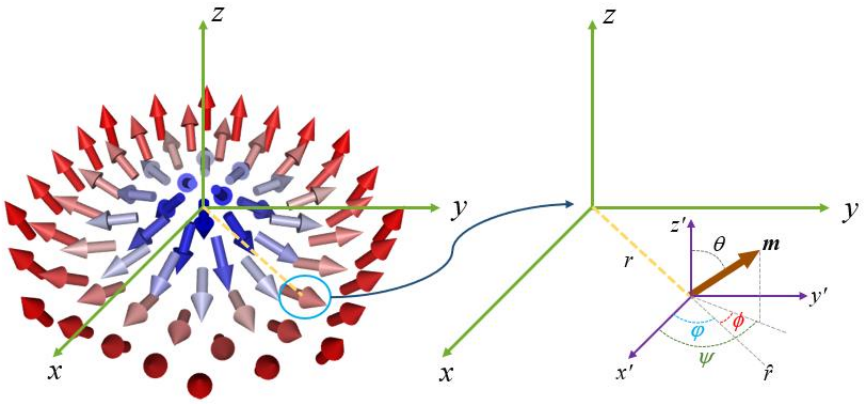

Figure 1.11: Representation of the polar coordinate systems which is used to describe skyrmions.

Now the position of individual **m**(x,y) can be expressed in polar coordinate (r, φ) as texture is 2D here. The value of individual **m** is defined in the unit sphere with spherical coordinates (θ,

ψ), as $\hat{m} = sin\,\theta\, cos\,\psi\,\hat{x} + sin\,\theta\, sin\,\psi\,\hat{y} + cos\,\theta\,\hat{z}$. The coordinate system is shown in figure 1.11. For simplicity ψ is constant w.r.t *r* and the equation 1.48 rewritten as [77,79,80],

$$Q_{sk} = \frac{1}{4\pi}\int_{r=0}^{\infty}\int_{\varphi=0}^{2\pi}\frac{d\theta}{dr}sin\,\theta\,\frac{d\psi}{d\varphi} = \frac{1}{4\pi}[-cos\,\theta(r)]_{r=0}^{r=\infty}[\psi(\varphi)]_{\varphi=0}^{\varphi=2\pi} = P.V \tag{1.49}$$

Here *P* and *V* are the core polarity and vorticity of skyrmion, respectively. They are expressed as [77,79,80],

$$P = \frac{[-cos\,\theta(r)]_{r=0}^{r=\infty}}{2} = \frac{[m_z(0)-m_z(\infty)]}{2} \tag{1.50}$$

$$V = \frac{[\psi(\varphi)]_{\varphi=0}^{\varphi=2\pi}}{2\pi} \tag{1.51}$$

Thus, the topological number is a product of *P* and *V*. From the cylindrical symmetry, one can write $\psi = V\varphi + \phi$, where ϕ is the tilt angle of magnetization w.r.t the radial axis or helicity of skyrmion. Now, for skyrmion, *V*=1 and in the contrary *V*= -1 for anti-skyrmion. The spin configuration of skyrmions can be wrapped over a unit sphere, thus the Q_{sk}=±1 and *V*=1 distinguish it from any other spin textures like anti-skyrmion, skyrmioniums, etc. In other way, Q_{sk} is quantized for skyrmions and defines a particular homotopy class. A magnetic texture can be converted into other topological objects if only they belong to the same homotopy class. The transformation is absolutely forbidden among the different types of homotopy classes. For example, a skyrmion with Q_{sk}=±1 cannot be continuously transformed into a uniformly magnetized state with Q_{sk}= 0. Thus, skyrmion is topologically protected.

Now depending upon the *P* and ϕ, various types of skyrmions with different chirality can be obtained. Various types of skyrmions are shown in the figure 1.12. For ϕ = 0 or π, the magnetization rotates in a cycloidal nature along the radial axis which defines the Néel skyrmions (see figure 1.12 (a), (c), (e), and (g)). Similarly, ϕ = π/2 or 3π/2 prefers the helicoidal arrangements and corresponds to Bloch skyrmions (see figure 1.12 (b), (d), (f), and (h)). For

Néel skyrmion, if $P.\cos(\phi)>0$ the chirality should be clock-wise (CW) and $P.\cos(\phi)<0$ for the counterclockwise (CCW). For Bloch skyrmion, if $P.\sin(\phi)>0$ the chirality is CW, and $P\cos(\phi)<0$ for CCW. The chirality is also selected by the sign of the DM interaction. D>0 and D<0 prefers CW and CCW chirality, respectively.

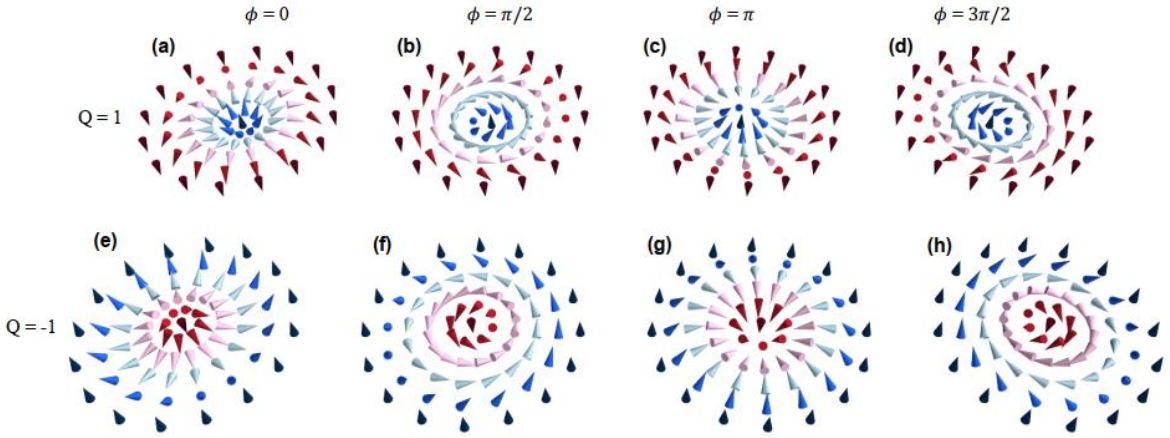

Figure 1.12: Classification of skyrmions: Skyrmion texture for Q = 1 and (a) φ = 0; (b) φ = π/2; (c) φ = π; (d) φ = 3π/2, and skyrmion texture for Q = −1 and (e) φ = 0; (f) φ = π/2; (g) φ = π; (h) φ = 3π/2. Figure is taken from the thesis of William Legrand [80].

1.7.3 Different mechanisms to stabilize a skyrmion:

To date, Skyrmions are observed in different magnetic systems. So, there are several mechanisms involved in skyrmion formation, as:

i. It is observed that skyrmions and anti-skyrmions are stabilized via frustrated symmetric exchange interaction [81].
ii. Four-spin interaction also plays a pivotal role in stabilizing skyrmion in a magnetic system [82].

iii. Dipolar interaction stabilizes the skyrmions with a diameter of the order of μm in the multilayer thin films. The dipolar interaction increases the thermal stability of the skyrmions by using repetitive multilayers or by using a reverse bilayer to fulfil the flux closure mechanism [75].

iv. By introducing iDMI, skyrmions with relatively smaller sizes (in order 100 nm) can be stabilized in a thin film [7,74,83].

As DM interaction reduces the texture size and dipolar energy enhances the thermal stability, thus, among the four types of interactions, dipolar and DM interactions have drawn a great research interest to the research community. In this thesis work, we have also concentrated on these two interactions for stabilizing the Néel skyrmions.

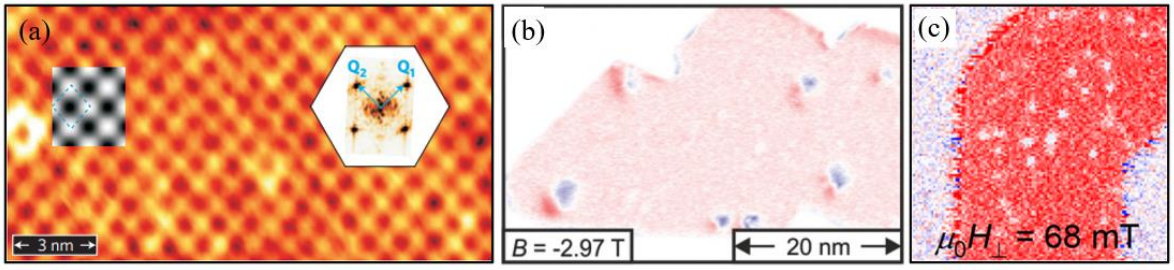

Figure 1.13: (a) Skyrmion lattice imaged via SP-STM at 11 K in Ir (111)/Fe system, image is taken from [82] (b) Isolated skyrmion observed in FePd bilayer at an out-of-plane field of -2.97 T, image is extracted from [84]. (c) Skyrmion observed at room temperature in in a $[Ir|Co|Pt]_{10}$ multilayer, image is taken from [85].

First, Heinze et al. investigated the Néel skyrmion in "skyrmion lattice" form in Ir (111)/Fe system by spin-polarized scanning tunneling microscopy (SP-STM) at 11 K (shown in figure 1.13 (a)) [82]. Later, in 2013, Romming et al. nucleated the isolated skyrmion using the SP-STM tips in a PdFe bilayer, epitaxially grown on Ir(111) substrate [86]. Further, in 2015, the effect of a perpendicular external magnetic field on the skyrmions was investigated (shown in figure 1.13 (b)) [84]. In these works, the skyrmions were stabilized at low temperatures. Hence,

to enhance the thermal stability, Moreau-Luchaire et al., have proposed a multilayer thin film with several numbers of repetitions and stabilized the skyrmion at room temperature (shown in figure 1.13 (c)) [85]. This finding offered a new possibility for practical integration of skyrmions and several other groups made a remarkable advancement in this direction. Further, tuning the thickness of FM, skyrmion has also been stabilized in a single magnetic layer under a very small applied field even at zero field [72,73,87].

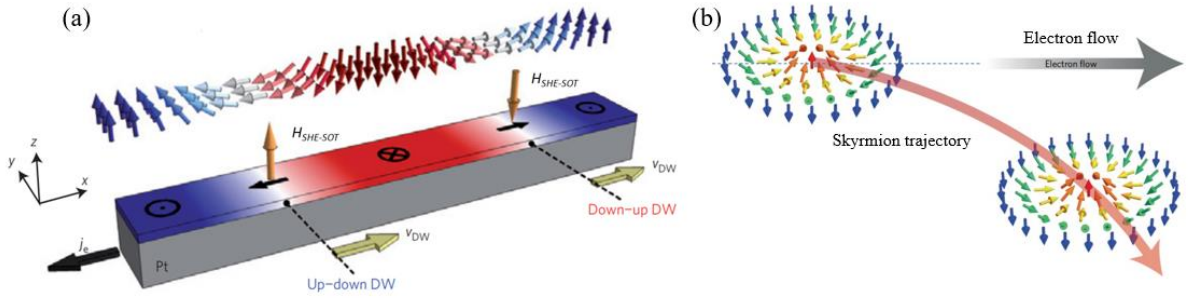

Figure 1.14: (a) Current-driven dynamics of left-hand chiral Néel DWs in a Pt/CoFe/MgO system. The image is taken from Ref. [88] (b) Illustration of skyrmions Hall effect, extracted from Ref. [89]

1.7.4 Dynamics of skyrmion:

Studying skyrmion dynamics is very much essential for practical integration in memory devices. There are several ideas have been proposed to drive a skyrmion. For example, skyrmions can be moved by using a field gradient [90]. Recently, Casiraghi et al., have shown that the stray field of a MFM tip can displace the skyrmions. However, in the case of field-induced motion, a large field gradient is essential to achieve high mobility of skyrmions which limits the application purposes. Another possibility is using spin orbital torque (SOT) which is mostly used by the spintronics community. As iDMI introduces a fixed chirality in a system, so combining with SOT skyrmions can be moved at a high velocity. When current is applied through a sample, mostly it passes through the adjacent HM of a FM due to low resistivity.

Now, due to spin-dependent scattering, an equal number of electrons flow towards opposite directions of HM, each carrying opposite spins which is known as the spin Hall effect (SHE). Thus, a spin gradient is generated inside the HM which injects a spin current, $\mathbf{J_s}$, perpendicularly to the HM/FM interface. If θ_{SHE} is the spin Hall angle then $\mathbf{J_s}$ can be expressed as,

$$\vec{J}_s = -\frac{\hbar}{2e}\theta_{SHE}(\vec{J}_e \times \vec{\sigma}) \tag{1.52}$$

Here, $\mathbf{J_e}$ is the inplane charge current vector. The transmitted spin current interacts with the local magnetization of FM and via transferring the angular momentum it exerts a torque (known as Slonczewski-like torque or SHE-SOT) on the magnetization. The sign and magnitude of the transferred spin current is quantified by the θ_{SHE} which depends on HM and FM combinations. However, due to HM/FM interface, a part of $\mathbf{J_s}$ gets reflected or dissipated, and a reduced effective spin current acts on the magnetization. The θ_{SHE} changes the sign by altering the HM/FM materials position. So far, it has been found that $\theta_{SHE}>0$ for Pt [91] and $\theta_{SHE}<0$ for Ta [92], W [93], Hf [94]. Further, θ_{SHE} also depends on the crystalline structure of the materials [93]. Now the effective field ($H_{SHE\text{-}SOT}$) corresponding to the torque can be written as,

$$H_{SHE-SOT} = \frac{\hbar\theta_{SHE}|j_e|}{2|e|M_s t_F}(\hat{m} \times (\hat{z} \times \hat{j}_e)) \tag{1.53}$$

where M_s, t_F and e are the saturation magnetization, the thickness of FM layer, and the charge of an electron. Due to the effective field, a skyrmion moves through nanotracks. Now to get a clear idea about SHE-SOT-induced dynamics, a simple analogy says a NWs with left-handed chirality have been considered through a nanotrack, as shown in figure 1.14(a). The bottom HM layer is Pt so $\theta_{SHE}>0$ in this case. Now, from equation 1.53, the forces acting on up-down and down-up DW are directed oppositely. Thus, both the DWs move in the forward direction.

However, in the case of achiral DWs, the domain will be shrunk or expanded after applying the current.

Therefore, the skyrmion moves through a nanotrack along the applied current direction (i.e., opposite charge flow direction for Pt and along the charge flow direction of Ta, W, Hf) in a longitudinal motion. However, due to its topological nature, skyrmions got deflected along a transverse direction until they reached the edge of the tracks, as shown in figure 1.14(b). Then due to the repulsive interaction from the edge, either they attain a steady state motion parallel to the track or they annihilate at the edge. The deflection of skyrmion towards the edge is known as 'Skyrmion Hall effect (SkHe)'. A current-induced motion of skyrmion can be explained via the Thiele equation [95,96]:

$$\boldsymbol{F}_{SHE} + \boldsymbol{G} \times \boldsymbol{v} - \alpha D \boldsymbol{v} = 0 \tag{1.54}$$

where $\boldsymbol{G} = 4\pi S$ is the gyrotropic vector, D is the dissipative tensor, α is the Gilbert damping parameter, and $\boldsymbol{v}$ is skyrmion velocity. Hence, the x and y component of the velocity of a skyrmion is [73,97]:

$$\boldsymbol{v}_x = \frac{\alpha D}{G^2+\alpha^2 D^2}\boldsymbol{j}_s, \text{ and, } \boldsymbol{v}_y = \frac{G}{G^2+\alpha^2 D^2}\boldsymbol{j}_s \tag{1.55}$$

where j_S is the spin current generated by the spin Hall effect (SHE). As $G \neq 0$ for FM skyrmions, both longitudinal and transverse are observed in their motion. Therefore, the skyrmion Hall angle (ϕ_{Sk}) defined as, $\phi_{Sk} = tan^{-1}\left(\frac{v_y}{v_x}\right)$. In an ideal case, a zero skyrmion Hall angle is always preferable for its practical integration. However, practically, a finite amount of ϕ_{Sk} is always observed in a thin film. Recent studies reveal that synthetic ferromagnet [98]and ferrimagnetic [99] thin films induce a minimal ϕ_{Sk} than a single metallic thin film.

Chapter 2

Experimental techniques

In this chapter, we have described all the experimental techniques which are used in the thesis work. All the metallic layers (Ta, Pt, Re, Ru, Co and CoFeB) are deposited via magnetron sputtering and the MgO layer is deposited via e-beam evaporation on 100 nm thermally oxidized Si substrates. The nano-tracks of the samples are prepared via electron beam lithography (EBL) techniques. The structural information of the thin films is investigated via X-ray diffraction and X-ray reflectivity methods. The magnetic characterization of the samples has been performed via magneto-optic Kerr effect (MOKE), magnetic force microscopy (MFM) and superconducting quantum interference device (SQUID) magnetometry. The domain wall (DW) dynamics of the samples are performed via Kerr microscopy. Further, the iDMI constant for the thin films is quantified via Kerr microscopy as well as Brillouin Light Scattering (BLS) technique. Electric measurements of the samples have been performed by a physical properties measurement system (PPMS). The DW dynamics measurements, iDMI quantification and MFM measurements for Pt/Co samples are performed in our lab at NISER. For Pt/CoFeB samples, DW dynamics measurements, BLS and MFM measurements are performed via a collaboration (via Indo-French CEFIPRA project) with Prof. Stanislas Rohart at Laboratoire de Physique des Solides (LPS), Paris-Saclay University, France. Via the CEFIPRA project I could visit LPS in Orsay to participate in the experiments. Further, to verify

the experimental findings, we have performed micromagnetic simulations using MuMax3 software.

2.1 Sample fabrication:

2.1.1 Thin film deposition techniques:

The thin film deposition technique plays a pivotal role in recent technology and R&D sections. Thin films are widely used in solid-state devices, electronic displays (i.e., Liquid crystal displays (LCD), light-emitting diode (LED) and fluorescent displays), optical coatings, etc. Particularly, magnetic thin films are extensively used in modern data storage technology, many magnetic sensors and circuits.

There are mainly two different methods that have been used to fabricate a thin film, 1. Chemical vapour deposition (CVD) and 2. Physical vapour deposition (PVD). CVD is a chemically reactive process where the desired surface or substrate is exposed to the gaseous phase of one or more chemicals [100]. PVD is associated with vacuum deposition processes where the depositing materials are evaporated or otherwise atomized from solid sources [101]. However, PVD is more advantageous than CVD techniques as no hazardous gases and chemicals are involved and very good quality thin films can be achieved at room temperature (RT). In the thesis work, PVD techniques such as sputtering and e-beam evaporation have been used to deposit the thin films.

2.1.1.1 Sputtering:

Sputter deposition is a widely used popular technique to deposit thin films on substrates. The main advantages of this technique are to deposit a large area with high uniformity and ability to sputter both conducting and insulating materials. In this process, the atoms deposited on the substrate are achieved by a bombardment of the target by energetic ions of an inert gas (plasma)

in a vacuum chamber [102]. In our deposition system, argon (Ar) gas is used as an inert gas to create the plasma. A sufficiently high negative bias voltage is applied to a cathode (target) which repels the electrons coming from the cathode (sputtering target). The electrons move far away from the target and collide with the Ar atoms. Therefore, Ar gas got ionized and the Ar^+ ions are accelerated towards the target. Further, the Ar^+ ions hit the target and transfer the momentum via elastic and inelastic scattering. The target atoms are then ejected from the surface and get deposited on the top of the substrate if the substrate is mounted within the line of view (solid angle) of the ejected atoms. The secondary electron released from the target due to the bombardment of Ar^+ ions help in generating the denser plasma of Ar^+. Figure 2.1 shows a schematic of the sputtering process. In the process, the flow rate of Ar gas must be increased to achieve a high deposition rate. However, a high flow rate of Ar during the deposition increases the number of collisions of target atoms with Ar-atmos or ions and decreases the mean free path of target atoms. This may degrade the deposited film quality. To overcome the issue, a magnetron sputtering technique is proposed in which a co-axial permanent magnet with opposite polarity is placed just below the target (magnet geometry is shown in figure 2.1) [103,104]. Now, due to the magnetic field (that induces the Lorentz force) the secondary electrons are trapped and increases the probability of ionization of Ar atoms near to target. The increased ionization efficiency enhances the plasma density and deposition rates. However, a balanced magnet configuration confines the plasma near to target and decreases the range of plasma. So, the distance between the target and substrate should be minimal in this case which constraints the chamber size, deposition voltage, deposition rates, etc. Using an unbalanced magnet configuration, the range of plasma can be enhanced significantly. In an unbalanced magnet, the outer ring magnet is stronger than the inner axial magnet. Consequently, the uncompensated field line as well as plasma extended towards the substrate and the yield becomes near to the substrate.

There are two different types of sputtering techniques available depending on the conductivity of the target materials i.e. (i) direct current (DC) sputtering (ii) radio frequency (RF) sputtering.

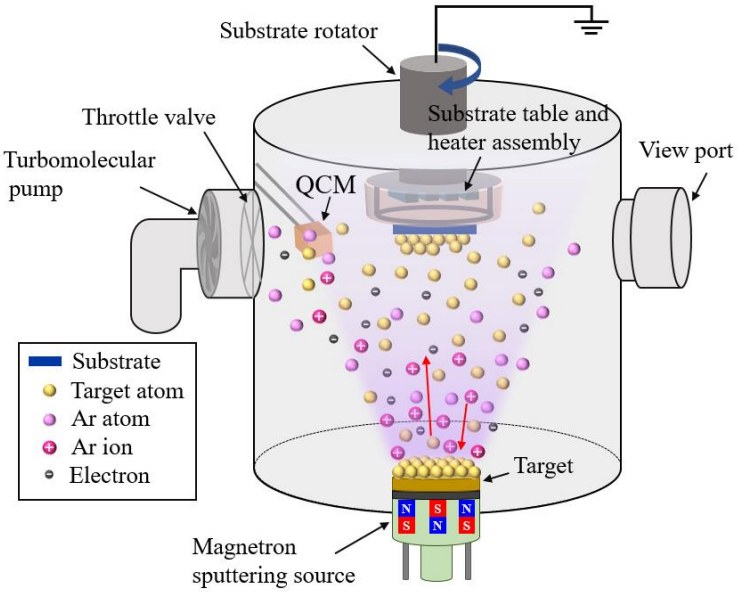

Figure 2.1: A schematic of the sputtering deposition technique in a vacuum chamber. The violet colour solid cone represents the plasma. Different atoms, involved in the process, are shown in different colour. Different components of a sputter deposition chamber are shown.

(i) DC sputtering: This technique is used to deposit a conducting material. During deposition, a constant direct current (DC) is applied to the target (cathode). Due to the conducting nature of the target, the applied negative bias is distributed uniformly throughout the target. The Ar^+ ions are attracted by the target and after bombardment with the target, it gets neutralized via transferring the charge. However, for an insulating target, the applied negative bias is not distributed uniformly through the target surface resulting in Ar^+ ion accumulation and the plasma starts disappearing. Therefore, insulating materials cannot be deposited via DC sputtering.

(ii) RF sputtering: This technique is mainly used to deposit non-conducting insulating or dielectric materials. Here, an alternating current is applied to the target during the deposition

to overcome the positive (Ar+) charge accumulation problem. Usually, a radio frequency of 13.56 MHz is used for a RF power source. During the deposition, a potential is applied via two half-cycles in each of the RF cycles. While negative potential is applied, the Ar+ ions bombard the target and the target atoms get ejected from its surface. However, as the target is insulating, the positive charge keeps growing on the surface of the target until the target repels any additional positive bombardment. Next, during the positive half of the cycle, electrons are attracted towards the target surface and after bombardment, it neutralizes the target by removing the Ar+ ions. However, a self-bias voltage also arises in RF sputtering due to the higher mobility of electrons in comparison to the ions present in the plasma. The RF field provides mobility to the ions and electrons present in the plasma. However, owing to their lighter mass and smaller size, electrons exhibit greater mobility compared to ions. Consequently, they respond more readily to changes in the RF field. Therefore, in the positive cycle of the RF field, a large number of electrons impinge on the target material. These bombardments of negatively charged particles result in the accumulation of a negative voltage on the target surface, known as the self-bias voltage. This negative voltage in turn increases the energy of the ions accelerating towards the target material. Such highly energetic ions eject more atoms from the target material upon bombardment. Thus, the self-bias voltage helps to increase the energy and rate of sputtered atoms ejected from the target material during RF sputtering. The RF sputtering can be used to deposit both conducting and non-conducting materials. However, the deposition rate is lower in this technique than DC sputtering, as the deposition occurs here only in a negative half cycle [105]. To achieve a high deposition rate via RF sputtering, higher voltage is required resulting in overheating issues of the target. Therefore, a cooling facility is very necessary for RF sputtering.

2.1.1.2 E-beam evaporation:

Electron beam (e-beam) evaporation is a form of PVD technique. Here, the target rod/crucible (where target materials are kept) is biased at a very high positive voltage (~ +2000 V) and is placed near a tungsten filament. When sufficient current passes through the filament, the filament undergoes thermionic emission, releasing electrons. Then, a stream of electrons is drawn from the filament towards the rod/crucible. The electron stream impacts on the surface with high energy and causes heating which will lead to the evaporation of target materials. The ejected target atoms travel in a vacuum chamber and then precipitate to form a uniform thin film coating on a substrate. The target materials possess very low thermal energy (<1eV). Therefore, a high vacuum chamber is essential for this technique so that the mean free path of target atoms is larger than the separation between the e-beam source and substrate. In addition, higher deposition rates may be achieved using electron beam evaporation, ranging from 0.1 nm to 100 nm per minute. Here, the energy mainly transfers to the target rather than the whole system which reduces the possibility of damaging the substrate [106].

We have used a QPrep multi-deposition system manufactured by Matis deposition Ltd. UK, to deposit the thin films for the thesis work (see figure 2.2 (a)). This system has two main parts one main chamber and another one load-lock. The main chamber and load lock are separated by a gate valve. Both the main chamber and load lock are equipped with turbo molecular pumps (TMP) and scroll pumps. Using the load lock the samples are transferred to the main chamber without breaking the vacuum of the main chamber. The maximum base pressure of 5×10^{-10} mbar can be achieved in the system. The system pressure is measured via INFICON (BPG400) full range gauge. To control the system pressure during deposition, one additional throttle value is placed just before the main chamber TMP. The thickness of the samples is monitored via a quartz crystal monitor (QCM). To achieve uniformity in the prepared thin film, the substrate

table can be rotated up to 20 rpm. Also, the substrate table can be heated up to 800°C. The various deposition units of the system are listed below:

i. Five unbalanced magnetron sputtering sources (DC and RF)

ii. A four-pocket e-beam evaporator

iii. Two thermal evaporators

iv. One nanoparticle generator source (Nano gen)

v. A Mat-60 unit produces the atomic O_2 from its molecules.

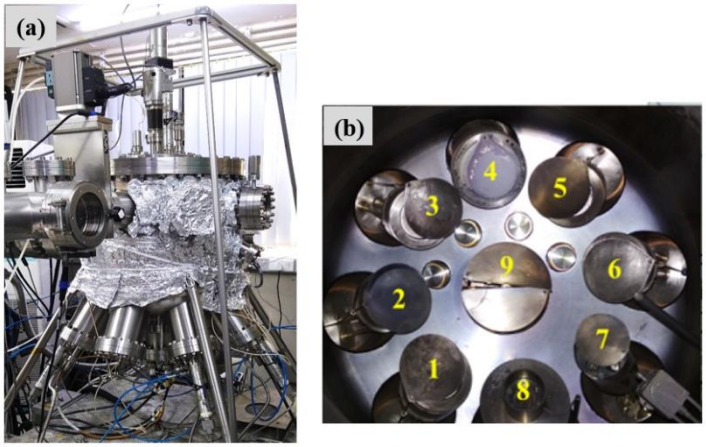

Figure 2.2: (a) Multi deposition chamber manufactured by MANTIS present in our lab at NISER. (b) Top view of the system. The numbers correspond to different deposition sources. 1-3 are the DC sputtering sources, 4 is the MAT60, 5-6 are the RF sputtering sources, 7 is the e-beam evaporator, 8 is the NanoGen source and 9 is the thermal evaporator.

In this chamber, eight equidistant sources are placed at the lower periphery (45° from each other in the horizontal plane) and the thermal source is positioned exactly at the centre of the lower bottom part (see figure 2.2 (b)). The eight sources are placed in a tilted way where the tilt angle is 30° w.r.t substrate normal. Thus, uniaxial anisotropy is induced along the perpendicular direction to the plume's inplane projection and support the columnar growth of the grains along the easy axis [107]. Due to the columnar growth, the long axis of the

crystallites can form a chain like structure which may lead to a uniaxial anisotropy [107]. All the sources and the substrate table are protected via motorized shutters.

2.1.2 Electron beam lithography:

Lithography is a technique which helps to fabricate a sample in a nanoscale dimension. Here, different kinds of radiation sources (i.e. UV-light, e-beam, photon, etc.) are used to expose a chemically activated medium known as photoresist. Among them, electron beam lithography is a very sensitive technique to prepare pattern samples with resolution in tens of nanometers using e-beam as a radiation source [108]. Here, a positive or negative e-beam resist can be used as a chemically activated medium. Polymethyl methacrylate (PMMA) is a widely used very popular +ve e-beam resist. Figure 2.3 shows the process of the EBL technique. In this method, first, the substrate is coated by a uniform thin layer of PMMA using the spin coater and baked at a certain temperature for 5-10 minutes. Then the substrate is placed inside the instrument and the e-beam is directed toward the sample surface through a path designed via computer with CAD software which basically defines the desired nanostructures. Now the sample is developed in a mixed solution of isopropanol (IPA) and methyl isobutyl ketone (MIBK) in a 3:1 ratio where the exposed part of e-beam resist will be dissolved. Then the desired material is deposited on the patterned substrate via any deposition techniques. After deposition lift-off process is performed in acetone using ultrasonic agitation to remove the unexposed resist and a nanostructure can be fabricated [109].

In the thesis work, to fabricate the nano-tracks, the EBL technique is performed at Laboratoire de Physique des Solides (LPS), Paris-Saclay University, France for studying the current induced dynamics of skyrmion. Here, we have first prepared the thin film sample before fabricating the nano-tracks. After preparing the sample, it is coated with Methyl methacrylate (MMA) via spin coating (2000 rpm for 1min) and baked at 100°C for 10 minutes. Then again

it is coated with PMMA (3000 rpm for 1min) and baked at 100°C for 10 minutes. Then the sample is exposed to e-beam to prepare the desired pattern. After development, a certain thickness of Al (Al mask) is deposited via sputtering on the pattern sample. Then, via lift-off, the excess unexposed e-beam resist is removed and only nano-tracks of Aluminium (Al) will remain on the top of the sample. Finally, via ion-beam etching, we have prepared a nano-track of the sample.

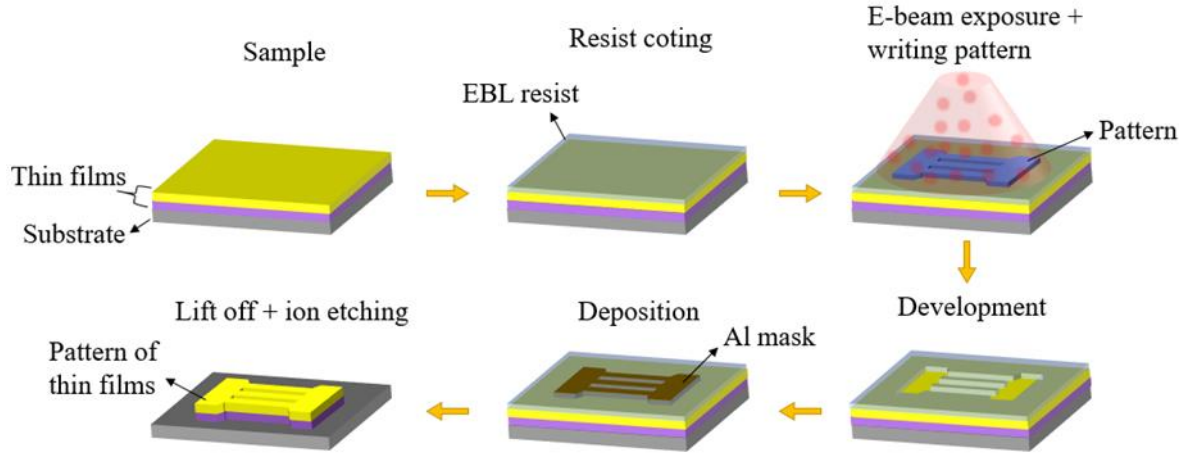

Figure 2.3: Schematic of the E-beam lithography (EBL) process.

2.2 Structural Characterization:

2.2.1 X-ray diffraction:

X-ray diffraction is a very popular technique to characterize the structural information of a sample i.e., crystal structure, site occupancy, atomic arrangement, crystallite size, imperfections, etc., because the wavelength of X-ray is (~0.1 nm) comparable to the atomic spacing of crystal [110,111]. In this technique, an X-ray beam is incident on a sample and gets diffracted by crystalline atoms. A crystal can be considered as a periodic arrangement of atoms scattering the incident X-rays elastically. As per Bragg's law, the scattered X-ray beam interferes constructively if the path difference between two consecutive rays is the integral multiple of wavelength (λ) [112]. If d is the interplanar separation and θ is the incidence angle

(glancing angle) of X-rays then the path difference between two rays diffracted from the consecutive plane is:

$$2d\,sin\theta = n\lambda \tag{2.1}$$

For specific systems, λ is constant so the constructive interference pattern depends only on d and θ. Here, n is the order of interference. The intensity of the interference pattern decreases with increasing the order, n. While performing the measurements, the angle of incidence is varied from 0 to 90° in small steps. Then the intensities of the reflected beam are measured as a function of the angle (2θ) between reflected rays and the direction of incident rays. For a constant value of θ, the interplanar separation d for a film can be quantified using equation 2.1. Further, the lattice parameters (a) also can be calculated using the formula, $d = a / (h^2 + k^2 + l^2)^{1/2}$, where ($h$, k, l) is the miller indices of the corresponding plane [113].

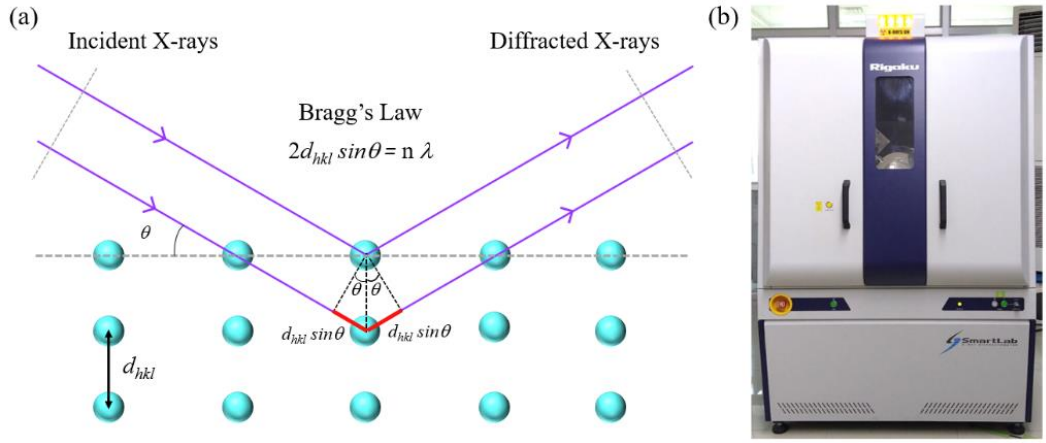

Figure 2.4: (a) A schematic of the X-ray diffraction phenomenon. (b) The automated multipurpose X-ray diffractometer (SmartLab) is manufactured by Rigaku at NISER.

We have measured the thin film samples of the thesis work using an automated X-ray diffractometer (SmartLab) manufactured by Rigaku Corporation, Japan [114,115]and a D8-Advance reflectometer provided by Bruker Corporation, USA [116] (shown in figure 2.4 (b)).

A Cu K_α source (λ = 0.154 nm) is used for both SmartLab diffractometer and D8-Advance reflectometer.

2.2.2 X-ray reflectivity:

X-ray reflectivity (XRR) is another technique for X-rays to probe the internal structure of a sample. This technique is used to measure the thickness, roughness and density of a deposited thin film. The technique is independent of material crystalline quality. Depending upon the detector quality, it can determine the multilayer film thickness from a few angstroms to several hundred of nanometers. While a beam of X-rays is incident on a thin film, the refractive index is modified as,

$$\tilde{n} = 1 - \delta + i\beta \tag{2.2}$$

with $\delta = \frac{\lambda^2}{2\pi} r_e \rho_e$ and $\beta = \frac{\lambda}{4\pi}\mu$ [117,118]. Here, λ denotes the wavelength of X-rays, r_e, ρ_e and μ represent the radius, density, and absorption length of the electron, respectively. As ρ_e depends on the density of a material, consequently, δ gives the information about the density of the thin film. Now, if θ_i and θ_t are the incidence and transmission angle, respectively, then according to Snell-Descartes law (see figure 2.5 (a)),

$$n \cos\theta_i = \tilde{n} \cos\theta_t \tag{2.3}$$

with n is the refractive index of air (=1). For Specular reflection, the θ_i is equal to θ_f. As for XRR measurements, a hard X-ray beam is used and a very small amount of X-rays get observed by the thin film. Therefore, β is very small and can be ignored. Now the equation (2.2) is modified as, $\tilde{n} = 1 - \delta$. After using the value of n (=1, for air) and $\tilde{n}$, equation (2.3) can be written as,

$$\cos\theta_i = (1 - \delta)\cos\theta_t \tag{2.4}$$

If the incidence angle of X-rays is very small then it gets reflected from the surface. Therefore, for a critical angle of $\theta_i = \theta_c$, total external reflection occurs with $\theta_t = 0$. Then equation 2.4, modified as, $cos\ \theta_c = (1 - \delta)$. Using the Taylor series expansion and neglecting the higher-order terms, $cos\ \theta_c$ represented as $1 - \frac{\theta_c^2}{2}$, therefore, $\theta_c = \sqrt{2\delta}$ [110]. As δ gives the information about the material density, θ_c can provide the knowledge about the density (ρ) of the thin film. For total external reflection, maximum intensity is observed by the detector. However, while $\theta_i > \theta_c$, some amount of the X-ray beam gets absorbed by the thin film and the intensity of reflected rays gets reduced. For $\theta_i > \theta_c$, the Fresnel's reflection coefficient (r) can be written as,

$$r = \frac{n \sin\theta_i - \tilde{n} \sin\theta_t}{n \sin\theta_i + \tilde{n} \sin\theta_t} \tag{2.5}$$

Now, using Snell-Descartes law for small values of θ_i, the reflection coefficient, r, for ideal flat surfaces can be represented as,

$$r = \frac{\theta_i - \sqrt{\theta_i^2 - \theta_C^2}}{\theta_i + \sqrt{\theta_i^2 - \theta_C^2}} \tag{2.6}$$

Thus, the intensity (I) of the X-ray reflectivity curve can be represented as,

$$I = R(\theta) = r\, r^* = \left| \frac{\theta_i - \sqrt{\theta_i^2 - \theta_C^2}}{\theta_i + \sqrt{\theta_i^2 - \theta_C^2}} \right|^2 \tag{2.7}$$

Now depending on the value of θ_i, there conditions arise:

a. For $\theta < \theta_c$, $I = R(\theta) = 1$; i.e., the maximum intensity of the X-rays beam is received at the detector.
b. For $\theta = \theta_c$, I start reducing significantly, as shown in figure 2.5 (b).

c. For θ >> θ_c, *I* get reduced as $\frac{1}{\theta^4}$.

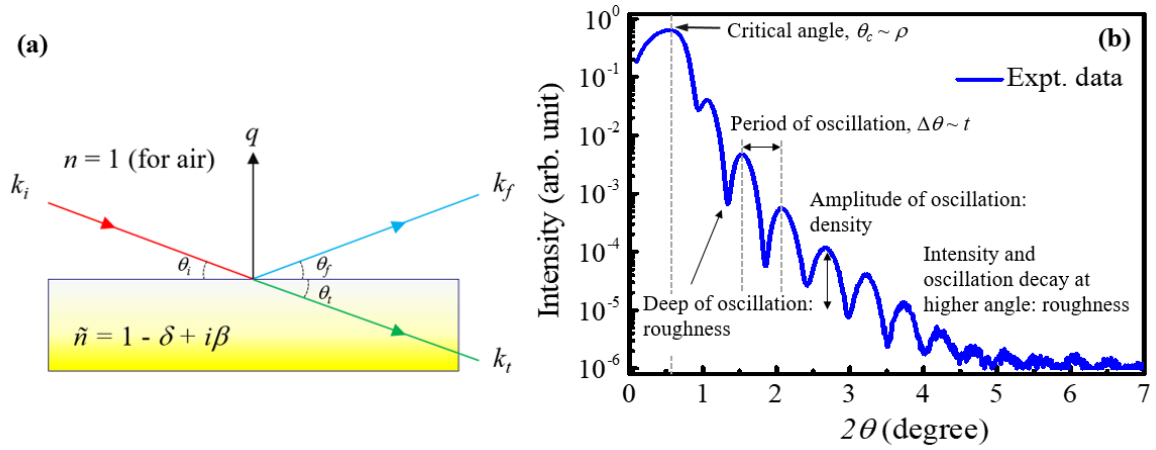

Figure 2.5: (a) Schematic of X-ray reflection method in specular geometry and k_i, k_f and k_t are the wave vector of the incident, reflected and transmitted X-rays, respectively. (b) A typical XRR spectrum where the intensity of the reflected beam is plotted as a function of 2θ.

While X-rays penetrate a thin film, the reflection arises from both the bottom and top surface of the film. Therefore, both constructive and destructive interference appear and form the Kiessig fringes in the reflectivity. The thickness of a single layer of thin film is simply determined using Bragg's law, $t = \frac{\lambda}{2\Delta\theta}$. Here, *t* denotes the film thickness and $\Delta\theta$ represents the difference between two consecutive minima or maxima in the XRR fringes. However, in real case, the sample surface is not perfectly smooth. The roughness of thin film introduces the off-specular reflection, consequently, the amplitude of oscillation and intensity of reflected X-rays get reduced. Therefore, a new term (corresponds to the roughness of film) is added to Fresnel's reflection coefficient and modified as [110],

$$r_r = r_f e^{-\frac{q^2\sigma^2}{2}} \tag{2.8}$$

where $q = \frac{4\pi}{\lambda}\sin\theta$ and σ is the surface roughness. The r_r and r_f is the reflection coefficient of rough and flat surfaces, respectively.

Now for a multilayer thin film, the situation is very different than a single-layer thin film as the reflection and transmission arises from each layer. Therefore, a rigorous calculation is required for each layer. To overcome the problem, Parratt introduced a recursive formalism. Most of the commercially available X-ray reflectivity simulator is designed based on the Parratt formalism. After fitting the experimental data using those simulators, the thickness, roughness, and density of the thin film can be determined.

In this thesis work, the XRR measurements for all the samples are performed using a Smartlab diffractometer manufactured by Rigaku Corporation Ltd., Japan [114]. The measured data are analyzed via GenX software which is designed using Python script with Parratt formalism [119,120].

2.3 Magnetic characterization:

2.3.1. Superconducting quantum interference device (SQUID) magnetometry:

Superconducting quantum interference device (SQUID) magnetometry is the most sensitive instrument for the detection of magnetic flux [121,122]. It is extremely sensitive to detect a low magnetic moment of ~ 10^{-8} emu. Also, it has been used in various applications such as nuclear magnetic resonance, susceptometry, scanning SQUID microscopy, etc. In SQUID, the Josephson effect is used to detect the small variations in magnetic flux. Typically, a SQUID consists of two rings of superconductor interrupted by one or more Josephson junctions [123]. Here, the superconductors are separated by a thin insulating layer. The supercurrent (I_s) is generated via tunnelling the copper pairs in between the superconductors. Each superconductor can be considered as a single wave function due to the existence of phase coherence in all cooper pairs. Therefore, two superconductors can be expressed via two different wave functions that possess different phases. Now, the solution of Schrödinger equations for these two superconductors gives expression of the supercurrent as, $I_s = I_0 \sin(\varphi_2 - \varphi_1)$, with I_0=

the critical current and $(\varphi_2 - \varphi_1)$ = the phase difference. Additionally, by applying the magnetic field the phase of the quantum state can be modified. The total quantized phase can be expressed as,

$$\Delta\varphi(B) + \Delta\varphi(I) = 2\pi n \tag{2.9}$$

Therefore, a change in the magnetic field that is closely related to the flux quantization is the major reason for the great sensitivity of SQUID. During the measurement, the sample is placed inside superconducting wires which are known as second-order gradiometer coils. The top and bottom coils are consisted of a single turn in a clockwise manner. Whereas, the middle coil is

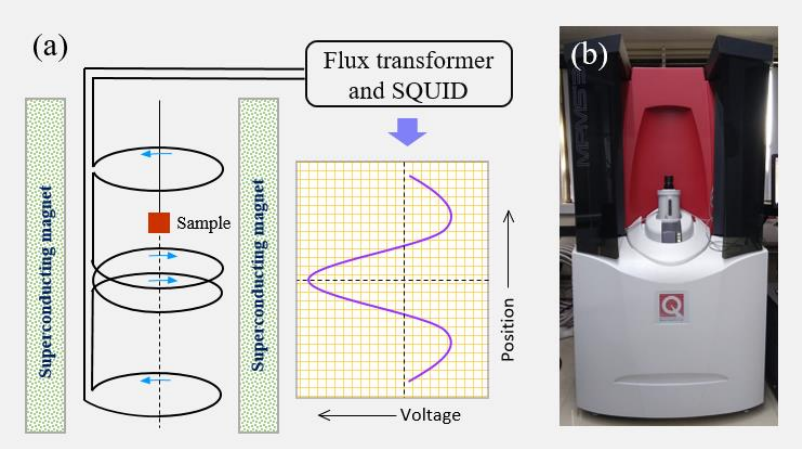

Figure 2.6: (a) A schematic representation of SQUID magnetometer. (b) The MPMS3 SQUID available in our lab at NISER.

made of with double turn in an anti-clockwise manner. The coils are placed in between two superconducting magnets which produces a uniform magnetic field throughout the coil's region (see figure 2.6 (a)). While the sample moves vertically up and down, generates the alternating magnetic flux in the pick-up coil. The associated magnetic flux induces a persistent current in the coils. Further, the magnetic flux is transferred to RF-SQUID to convert it into a corresponding voltage signal. The voltage signal is then transformed to the magnetic moment of the sample and finally, it is measured with respect to scan position.

In the thesis work, the magnetization and magnetic anisotropy of all the samples are measured via an MPMS3 system manufactured by Quantum Design, USA (shown in figure 2.6 (b)). A maximum ±7 T magnetic field can be applied and the temperature can be varied over a wide range from 1.8 K to 400 K in the instruments [124].

2.3.2 Magneto-optic Kerr effect (MOKE) based microscopy:

The magneto-optic Kerr effect (MOKE) based microscopy technique is a very popular technique for hysteresis measurements, domain imaging, domain wall (DW) dynamics measurements, anisotropy quantification, etc [125–128]. This technique is based on the magneto-optic Kerr effect, which can be explained via the dielectric theory as well as the microscopic quantum theory [129,130]. Here, the rotation of the plane of incidence of a polarized light occurs after the reflection from a magnetic sample. A linear polarized light is superimposed of left circularly polarized (LCP) and right circularly polarised (RCP) light with equal amplitude i.e. $E_L=E_R=E/2$. Now the electric field of LCP (RCP) light moves the free electron of the magnetic sample in left (right) circular motion. Therefore, it can be considered that the electron rotating around a positive charge forms an electric dipole. The corresponding radius of the circular path of an electron can be determined from the equilibrium condition of all acting forces and written as,

$$r_{L,R} = \frac{\frac{eE}{2m_e}}{\omega^2-\omega_0^2} \tag{2.10}$$

where, $r_{L,R}$, e, E, ω and $\omega_0 (= \sqrt{\frac{k}{m}})$ are the radius of the circular path of the electron (L, R in the subscript is for left and right circular light), charge of an electron, electric field, angular frequency of light, and a constant of the material, respectively [125,126,131,132]. Hence the displacement vector can be represented as, $\boldsymbol{D} = \epsilon \boldsymbol{E} = (\epsilon_0 \boldsymbol{E} + \boldsymbol{P})$, where, P, ε, ε_0 are the polarization of the medium, permittivity of the medium and permittivity of free space,

respectively. Now if N is equal to the number of dipole moment/volume, then the dielectric constant of the medium can be written as,

$$\epsilon_r = \frac{\epsilon}{\epsilon_0} = \left(1 + \frac{\frac{Ne^2}{2m\epsilon_0}}{\omega^2 - \omega_0^2}\right) \tag{2.11}$$

In the absence of any applied field, the LCP and RCP light experience the same refractive index as the dielectric constant is the same. However, presence of an applied magnetic field, Lorentz force arises which tries to push the electron motion either towards or away from the nucleus depending upon the polarity of light. Therefore, the radius of the left (right) circular electron's motion contracts (expands) which can be written as,

$$r_{L,R} = \frac{\frac{eE}{2m_e}}{\omega^2 - \omega_0^2 \mp \frac{\omega Be}{m_e}} \tag{2.12}$$

The two different radii of left and right circular motion induce two different dipole moments, hence two different dielectric constants appear. As the dielectric constants of a material are related to the refractive index (n), therefore, the refractive index for left (n_L) and right (n_R) circular light also be different leading to different velocities in the propagation of lights. This phenomenon is analogous to the birefringence of circularly polarised light which introduces a phase difference ($\Delta\theta$) between the oppositely polarised light waves with $\Delta\theta \propto (n_L\text{-}n_R)$. As a consequence, the plane of polarization of reflected light is rotated which is known as Kerr rotation (θ_K). As the θ_K arises due to Lorentz force which is induced in a magnetic sample via an external applied magnetic field ($\boldsymbol{B}$), it can be concluded that θ_K is proportional to B ($\theta_K \propto B$). Again $\boldsymbol{B} = \mu_0 \boldsymbol{M}$, where $\boldsymbol{M}$ = magnetization of the sample, so θ_K is proportional to $\boldsymbol{M}$. Now if the amplitudes of LCP and RCP wave become different, the reflected light contains an additional contribution known as ellipticity (ϵ_K) along with θ_K. In this case, the dielectric constant transforms to a complex parameter and the macroscopic origin of magneto-optic

effects can be explained by dielectric tensor theory, $\boldsymbol{D} = \boldsymbol{\varepsilon}\boldsymbol{E}$ where $\boldsymbol{\varepsilon}$ is an antisymmetric tensor. The relation can be written as [125,126],

$$\boldsymbol{D} = \varepsilon(\boldsymbol{E} + iQ\boldsymbol{m} \times \boldsymbol{E}) \tag{2.13}$$

where Q is a material-dependent parameter, proportional to the saturation magnetization and denotes the strength of Kerr rotation. Now, the magneto-optic effect arises due to the antisymmetric off-diagonal elements in the 3 × 3 dielectric tensor while the symmetric part of the dielectric tensor has no effect. Therefore, it can be written as [125,126],

$$\boldsymbol{\varepsilon}' = \boldsymbol{\varepsilon}\begin{pmatrix} 1 & iQ_v m_z & -iQ_v m_y \\ -iQ_v m_z & 1 & iQ_v m_x \\ iQ_v m_y & -iQ_v m_x & 1 \end{pmatrix} \tag{2.14}$$

here, Q_v represents the Voigt constant and $(m_x, m_y, m_z) = \boldsymbol{m}$ is the normalized magnetization vector. Now the 2nd term of the equation 2.13 is very similar to Lorentz force. Thus, the Kerr amplitude (K) can be calculated by projecting Lorentz movement (parallel to the second term in equation 2.13) in a plane perpendicular to the propagation direction of the reflected light (see figure 2.7 (a)). If N is defined as the amplitude of reflected light in the same plane as the incident light, then K is perpendicular to N. For small angle approximation, θ_K can be written as, $\theta_K = \frac{K}{N}$ (see figure 2.7 (a)). For oppositely aligned magnetization, the Lorentz force acts in a reverse direction, therefore, the K changes sign. Now the domain contrast is achieved by blocking the reflected light from one type of domain and allowing the light from the reverse domain using an analyzer. The difference between the black and dark intensities provides the relative Kerr contrast which is expressed as [125],

$$S = 4\beta KN \tag{2.15}$$

β is the angle created by the analyzer and N is shown in figure 2.7 (b). Now, it should be noted from equation 2.15 that (1) Kerr signal (S) is linearly proportional to the Kerr amplitude (K), therefore, S is also linearly proportional to the respective magnetization components, (2) The intensity of the Kerr signal can be enhanced by increasing the analyzer angle, β, beyond θ_K, which may lead to enhancement in signal-to-noise ratio, (3) The visibility of domains is defined by the Kerr amplitude and not by the Kerr rotation.

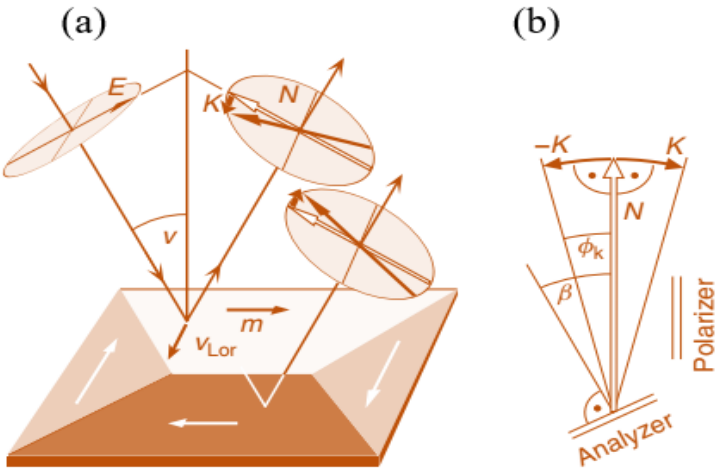

Figure 2.7: (a) Illustration of magneto-optical interaction in longitudinal geometry. The magnetization (m) of the sample is parallel to the plane of incidence of polarized light. The electric field (E) of incident light combined with m of the sample generates the Lorentz motion (v_{Lor}) of the electrons. The Kerr amplitude (K) is obtained by projecting the v_{Lor} onto the plane perpendicular to the direction of propagation of the reflected light. (b) The relative configuration of the analyzer and polarizer are displayed with respect to the normally reflected amplitude (N) and Kerr amplitude (K). The picture is taken from ref. [125]

There are three different geometries in MOKE which are observed depending upon the magnetization direction and plane of incidence of the polarized light, as shown in figure 2.8.

i. Longitudinal Mode: The magnetization direction of the sample is parallel to both the sample plane and plane of incidence of the polarised light (see figure 2.8 (a)).

ii. Transverse Mode: The magnetization direction of the sample is parallel to the sample plane and perpendicular to plane of incidence of the polarised light (see figure 2.8 (b)).

iii. Polar Mode: The magnetization direction of the sample is perpendicular to the sample plane and parallel to the plane of incidence of the polarised light (see figure 2.8 (c)).

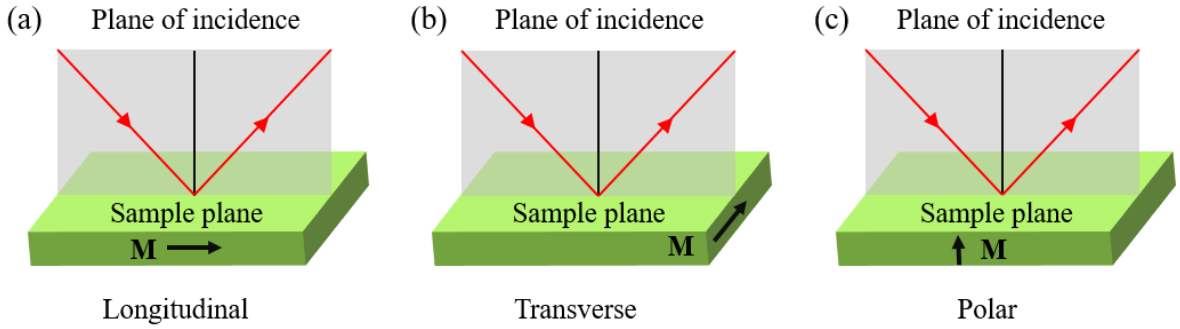

Figure 2.8: Schematic representation of different geometry of MOKE microesope.

Figure 2.9 (a) reveals a schematic of the Kerr Microscopy set-up. First, an unpolarised light emerging from a LED source is passed through a polarizer and converted into linearly polarised light. The polarized light incident on the sample. For simplicity, we consider that the sample consists of two domains having opposite spontaneous magnetization. After reflection, the polarized lights (say beam 1 and beam 2) rotate equally in opposite directions due to the Kerr effect as described earlier and transform to elliptical polarized light. Therefore, a variable quarter wave plate is used to compensate for the phase shift before the analyzer. Now, the axis of the analyzer is rotated in such a way that it blocks one of the reflected beams completely (beam 2) and allows the other ray (beam 1) which correspond to dark and bright contrast in the image plane. The two different image contrasts define the two different domain states of a sample.

The magnetization reversal and corresponding domain imaging of the samples related to this thesis work are studied via Kerr Microscopy manufactured by Evico Magnetics Ltd., Germany (see figure 2.9 (b)) [133]. It consists of eight LED sources and by selecting the proper combination of LED lights the sensitivity of the measurement can be chosen conveniently [134]. A maximum resolution of ~ 300 nm can be achieved using an oil immersion objective. In in-plane mode, we can apply a maximum field of 1.3 T whereas, in out-of-plane mode, a maximum 0.9 T field can be applied using an electromagnetic coil. All the electromagnetic coils are attached to a cooling facility to avoid the extra heating issue. The in-plane sample stage can be rotated from 0 to 360° with a small step of 1°. Therefore, this can be used to investigate angle-dependent magnetic features such as magnetic anisotropy, hysteresis, and domains. We have also performed the domain wall dynamics and iDMI quantification using this instrument.

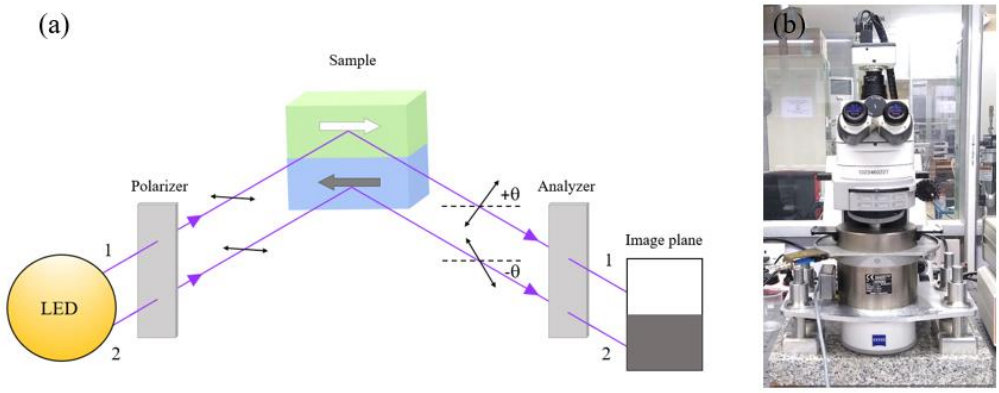

Figure 2.9: (a) A conventional domain image formation method. In image plane two different colours represent the two opposite domain state. (b) Image of Kerr microscope set up available in our lab at NISER.

i. Field-induced domain wall velocity measurement:

Domain wall (DW) dynamics in perpendicular magnetic anisotropic (PMA) systems have potential applications in a wide scale of magnetic devices, such as DW-based racetrack

memory, logic devices, and spin memristors for mimicking synapse in an artificial neural network [135–137]. Therefore, the determination of the DW velocity of a PMA system is very important. Here, we have performed Kerr microscopy to measure the DW velocity. To study the DW dynamics, a pulsed magnetic field is necessary which can be generated via a solenoid coil. If we consider a coil of N number of turns with inner radius r, then the magnetic field, H, generated at the center of the coil is $H = \frac{\mu_0 NI}{2r}$, where μ_0 is the permeability of the vacuum and I is the applied current. The corresponding inductance, L, of the coil, is $L = \frac{\mu_0 \pi N^2 r}{2}$. Therefore, H and L increase with the number of turns of the coil (N). Now the rise time of the coil can be written as $\tau = \frac{L}{R_{total}}$, where L is the inductance and R_{total} is the total resistance of the circuit ($R_{coil} + R_{circuit}$). Now, the strength of the magnetic field can be enhanced by increasing the N and I and reducing r. Again, enhanced N, increases the inductance (L) which enhances the rise time (τ) of the coil. A coil with high τ opposes to apply pulses of small duration. Therefore, to maintain a proper balance of H and L, N should be chosen carefully. The current through the coil should also increase properly otherwise it may be damaged via Joule heating.

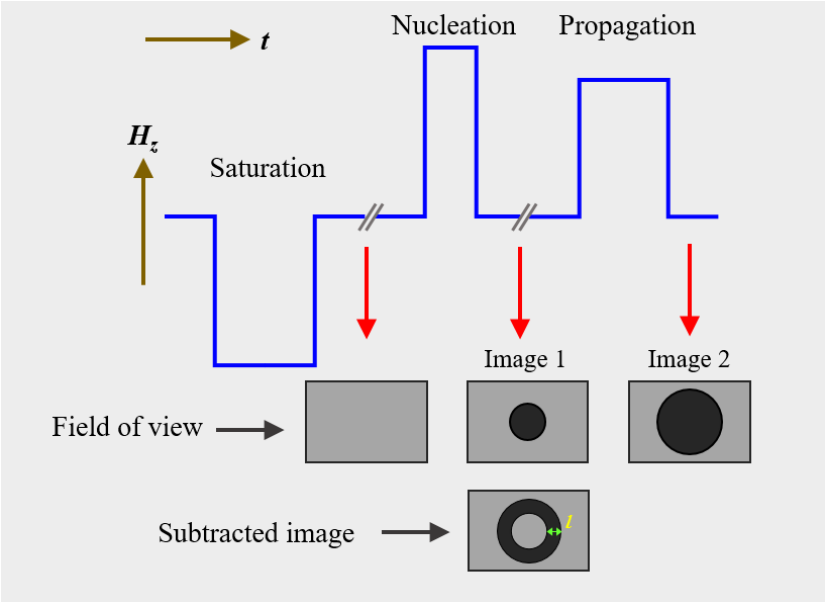

Figure 2.10: A schematic representation of DW velocity measurement protocol.

For the thesis work, we have used home-made coils to study the DW dynamics. For Pt/CoFeB sample, we have used a coil (diameter ~ 1 mm) to generate the pulsed magnetic field along the out-of-plane direction, with a pulse rise time of the order of 100 ns [138]. The measurement is performed at Laboratoire de Physique des Solides (LPS), Paris-Saclay University, France. For Pt/Co sample, a coil having ~100 number of turns and ~1 ms rise time is used to perform the measurements. A sourcemeter Keithley 2461 is used to apply the pulsed current through the coil. To study the DW motion, first, the sample is saturated by applying a constant magnetic field. Then, a reversed domain is nucleated and the image is recorded which is called image 1 (see figure 2.10). Next, another pulsed magnetic field (same polarity as nucleation field) with pulse-width, *t*, is applied for further DW motion and a domain image is recorded which is called image 2. Then, image 2 is subtracted from image 1 (see figure 2.10) to determine the resultant distance, *l*, travelled by the domain wall in the given field duration, *t*. Hence, the DW velocity is written as $v = \frac{l}{t}$ sample. We have varied both the amplitude and duration of a pulsed magnetic field during the measurements.

ii. Asymmetric DW motion measurements:

The interfacial Dzyaloshinskii-Moriya interaction (iDMI), arises from the heavy metal (HM)/ferromagnet (FM) interface and plays a pivotal role in DW statics and dynamics [139]. The iDMI combined with exchange interaction, Zeeman energy and anisotropy energy can stabilize chiral structures in a thin film. Therefore, quantification of the iDMI constant is very crucial for a thin film. Here, we have performed the asymmetric bubble domain expansion method to quantify the iDMI of PMA thin films. The iDMI field ($\boldsymbol{H_{DMI}}$) acts radially inward or outward direction in a bubble domain and preserves the rotational symmetry w.r.t *z*-axis. The symmetry of $\boldsymbol{H_{DMI}}$ can be broken by applying an in-plane bias field ($\boldsymbol{H_x}$) and left and right-side DWs propagate asymmetrically. Depending upon the direction of $\boldsymbol{H_{DMI}}$ and $\boldsymbol{H_x}$, the DWs

experience a resulting additive ($\boldsymbol{H_{DMI}} + \boldsymbol{H_x}$,) or subtractive ($\boldsymbol{H_{DMI}} - \boldsymbol{H_x}$,) force which causes the asymmetric motion. If $\boldsymbol{H_{DMI}}$ and $\boldsymbol{H_x}$ act oppositely, then for a particular value $\boldsymbol{H_x}$, the total resulting force cancels out i.e. $\boldsymbol{H_x} = \boldsymbol{H_{DMI}}$, and DW motion becomes minimum. In this case, the iDMI constant (D_{eff}) can be extracted by using the following equation [140–143],

$$D_{eff} = \mu_0 H_{DMI} M_s \delta \tag{2.16}$$

where, δ and M_s is the DW width and saturation magnetization of the sample, respectively. If A = exchange constant, K_{eff} = effective anisotropy constant then $\delta = \sqrt{\frac{A}{K_{eff}}}$.

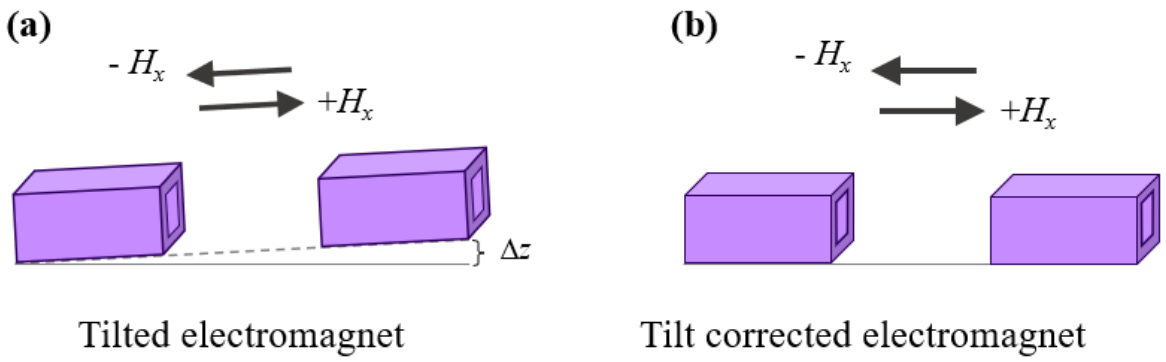

Figure 2.11: (a) and (b) Schematic of a tilted and tilt-corrected in-plane electromagnets, respectively. The tilt of the electromagnet is corrected via a rotating screw of the stage on which the magnet is placed.

We have assembled a set-up to measure the D_{eff} via Kerr microscopy. An electromagnet is used to apply the in-plane field ($\boldsymbol{H_x}$). The measurement procedure is very similar to DW velocity measurements. Here, first, the sample is saturated by applying $\boldsymbol{H_z}$ and then a domain is nucleated via a pulsed $\boldsymbol{H_z}$ in the opposite direction. Further, a simultaneous constant $\boldsymbol{H_x}$ and pulsed $\boldsymbol{H_z}$ are applied for the asymmetric DW motion. The $\boldsymbol{H_z}$ and $\boldsymbol{H_x}$ have to be perpendicular

to each other. A small tilt in $\boldsymbol{H_x}$ introduces an out-of-plane field which may cause an error in estimating the left (v_L) and right (v_L) side DW velocity under the application of a pulsed $\boldsymbol{H_z}$

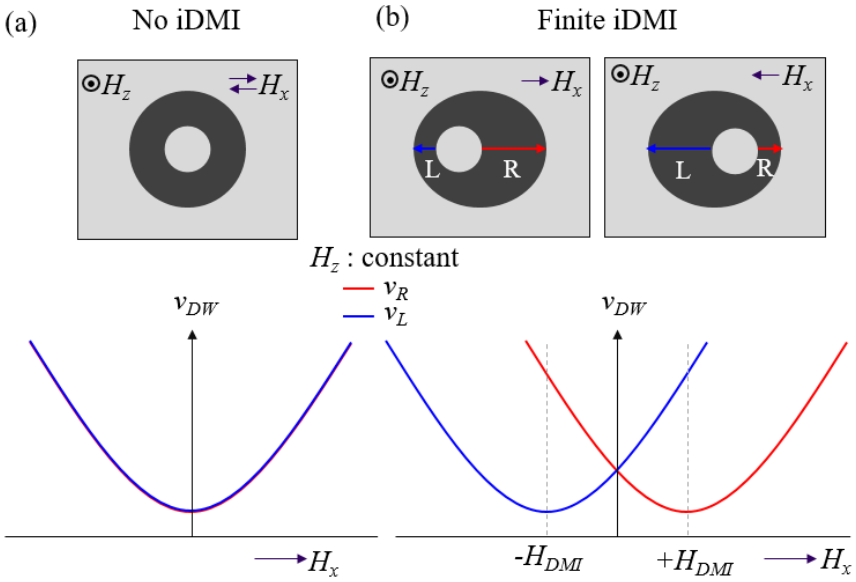

Figure 2.12: (a) Schematic of symmetric DW propagation and corresponding DW velocity as a function of H_x for no iDMI case. (b) Schematic of asymmetric DW propagation and corresponding DW velocity as a function of H_x for sizeable iDMI case. Here, the velocity of left (v_L) and right (v_R) side DW shifted oppositely w.r.t $H_x = 0$.

field (see figure 2.11 (a)). Therefore, the in-plane magnet is placed on a stage which can be moved up-down direction via a rotating screw. To correct the tilt angle, first, the measurements are performed for both $+\boldsymbol{H_x}$ and $-\boldsymbol{H_x}$ fields and measure the v_L or v_R. If tilt is present in the in-plane field, the v_L or v_R will be different for a particular $+\boldsymbol{H_x}$ and $-\boldsymbol{H_x}$ field. Thus, the stage is moved upward or downward direction and is repeated the measurements until the v_L or v_R become equal for a particular $+\boldsymbol{H_x}$ and $-\boldsymbol{H_x}$ field. Once the tilt angle is corrected, the measurement is performed for a constant pulsed $\boldsymbol{H_z}$ field with varying the $\boldsymbol{H_x}$ from +ve to –ve values (see figure 2.11 (b)). For each $\boldsymbol{H_x}$ value, the v_L and v_R are calculated. If there is no iDMI present in a system, the v_L and v_R should be superimposed and symmetric w.r.t in-plane field (see figure 2.12 (a)). However, the existence of iDMI in a system shifts the DW velocity

minima from zero to a finite IP field value which is comparable to the DMI field of the sample (see figure 2.12 (b)).

2.3.3. Magnetic force microscopy:

Magnetic force microscopy (MFM) is a very well-known and useful magnetic imaging technique for studying the magnetic domains or features in surface structure at micro to nanometer scales [144–146]. MFM is a scanning probe microscope. MFM is an advanced version of atomic force microscopy (AFM). MFM allows for measuring both topography as well as magnetic structures. Here, the information about the magnetic structures is achieved via the interaction between the stray field of the sample and a tip. Here, a magnetic tip (basically a sharp AFM tip coated with magnetic materials) attached with a flexible cantilever is scanned on the sample surface (shown in figure 2.13 (a)) and the interactions between the tip and the sample are detected. There are various types of interaction present depending upon the distance (Δz) between the tip and sample surface such as quantum mechanical force (Δz<1 nm), Van der Walls force (Δz~1 nm), and electric and magnetic force (Δz~0.05-1 μm). Therefore, the MFM scan is performed at a fixed lift height so that only stray field interaction between tip and sample plays a major role. The variations in the magnetic interaction between the magnetic tip and sample surface can be measured by a laser spot reflected from the top surface of the cantilever and by a photodetector. The photodetector detects the cantilever motion and measures the corresponding force gradient that arises due to the magnetostatic interactions. Also, the interaction changes the resonant frequency of the cantilever. Usually, the shift in resonant frequency (Δf) is found to be over a range of 1-50 Hz for a cantilever with resonant frequency ~100 kHz. The Δf is proportional to the force gradient that can be detected via the following methods i.e. amplitude modulation, phase modulation, and frequency modulation. In amplitude modulation, the amplitude of the cantilever's oscillation is recorded. In phase

modulation, the phase of oscillations is probed. In frequency modulation, the shift in resonant frequency (Δf) is directly detected. However, phase modulations are widely used due to their better signal-to-noise ratio, ease of use, and reduced artifacts effect. During the MFM scanning, the magnetic transitions emerged as a dark or a bright area corresponding to the attractive or repulsive force (see figure 2.13 (b)). The cantilever becomes softer due to the attractive force with a negative force gradient. Hence the resonant frequency of the cantilever gets reduced and a dark magnetic signal is obtained. However, for the bright magnetic signal, the resonant frequency gets enhanced as the cantilever becomes 'harder' due to repulsive force.

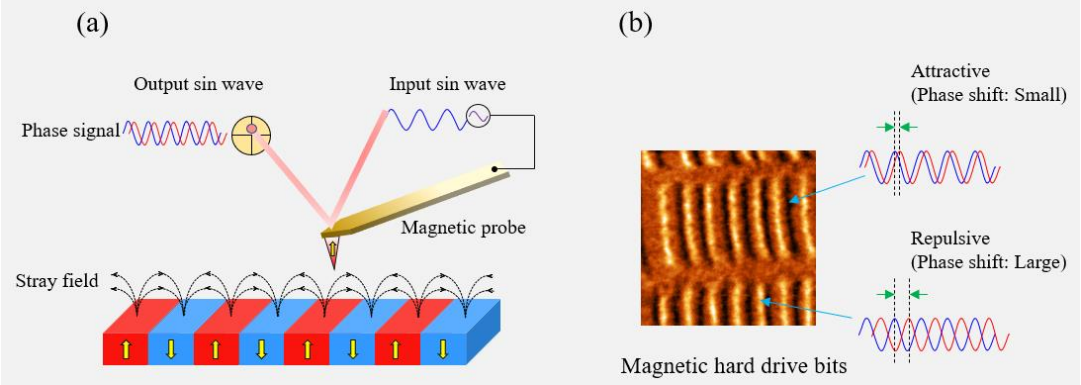

Figure 2.13: (a) Illustration of a basic principle of MFM. (b) Image of a magnetic hard drive bits measured via MFM. The dark and bright spot represents the repulsive and attractive force between stray fields of the magnetic tip and sample, respectively.

In the thesis work, a low temperature MFM manufactured by Attocube is used to perform the scanning for Pt/Co thin films (see chapter 5 and 7) at NISER. The temperature and magnetic field are varied in the range of 2 - 300K and ±9T, respectively, in the system. We have performed the measurements at room temperature using a commercial MFM tip manufactured by Nanosensor (SSS-MFMR). The MFM measurement for Pt/CoFeB samples (see chapter 6) are performed at Laboratoire de Physique des Solides (LPS), Paris-Saclay University, France using homemade MFM tips.

2.3.4. Brillouin Light Scattering:

Light-based scattering experiments play a pivotal role in studying various physical phenomena in solids, gases, and liquids. In the Brillouin light scattering technique, the scattered light contains information regarding the physical properties of a sample. BLS is a very sensitive and non-destructive technique to quantify the iDMI that arises at the HM/FM interface [147–150]. Here, the incident light (photon) interacts both elastically and inelastically with various quasi-particles (i.e., magnon, phonon, polariton, plasmon, etc.) present in the sample. In elastic scattering, the energy or frequency of scattered photons remains unchanged whereas in inelastic scattering it gets changed after the interaction with quasi-particles. For iDMI quantification, inelastic scattering between photon and magnon is considered in BLS (measurement geometry shown in figure 2.14 (a)). Due to the inelastic scattering, a finite frequency shift is observed in the BLS spectra (see the schematic in figure 2.14 (b)) and from the conservation of energy and momentum, the following expression can be written:

$$\hbar\omega_s = \hbar\omega_i \pm \hbar\omega \tag{2.17}$$

$$\hbar k_s = \hbar k_i \pm \hbar k \tag{2.18}$$

where +(-) sign represents the anti-stokes (stokes) frequency or wave vector shift and ω_i, k_i, ω_s, k_s are the frequency and wave vector of incident and scattered photons, respectively. Stokes (S) and Anti-stokes (AS) peaks arise due to the creation and annihilation of the magnons, respectively, in the BLS spectra (see figure 2.15). It should be noted that the energy of magnon ($\approx 10^{-4}$ eV) is very low in comparison to incident photon (≈ few eV). As a consequence, the magnitude of the wave vector of scatter and incident photon is very close to each other. Here, the 180◦ backscattered photons (arises due to inelastic scattering) are sent through a tandem Fabry-Perot (FP) interferometer to achieve a high spectral resolution and to extract the

information about the spin wave. Therefore, it is considered that k_i and k_s are collinear ($k_i = -k_s$). Hence, according to the conservation of the momentum, the modulus of the spin wave vector can be written as [147–149],

$$|k| = |k_i \sin\theta - k_s \sin\theta| = 2|k_i \sin\theta| = 2\left(\frac{2\pi}{\lambda}\right)\sin\theta \qquad (2.19)$$

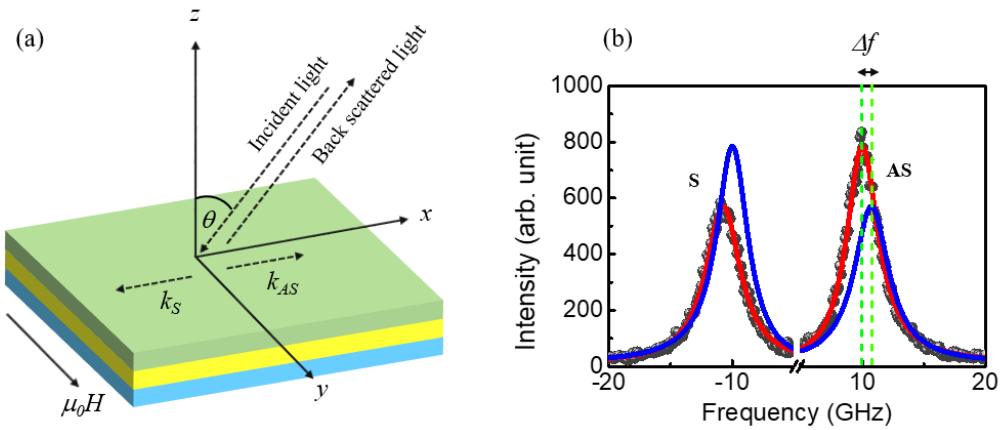

Figure 2.14: (a) Schematic representation of BLS measurement geometry. (b) Image of a typical BLS spectrum. The finite frequency shift between the S and AS lines indicates the presence of iDMI in a sample.

Now the sample is mounted on a rotatable stage which allows for a change of the incident angle (θ). By changing the incident angle, θ, the spin wave vector can be varied as per equation 2.19. During measurements, a constant magnetic is applied perpendicular to the spin wave vector which corresponds to Damon-Eshbach (D-E) mode (see figure 2.14 (a)). A finite frequency shift between S and AS lines indicates that the system possesses a sizeable iDMI.

In the thesis work, we have used this technique to quantify the iDMI for Pt/CoFeB/MgO thin films which are performed at Laboratoire de Physique des Solides (LPS), Paris-Saclay University, France. To apply the magnetic field, a permanent magnet is used in the experiment (maximum magnetic field: ±520 mT). The incident angles are varied over a range of 10°- 60°.

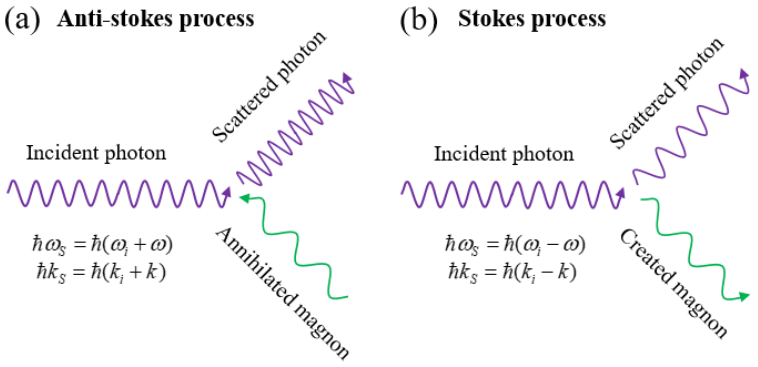

Figure 2.15: (a) and (b) Illustration of anti-stokes (AS) and stokes (S) process due to the inelastic scattering between photon and magnon, respectively. Magnon is created and annihilated in the stokes and anti-stokes process, respectively.

2.4 Electronic transport measurements:

Electronic and magnetic transport measurements are very useful to understand the electric properties of the sample such as conductivity, resistivity, charge carrier concentration, etc. While the electric properties of the sample are measured in the presence of the magnetic field known as magnetic transport measurements. A physical properties measurement system (PPMS) (shown in figure 2.16 (a)) is used to perform the electric measurements manufactured by Quantum Design, UK [151]. The longitudinal (ρ_{xx}) and transverse resistivity (ρ_{xy}) are measured via AC transport (ACT) measurements. An AC current is applied uniformly through the sample via two current probes. The current probes are made on the two opposite sides of the sample surface (around the perimeter). The voltage drop is measured in the four-probe geometry. A schematic of the two different measurements geometry with contact connections is shown in figure 2.16 (b)-(c). Figure 2.16 (b) shows the schematic of longitudinal resistivity measurement. Here, current (I_x) is applied via two outer connections (1 and 4), and the corresponding longitudinal voltage drop ($V_{xx} = V_2 - V_3$) is measured via two inner connections (2 and 3). The longitudinal resistivity is calculated using $\rho_{xx} = \frac{V_{xx}}{I_x} \times \frac{w \cdot t}{L}$, where *w, t,* and *L*

are width of the sample, the thickness of the thin film, and the distance between two electrodes, respectively [152]. Figure 2.16 (c) shows the schematic of transverse resistivity measurement [154,155]. Here, the voltage connections (2 and 3) should be opposite to each

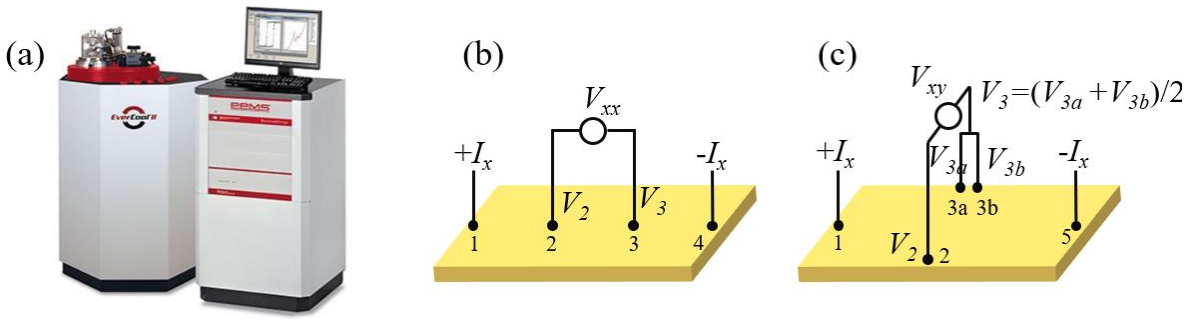

Figure 2.16: (a) Image of PPMS available at NISER. (b) and (c) Longitudinal and transverse transport measurements geometry. Four probe connections are utilized in longitudinal measurements, while five probe connections are used in transverse measurements.

other around the perimeter and must be perpendicular to the current (I_x) flow direction to detect the pure Hall signal. However, achieving such precise alignment of voltage probes is very difficult and the misalignment of the probes can add a magnetoresistance signal in Hall resistivity. Therefore, a five-probe approach with an additional voltage probe is used to overcome the problem [153]. As shown in figure 2.16 (c), instead of a single probe, two different probes 3a and 3b are used to measure the V_3 [156]. Therefore, the measured voltage at that end should be the average of the two voltages i.e. $V_3 = \frac{V_{3a}+V_{3b}}{2}$. In this way, the excess voltage gets neutralized before the measurements at zero magnetic field using a potentiometer between the two probes. This method significantly reduces the magnetoresistance signal in the Hall measurements. If V_{xy} (= $V_2 - V_3$) is the voltage drop along the transverse direction due to the applied current I_x, then the transverse resistivity can be written as $\rho_{xy} = \frac{V_{xy}}{I_x} \cdot t$. Usually,

the Hall resistivity (transverse resistivity) of a sample is measured by the four-probe geometry in the van der Pauw method [154,155].

In PPMS, the transport measurements can be done in both DC and AC modes. However, in this thesis work AC mode (ACT option) is used to perform the measurements due to a better signal filtering process. The AC bias with a frequency between 1 Hz to 1 kHz is applied during the measurement to enhance the accuracy of measured data. The DC offset, noise, and instrumental drift can be significantly reduced via using the ACT option.

The PPMS consists of a cryostat which helps to vary the temperature in the range of 1.8 -350 K. The superconducting magnets are used here to apply the magnetic field up to ±9 T. In the thesis work, the measurements are performed by applying an AC current of 500 μA with 17 Hz AC frequency. The contacts between the sample and sample holder are made via a wire bonder.

Chapter 3

Excess velocity of domain walls in the vicinity of the depinning field in a Pt/CoFeB/MgO film:

Domain wall (DW) dynamics in perpendicular magnetic anisotropic (PMA) systems have potential applications in a wide scale of magnetic devices such as DW-based racetrack memory, logic devices, and spin memristors for mimicking synapse in an artificial neural network [10,12,13,127]. The DWs in magnetic materials are considered as elastic objects in a weekly disordered medium [59,156,157]. The statics and dynamics of an elastic object in a disordered medium have a direct link with the physics of fluid dynamics, vortex dynamics in superconductivity, etc. [55,156,158]. Different phases of DW dynamics can be observed for an elastic DW associated with some amount of disorder [59,156,159,160]. Initially, it was believed that the DW dynamics should follow the linear behaviour as a function of externally applied force [161,162]. However, later it is observed that even a weak random pinning potential leads to a non-linearity in DW dynamics [42,56]. Pinning may be modelled by fluctuations of the anisotropy field which resist the DW motion at a smaller applied field/current [163,164] resulting in enhanced DW roughness and stochasticity [43]. There are mainly three different regions in DW dynamics viz. creep, depinning and flow regimes. However, near the depinning field (H_d), the DW dynamics sometimes do not follow the universal creep law [60,165]. The DW velocity (near H_d) may be found to be higher than the expected creep law. Previously, this kind of behaviour in DW dynamics has been observed only in Pt/Co/Pt and [Ni/Co] multilayer thin films [60,165]. This, unusual behaviour requires

further study to understand the physics of DW motion near the depinning field H_d. In this context, we have explored the DW dynamics in Pt/CoFeB/MgO multilayer thin film. Near H_d, the excess velocity is observed in the film which shows a good agreement with the theoretical model (modified creep law) as proposed by Caballero et al. [60]. In the modified creep law, a dimensionless and material-dependent parameter *p* has been introduced to explain the enhanced velocity. We have discussed the physical meaning of parameter *p* and defined a boundary condition for it. As this system is asymmetric, further, we have quantified the iDMI constant via the Brillouin light scattering spectroscopy (BLS) technique [166–168].

3.1 Sample details: The sample Ta (5 nm)/Pt (6 nm)/$Co_{40}Fe_{40}B_{20}$ (1.2 nm)/MgO (2nm)/ Ta (3 nm) is prepared in a high vacuum (base pressure was better than 8×10^{-8} mbar) chamber manufactured by Mantis Pvt. Ltd. A Si (100) substrate with thermally oxidized SiO_2 of 100 nm thickness is used to deposit the thin film. Ta, Pt and CoFeB layers have been deposited via DC magnetron sputtering and MgO layer has been deposited via e-beam evaporation in the deposition chamber. The substrate table has been rotated at 10 rpm to achieve uniformity for all layers. Post deposition, the sample has been annealed at 600° C for 1 h in the absence of magnetic field to improve the crystallinity and to induce the PMA. During annealing, the system pressure was better than 1×10^{-7} mbar. Here, Ta seed (bottom) layer is used for better growth of Pt. The top Ta layer prevents the ultra-thin film from oxidation. It has been reported that MgO is very much hygroscopic in nature [169,170] Therefore, without any capping layer, MgO layer will degrade which may lead to oxidation of the bottom CoFeB layer. Thus, a Ta capping layer is very much essential to maintain the quality of the sample for a long time.

3.2 Magnetic Characterization:

3.2.1 Static magnetic properties: The hysteresis loop of the sample is measured using polar magneto-optic Kerr effect (p-MOKE) based microscopy, as shown in figure 3.1 (a). From the

hysteresis loop, it is found that, $\frac{M_R}{M_S} = 1$ (where, M_R is the remanant magnetization and M_S is the saturation magnetization), which confirms that the easy axis aligns along the out-of-plane direction of the sample. Further, the saturation magnetization (M_S) of the sample is calculated from the hysteresis loops measured using SQUID magnetometry along the out-of-plane direction of the sample, as shown in figure 3.1 (b). Here, the value of M_S is found to be ~1.1 × 10^6 A/m.

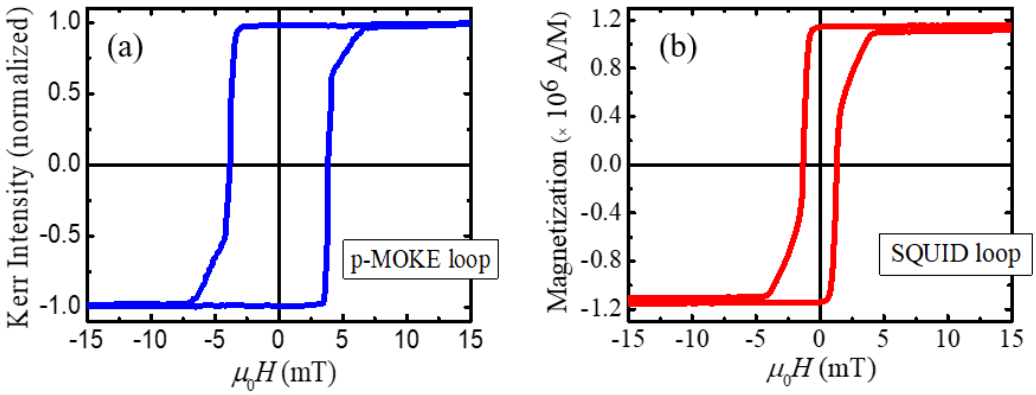

Figure 3.1 Hysteresis loops measured along the out-of-plane direction of the sample using (a) p-MOKE microscope and (b) SQUID magnetometer.

3.2.1 Dynamic magnetic properties: For magnetic thin films, the velocity vs. field curve can be divided into different regimes, as discussed earlier in Chapter 1. In the creep regime, the DW dynamics obey Arrhenius law, $v \sim \exp(-\Delta E/k_B T)$ where, ΔE is the effective pinning potential and $k_B T$ is the thermal energy. For small applied field $H << H_d$, the pinning potential is represented as

$$\Delta E\ (H \to 0) = k_B T_d \left(\frac{H}{H_d}\right)^{-\mu} \tag{3.1}$$

where, T_d is the depinning temperature and μ the universal creep exponent and its value is ¼ for ferromagnetic thin films [56,63]. However, for large applied field values (near to H_d),

equation 3.1 is not applicable and it needs modifications. In particular, when the applied field becomes equal to the depinning field the pinning barrier vanishes. In this case [$0 < H \leq H_d(T)$], the modified pinning potential scales as [56],

$$\Delta E = k_B T_d \left[\left(\frac{H}{H_d}\right)^{-\mu} - 1\right] \tag{3.2}$$

Hence, the DW motion in the creep region is represented as,

$$v = v_0 e^{-\frac{T_d}{T}\left[\left(\frac{H}{H_d}\right)^{-\mu}-1\right]} \tag{3.3}$$

where, $v_0 = v_d\,(H_d, T)$ = velocity at depinning ($H = H_d$).

For this study, the pulsed magnetic field-induced DW dynamics is measured using p-MOKE microscopy at Laboratoire de Physique des Solides, Université Paris-Saclay, France. To generate the pulsed magnetic field along the out-of-plane direction we have used a home-made small coil of ~1 mm diameter, with a pulse rise time ~100 ns. During measurement, we have varied both the amplitude and width of the applied pulsed magnetic field. In this case, the pulse width is varied from 1 μs to 5 s. The measurement protocol is the same as explained earlier in Chapter 2 (section 2.3.2). Figure 3.2 (a) shows a subtracted domain image for this sample. Figure 3.2 (b) shows the DW velocity (v) vs. applied magnetic field (H) plot. Our investigation has been limited to magnetic fields up to 16 mT. Indeed, beyond, the large domain wall velocity implies that neighbouring domains merge and the displacement of the domain wall cannot be measured. The velocity is found to increase with the applied magnetic field and no inflection point is observed, a sign that the depinning regime could not be reached. Further, the logarithm of velocity ($\ln v$) vs. $(\mu_0 H)^{-1/4}$ has been plotted in figure 3.2 (c), to verify the DW dynamics lies in the creep regime. It shows a good agreement with the usual creep law at the lower applied field. However, at higher fields (near H_d), the DW velocity is found to be higher than the expected creep law. The enhancement in velocity cannot be fitted with the previously described

universal creep theory. This kind of enhanced velocity in DW dynamics has been observed earlier in Pt/Co/Pt thin film [165]. Recently, a theoretical model was proposed by Caballero et al. for a similar behaviour of the DW motion in [Ni/Co] thin film and this phenomenon was named as "excess velocity" [60].

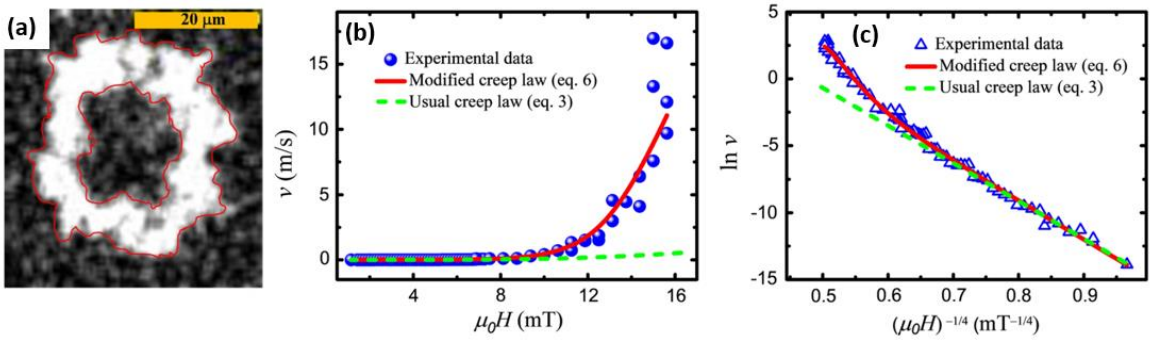

Figure 3.2 (a) Subtracted domain image (by subtracting a nucleated image from a propagated image). The close red loops represent the nucleated and propagated domains. (b) Domain wall velocity (v) vs. field ($\mu_0 H$), and **(c)** $ln\ v$ vs $(\mu_0 H)^{-1/4}$ plot. To fit the measured data (using equations 3 and 6), $\mu_0 H_d$ = 19 mT has been considered.

One can consider that the DW segment may jump to a new metastable configuration by crossing an optimal energy barrier as a result of applied field and thermal energy. Then, the DW segment in its new state acts as a thermal nucleus and further triggers to reach a subsequent metastable state, concluding the entire creep event. While DW motion approaches near the depinning field, the thermal nucleus has the ability to initiate deterministic relaxation events, which are comparable to depinning avalanches. This enhances the propagation length and hence, the DW velocity increases near H_d [60]. However, the particular condition in which the thermal nuclei near H_d trigger the deterministic relaxation events, is still an open question.

In this case, the velocity prefactor, v_0 gets modified (see figure 3.3), beyond a typical field H_r where relaxation events start [60]. In the low field range ($H < H_r$), v_0 remains the same as the

usual creep law (equation 3.3). For $H_r < H < H_\varepsilon$, the velocity prefactor is modified by the relaxation length scale and higher DW velocity arises with

$$v = v_0[1 + p(\delta h^{-\nu} - 1)^{\zeta+1}]e^{-\frac{T_d}{T}\left[\left(\frac{H}{H_d}\right)^{-\mu}-1\right]} \approx v_0 p\,\delta h^{-\nu(\zeta+1)} e^{-\frac{T_d}{T}[(\frac{H}{H_d})^{-\mu}-1]} \quad (3.4)$$

with p a dimensionless parameter, $\delta h = \left(\frac{H_d - H}{H_d}\right)$ the reduced field. Here, ν and ζ are the depinning length and roughness exponents, respectively, defined by the quenched Edwards-Wilkinson universality class ($\nu = \frac{1}{(2-\zeta)} = 1.33$) [171]. The approximation in equation 3.4 is valid for H close to H_d. The parameter p represents the ratio between an elemental and optimum domain wall jump surface ($p = \frac{L_c r_f}{L_0 u(x)}$) [60]. L_c is the Larkin length which represents the critical DW length below which the elastic energy required to deform the wall is larger than the energy gained from the deformation. Shorter than L_c, DWs are flat. L_0 is DW length corresponding to depinning avalanches. As a consequence, L_0 is always higher than L_c. Further, r_f and $u(x)$ are the correlation length of the pinning force and the displacement made by the DW during an avalanche, respectively. Again, r_f is necessarily smaller than $u(x)$. Therefore, the value of p should be smaller than 1. The relaxation length further saturates beyond H_ε, and δh becomes constant ($\delta h = \varepsilon$).

The velocity becomes

$$v = v_0[1 + p(\varepsilon^{-\nu} - 1)^{\zeta+1}]e^{-\frac{T_d}{T}\left[\left(\frac{H}{H_d}\right)^{-\mu}-1\right]} \approx v_0 p\,\varepsilon^{-\nu(\zeta+1)} e^{-\frac{T_d}{T}[(\frac{H}{H_d})^{-\mu}-1]} \quad (3.5)$$

Combining all the above three equations the modified creep law can be written as [60],

$$v = v_0\{1 + p[(\delta h^m + \varepsilon^m)^{-\nu/m} - 1]^{\zeta+1}\}\, e^{-\frac{T_d}{T}[(\frac{H}{H_d})^{-\mu}-1]} \quad (3.6)$$

with m as a cross-over parameter. In the model, $m = 4$ is considered as a large value of m does not affect the DW behaviour significantly [60]. It should be noted that the velocity prefactor represents the velocity exactly at H_d when the relaxation event saturates, as

$$v(H_d) = v_0[1 + p(\varepsilon^{-\nu} - 1)^{\zeta+1}] \tag{3.7}$$

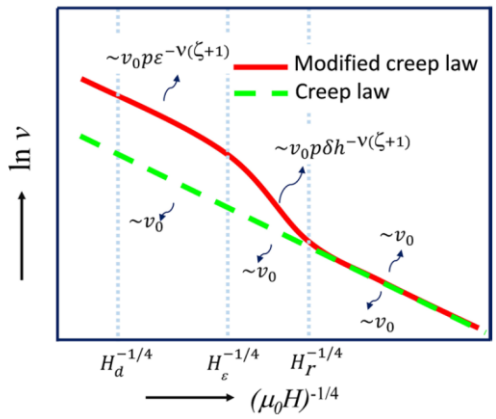

Figure 3.3 Three different field-dependent velocity regions are separated by the dotted vertical lines. The green dotted line and red line show the usual creep and modified creep law, respectively. The velocity prefactor is the same for all regions for the usual creep law but it varies for the modified creep law as shown in the figure [60].

As the excess velocity is observed in DW dynamics, *ln v* vs $(\mu_0 H)^{-1/4}$ plot has been fitted using equation 3.6 (see figure 3.2 (c)) and shows a good agreement with the modified creep law. Furthermore, we have extracted the values of *ln v* and $(\mu_0 H)^{-1/4}$ from both the fittings (usual and modified creep fit) of figure 3.2 (c). From the extracted values, *v* and $\mu_0 H$ have been calculated and plotted in figure 3.2 (b). In this case, also we have seen that *v* is showing good consistency with low $\mu_0 H$ values for both cases. It is important to emphasise that to obtain the three depinning parameters (i.e., H_d, T_d and v_T (= depinning velocity)), information from the depinning regime is also necessary in addition to the standard creep law. Since we have not reached the depinning transition, the value of $\mu_0 H_d$ is considered to be ≥ 16 mT. For the creep

fit, we have varied $\mu_0 H_d$ up to 25 mT to evaluate the depinning parameters using the boundary limit of p. Table 3.1 presents all the fitted parameters describing the excess velocity in DW dynamics. In figure 3.2, $\mu_0 H_d$ is considered as 19 mT and the logarithmic plots with creep fit for other H_d values have been shown in figure 3.4. As remarked in earlier studies [60], v_0 is found independent on H_d. The fitted value of T_d decreases and p increases with H_d. Previously, in ref. [60], the values of p greater than 1 have been used for the modified creep fittings which

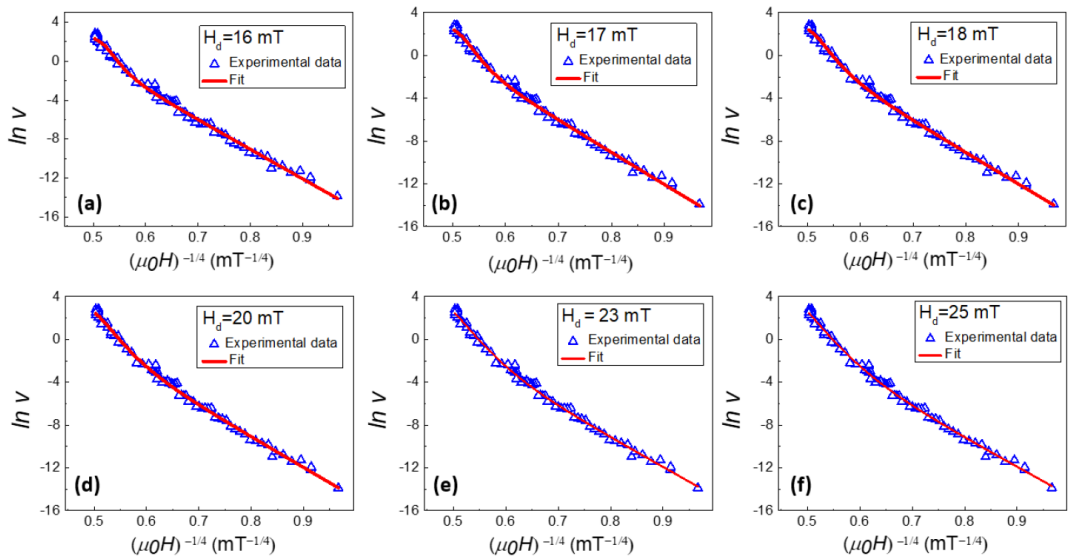

Figure 3.4 (a)-(f) *ln v* vs $(\mu_0 H)^{-1/4}$ plot considering $\mu_0 H_d$ between 16 to 25 mT. The red lines are the fit of the data using the modified creep law.

may lead to an inaccuracy in estimating the depinning parameters. However, we have demonstrated that p should be less than 1. It is observed that up to $\mu_0 H_d$ = 19 mT the value of p is lower or close to 1 (see Table 3.1) for the Pt/CoFeB/MgO thin film which sets a maximum value to the depinning field. Hence, it can be concluded that $\mu_0 H_d$ lies between 16 and 19 mT. In addition, the values of T_d and $v(H_d)$ vary between 4000 and 4500 K and 12 and 25 m/s, respectively.

3.2.2 iDMI quantification: In our sample **(**Pt/CoFeB/MgO) as the inversion symmetry is broken and the high spin-orbit coupling material Pt is adjacent to CoFeB, a finite iDMI value can be expected from the system. To determine, the iDMI constant (D) we have performed the BLS measurements. Here, a constant in-plane magnetic field (H_x) of 420 mT has been applied perpendicular to the incident plane of light and after photon-magnon interaction, the spin wave propagates along the sample surface (DE geometry). The spin waves propagating along the $+x$ ($-x$) direction has lower (higher) energy with clockwise (anti-clockwise) spatial chirality when viewing along the D [167]. The modulus of the spin wave vector is $k_{sw} = 4\pi \sin\theta/\lambda$, where θ is the incident angle and λ (=532) nm is the wavelength of incident laser light. Figure 3.5 (a) reveals the BLS spectra of the sample (at θ=45° and k_{sw}=16.7 μm^{-1}) which indicates the

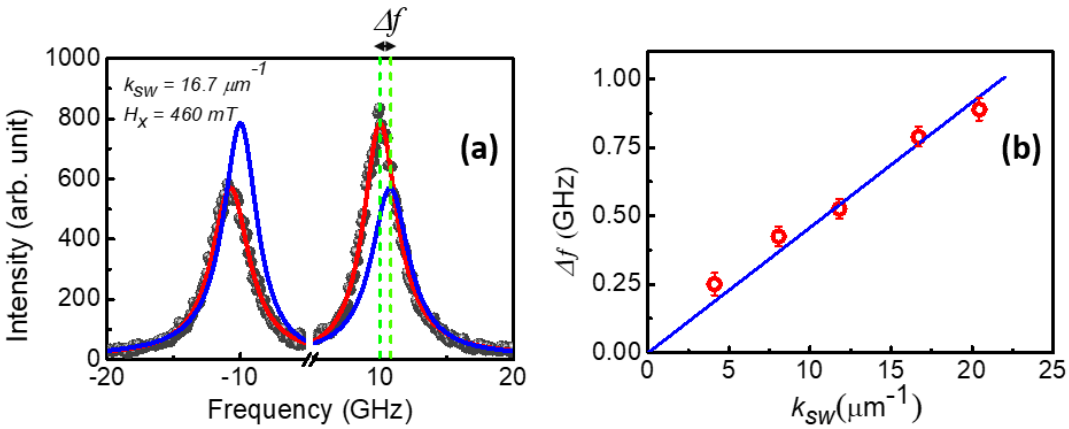

Fig. 3.5 (a) BLS spectra of the sample at k_{sw}= 16.7 μm^{-1} and Hx= 420 mT, (b) plot of frequency difference (Δf) vs spin wave vector (k_{sw}).

presence of asymmetry in intensities as well as in the frequency of anti-stokes (AS) and stokes (S) peaks. The asymmetry arises due to the features of surface propagating DE spin waves. The experimental data of Fig. 3.5 (a) (black dot) has been fitted using the Lorentzian function (the red continuous line is the fitted line) to deduce the frequency of S (f_S) and AS (f_{AS}) peaks very precisely. By reversing the direction of the in-plane applied field the frequency of S and AS

peaks can be interchanged [167,168]. Although the direction of the vector ***D*** will be the same always. Using this spin-wave property, the blue lines in figure 3.5 (a) have been obtained by reversing the frequency instead of reversing the field to get a better understanding. Further, we have varied the spin wave vector, k_{sw} to 4.10, 8.07, 11.81, 16.70 and 20.45 μm^{-1} by changing θ to 10°, 20°, 30°, 45° and 60°, respectively, at the same in-plane magnetic field and the frequency difference (Δf) has been evaluated for every k_{sw}. Δf as a function of k_{sw} has been plotted in figure 3.5 (b) and fitted with the following equation [166–168]:

$$\Delta f = f_S(-k) - f_{AS}(k) = \frac{2\gamma}{\pi M_S} D k_{sw} \quad (8)$$

where, $\gamma/(2\pi)$ = g × 13.996 GHz/T with g the Landé factor, D is the DMI constant. From the slope of the linear fit, we have obtained the value of D = ~0.39±0.03 mJ/m2.

H_d (mT)	m	v_0 (m/s)	T_d (K)	p	ε	v (H_d) (m/s)
16	4	1.05 ± 0.20	4558 ± 100	0.18 ± 0.06	0.23 ± 0.02	11.94 ± 0.20
17	4	1.14±0.20	4425±100	0.37±0.10	0.27 ± 0.02	14.89 ± 0.30
18	4	1.19± 0.30	4291±100	0.72±0.30	0.30 ± 0.02	20.13 ± 0.40
19	4	1.21± 0.30	4163± 110	1.26± 0.50	0.33 ± 0.03	24.65 ± 0.40
20	4	1.21 ± 0.40	4045 ± 120	2.06 ± 0.80	0.35 ± 0.02	31.62 ± 0.50
23	4	1.26 ± 0.50	3763 ± 150	5.93 ± 2.60	0.38 ± 0.03	66.59 ± 0.60
25	4	1.30 ± 0.60	3613 ± 160	9.89 ± 4.70	0.38 ± 0.03	113.72 ± 0.70

Table 3.1: Fitting parameters of Pt/CoFeB/MgO sample velocity-field data obtained using eq. (6).

In summary, we have studied the field-dependent DW dynamics in the creep region for an ultrathin Pt/CoFeB/MgO sample. Our observation of the excess velocity close to the depinning field is explained by a modified creep law. Furthermore, the physical importance of the

parameter p for the modified creep theory has been discussed. The modified creep law combined with the mentioned boundary condition of p helps us to predict the range of three material-dependent pinning parameters (i.e., depinning field, depinning velocity and depinning temperature) even if the depinning transition is not reached in DW motion. It has already been shown that the modified creep law holds for single-layer [165], and multilayer thin films of Co [60], and we find that it also holds for single-layer films of CoFeB. More work is needed to test the validity of this modified creep law to realize if it is universal to explain the excess velocity in ferromagnetic systems. We have also quantified the iDMI value which is present in the asymmetric Pt/CoFeB/MgO sample.

Chapter 4

Effect of Re insertion on domain wall dynamics and interfacial Dzyaloshinskii-Moriya interactions:

The Dzyaloshinskii-Moriya interaction (DMI) has been extensively studied due to its interesting fundamental physics and potential applications in upcoming storage technology. Interfacial Dzyaloshinskii-Moriya interaction (iDMI) arises at the interface between ferromagnet (FM) and nonmagnetic heavy metal (HM) having high spin-orbit coupling and lack of inversion symmetry [172]. The iDMI vector may change the sign depending on the different types of interfacial atoms and the stacking order of HM and FM which determine the preferred spin chirality, clockwise (CW) or anti-clockwise (ACW). The iDMI has a great impact on domain wall (DW) statics [40] as well as dynamics [78]. The existence of iDMI in a thin film decreases the DW energy and prefers the formation of a chiral Neel DW [40]. It has been reported that iDMI enhances the field and current-induced DW motion [78,88,173]. It can stabilize chiral spin texture i.e. chiral DWs [23,87], skyrmions [7,77,87], etc. depending upon the value of iDMI. An asymmetric thin film of HM_1/FM/HM_2 or HM/FM/Oxide is an ideal system for exhibiting the iDMI. In the previous chapter, we have observed that HM/FM/Oxide i.e. Pt/CoFeB/MgO system exhibits an iDMI value ~0.39 mJ/m^2 which mostly arises from the bottom Pt/CoFeB interface. However, by choosing a proper combination of HM_1 and HM_2, DM interaction can be enhanced significantly in a HM_1/FM/HM_2 system. Higher iDMI helps in stabilizing the smaller size of chiral textures which will be useful for practical application. In this context, various asymmetric stacks i.e. Pt/Co/Ir [174], Pt/Co/Ru [174], Pt/Co/W [175],

Pt/Co/Pd [176], etc., have been studied where the iDMI values are found in the range over 1 – 2.5 mJ/m^2. Recently, from first-principle calculations, it has been predicted that Pt/Co/Re system possesses a huge iDMI interaction (iDMI constant, D ~9.17 mJ/m^2) than any other thin film system like Pt/Co/ [177,178]. Further, the experiment proved that Pt and Re induce opposite chirality in DWs and the iDMI arising from Pt/Co and Co/Re added up [179]. Thus, it is very important to study the effect of such HM on DW dynamics and DM interaction while it is grown on the top of a FM.

In this context, we have prepared Pt/Co/Re(t_{Re})/Ta thin film having perpendicular magnetic anisotropy. We have studied the effect of Re insertion on magnetization reversal, effective anisotropy and DW dynamics. Further, iDMI value has been quantified from all the stacks via asymmetric DW motion and an iDMI value of ~ 0.7 mJ/m^2 has been calculated from the Co/Re interface.

4.1 Sample details: A series of samples with structure Ta (5 nm)/Pt (6 nm)/Co (1 nm)/Re (t_{Re})/Ta(4nm) are deposited by varying the Re thickness (t_{Re}) on Si/SiO2 (100 nm) substrate at room temperature, where t_{Re}= 0, 0.2, 0.5, 1.0 and 2.0 nm. The samples are named as S1-S5 for t_{Re}=0 – 2.0 nm, respectively. The Ta, Pt and Co layers are deposited via DC sputtering and Re layer is deposited via RF sputtering. The base pressure was ~ 6×10^{-8} mbar. The deposition rate of Pt, Ta, Co and Re was 0.3, 0.13, 0.1 and 0.1 Å/s, respectively. The substrate table was rotated at 10 rpm during the deposition to achieve uniformity in each layer.

4.2 Magnetic Characterization:

4.2.1 Magnetization reversal: The magnetisation reversal has been studied via polar-MOKE microscopy. The square hysteresis loops of all the samples indicate that the easy axis is vertical to the film plane. The coercive field (H_c) decreases with increasing the Re thickness which reflects a decrease in effective anisotropy. The H_c values are found to be ~13 mT, ~10.58 mT

and ~7.47 mT for S1, S2 and S3-S5, respectively. Beyond t_{Re}=0.5 nm, no significant change in H_c is observed in the samples. Thus, it can be concluded that in S2 (t_{Re}=0.2 nm), a dusting layer of Re is formed between the top Co and Ta layer which causes an intermediate H_c value. However, a continuous layer of Re is formed for $t_{Re} \geq 0.5$ nm and causes a saturation in the H_c for S3-S5.

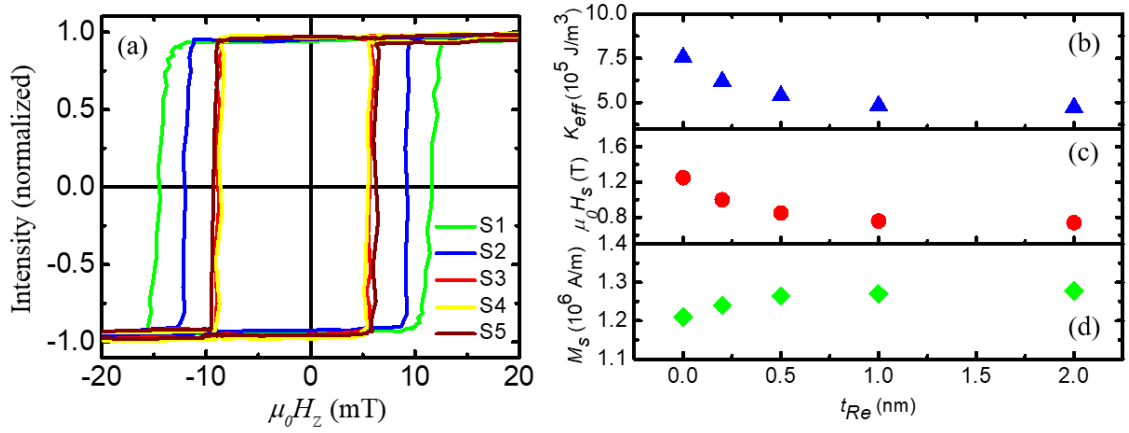

Figure 4.1: (a) hysteresis loops of S1-S5 measured via polar MOKE microscopy, (b-d) K_{eff}, H_S, and M_S are obtained from hysteresis loops measured by SQUID magnetometer.

4.2.2 Magnetic anisotropy: The effective anisotropy of all the samples is determined after performing the M-H measurement via SQUID. The effective anisotropy can be expressed as, $K_{eff} = (1/2)\mu_0 H_s M_s$, where H_s is the in-plane saturation field (i.e. the field required to saturate the magnetisation along in-plane direction) and M_s is the saturation magnetisation. The values of H_s, M_s, and K_{eff} are shown in table 4.1 and in figure 4.1 (b-d). The H_s decreases with increasing the Re thickness like H_c and consequently, K_{eff} also decreases. The decrease in K_{eff} with t_{Re} may be due to the reduction in interfacial anisotropy at the Co and Re interface.

4.2.3 Domain wall dynamics: The pulsed field-induced DW motion for all the samples is measured via Kerr microscopy in our laboratory (LNMM-NISER) using the measurement protocol as explained in chapter 2. The measurements are limited only to the creep regime.

Figure 4.2(a) shows the DW velocity (v) as a function of field (H_z) and the logarithm of the velocity (ln v) vs $H_z^{-1/4}$ is shown in figure 4.2(b). The experimental data are fitted with the following creep law [42,160]:

$$v = v_0 e^{-\frac{T_d}{T}\left[\left(\frac{H_z}{H_d}\right)^{-\mu}\right]} \tag{4.1}$$

and the logarithm of the velocity can be written as:

$$ln\, v = ln\, v_0 - \frac{T_d}{T}\left(\frac{H_z}{H_d}\right)^{-\mu} \tag{4.2}$$

with universal creep exponent μ =1/4. As the data fitted well with equations 4.1 and 4.2, it is confirmed that DW motion stays in the creep regime. It is observed that the v increases with increasing the Re thickness and beyond t_{Re}= 1.0 nm (for S4 and S5), no significant change in v is observed. The possible reason for the enhancement in the v could be the lowering in the depinning field (H_d), reduction in k_{eff} and enhancement in iDMI. The H_d is strongly related to the defects or disorder or local variation in the anisotropy of samples. The ratio of $\frac{T_d}{T}(H_d)^{\frac{1}{4}}$ is extracted from the creep fittings which is related to the pinning of the sample and are shown in table 4.1. The value of $\frac{T_d}{T}(H_d)^{\frac{1}{4}}$ is found to be 11.01 Tesla$^{0.25}$ for S1 and is reduced to ~8.2 Tesla$^{0.25}$ for samples S4 and S5 which signify that the pinning potential of the samples decreases with t_{Re}. Further, as shown earlier, the reduction in PMA energy with t_{Re} helps in lowering the DW formation energy (σ_{DW}), which supports achieving higher DW velocity. Additionally, we have also found that the iDMI constant increases from 1.10 to 1.78 mJ/m^2 after the insertion of Re which also causes faster DW dynamics. A detailed analysis of iDMI quantification is explained in the next section.

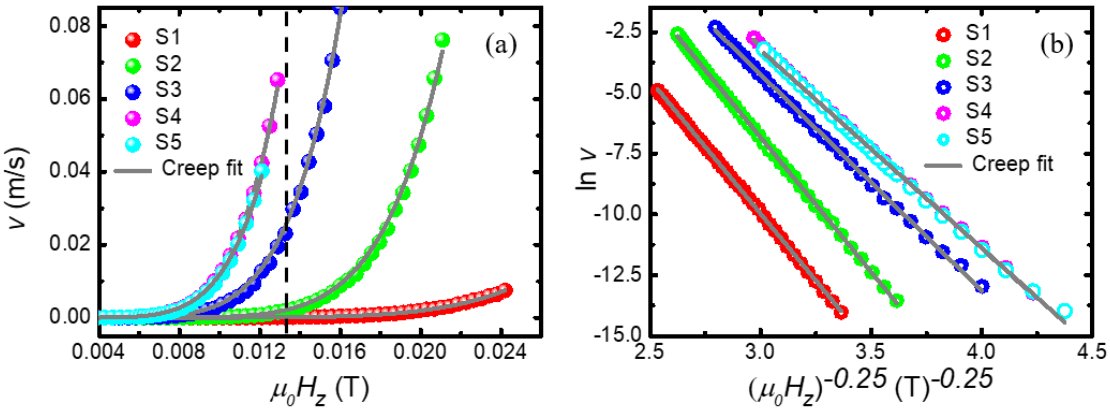

Figure 4.2: (a) DW velocity (v) vs. field ($\mu_0 H_z$) and (b) $ln\, v$ vs. $(\mu_0 H_z)^{-\frac{1}{4}}$ plots for samples S1-S5. The black dotted line is used in figure (a) to visualise the enhancement in v.

4.2.4 interfacial Dzyaloshinskii-Moriya Interaction (iDMI):

iDMI originates at HM/FM interface having broken inversion asymmetry. It is already proven that Pt/Co interface gives a sizeable iDMI constant of ~1-2 mJ/m^2. However, recently it has been predicted that a huge iDMI could be expected from Re/Co interface too. Therefore, here, we have quantified the iDMI constant in the samples via the asymmetric bubble expansion method as proposed by Je et al. [66]. The DMI field provides a radial symmetry in a bubble domain. Now, after applying an in-plane field (H_x), the radial symmetry got broken and the domain propagates asymmetrically. In this case, one side of the DW experiences an additive force (H_x+H_d) whereas a subtractive force (H_x-H_d) is exerted on the opposite side of DW. Thus, at H_x=H_d, the force acting on one side of DW is nearly zero and the DW velocity becomes minimal. In this context, the modified creep law can be written as [66],

$$v(H_x) = v_0 e^{-\zeta H_Z^{-\mu}} \tag{4.3}$$

where μ=1/4 and $\zeta = \zeta_0 \left(\frac{\sigma(H_x)}{\sigma_0}\right)^{-1/4} = \frac{T_d}{T} H_d^{1/4} \left(\frac{\sigma(H_x)}{\sigma_0}\right)^{-1/4}$. ζ_0 related to the pinning potential of the sample without applying H_x. The $\sigma(H_x)$ can be written as:

$$\sigma(H_x)|_{B-N} = \sigma_0 - \frac{\delta(\pi\mu_0 M_S)^2}{8K_D}(H_x + H_D)^2 \text{ for } |H_x + H_D| < \frac{4K_D}{\pi\mu_0 M_S}$$

$$\sigma(H_x)|_N = \sigma_0 + 2K_D\delta - \pi\delta\mu_0 M_S|H_x + H_D|, \text{ otherwise} \quad (4.4)$$

where $\sigma_0 = 2\pi\sqrt{Ak_{eff}}$ is the Bloch wall energy, $\delta = \sqrt{A/k_{eff}}$ is the DW width and $K_D = t\ ln(2)\frac{\mu_0 M_S^2}{2\pi\delta}$ is the DW anisotropy energy density.

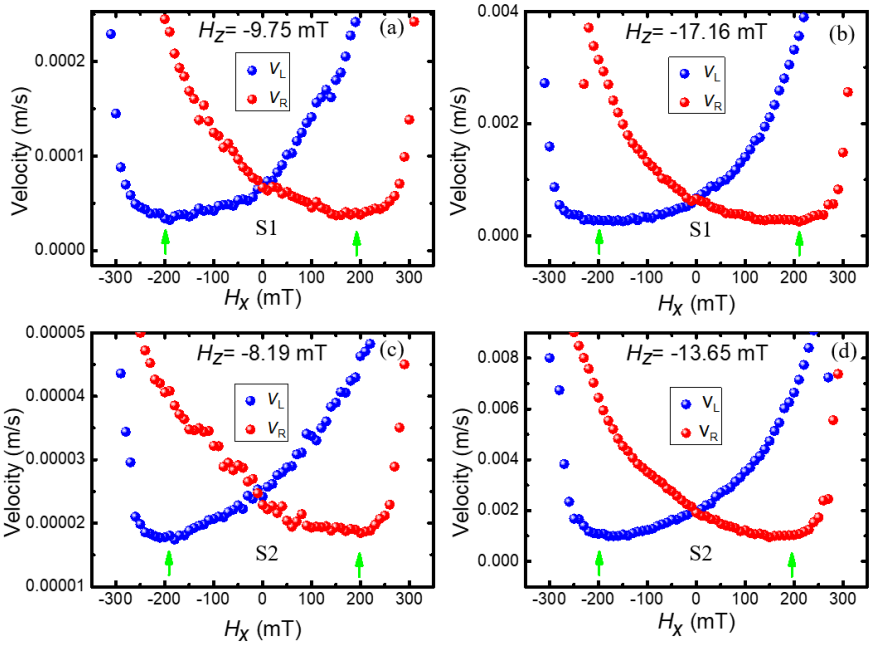

Figure 4.3: v_L and v_R as a function of H_x for S1 at (a) H_z=-9.75 mT and (b) H_z=-17.16 mT; for S2 at (c) H_z=-8.19 mT and (d) H_z=-13.65 mT.

After, determining the H_d, the effective iDMI constant can be expressed as [66,67],

$$D_{eff} = \mu_0 H_d M_S \delta \quad (4.5)$$

where M_S is the saturation magnetization and $\delta = \sqrt{\frac{A}{k_{eff}}}$ is the DW width.

Thus, we have measured the DW velocity (v) as a function of H_x at a constant out-of-plane field (H_z) using the procedure described in chapter 2. The left (v_L) and right side DW velocity (v_R) for the samples S1 and S2 are shown in figure 4.3. The minimum velocity is observed at H_x=

H_d= ~200 mT for S1 and S2. The corresponding iDMI value (D_{eff}) is quantified using equation 4.5 and is found to be 1.10 ± 0.09 and 1.25 ± 0.11 mJ/m^2 for S1 and S2, respectively. For this evaluation, we have considered A=16 pJ/m [67] and other parameters are taken from the experiment. Further, figure 4.4 shows the velocity vs H_x plot for samples S3, S4 and S5 and the H_d is observed to be ~240 mT.

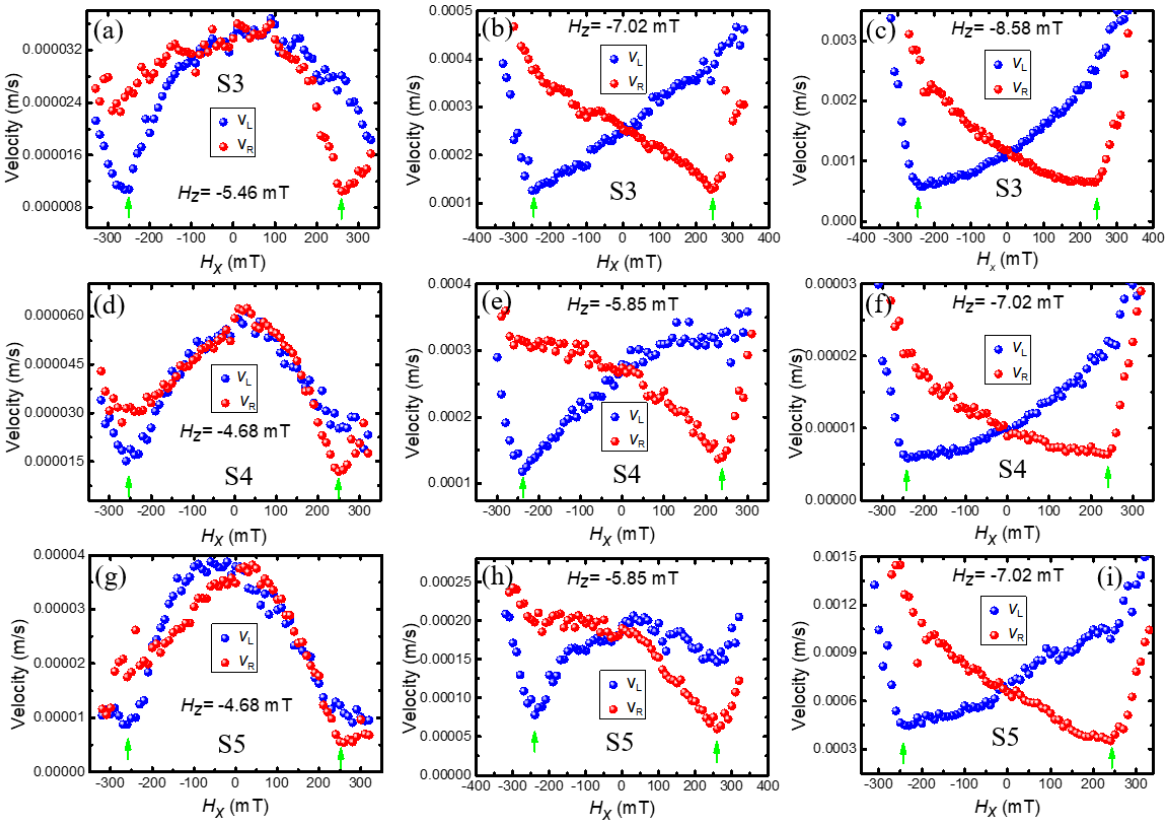

Figure 4.4: v_L and v_R as a function of H_x for sample S3 at (a) H_z=-5.46 mT, (b) H_z= -7.02 mT and (c) H_z=-8.58 mT; for sample S4 at (d) H_z=-4.68 mT, (e) H_z =-5.85 mT and (f) H_z =-7.02 mT; for S5 at (g) H_z=-4.68 mT, (h) H_z=-5.85 mT and (i) H_z=-7.02 mT.

The D_{eff} of 1.65 ± 0.16, 1.75 ± 0.16, 1.78 ± 0.17 mJ/m^2 is quantified for samples S3, S4 and S5, respectively. The D_{eff} as a function of t_{Re} is shown in figure 4.5 and table 4.1. The D_{eff} increases with increasing the t_{Re} up to 1 nm which is also reflected in DW dynamics (see figure 4.2). Beyond t_{Re}= 1 nm, the D_{eff} got saturated. Now, the Co/Ta interface gives a very negligible

iDMI [180], thus the D_{eff} arises in S1 mostly from Pt/Co interface. Thus, comparing the D_{eff} values of S1 and S5, one can quantify that a maximum ~0.7 mJ/m^2 iDMI value comes from the Co/Re interface. As the D_{eff} enhances after the insertion of Re, it could be concluded that Pt/Co and Co/Re give an additive iDMI.

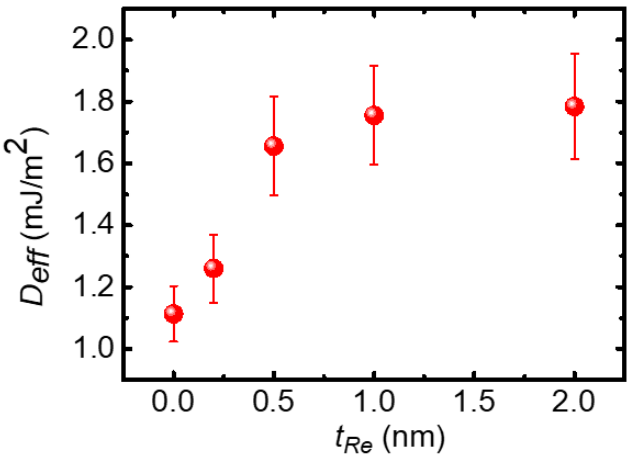

Figure 4.5: Effective Dzyaloshinskii-Moriya constant (D_{eff}) as a function of Re thickness (t_{Re}).

Further, we have also varied the H_z to study the behaviour of v_L and v_R as a function of H_x. For S1, H_z = -9.75 mT and -17.16 mT (see figure 4.3(a-b)) whereas for S2, H_z = -8.19 mT and -13.65 mT (see figure 4.3(c-d)) are considered. It has been observed that the behaviour of v_L and v_R are very similar at different H_z for S1 and S2 as observed earlier [181]. However, for S3-S5, we have considered three different H_z values (see figure 4.4 (a-i)), as the behaviour of v_L and v_R got significantly changed with H_z, unlike S1 and S2 which is not observed earlier in DW dynamics. Also, via a lateral shift of the minima of v_L on the minima of v_R (or vice versa), the two plot cannot be superimposed which signify that the H_x dependence DW dynamics cannot be explained by the equation 4.4, proposed by Je et al. [66]. In 2016, E. Jue et al. first observed some unusual behaviour of v_L and v_R in the presence of both H_z and H_x [182]. The experimental data cannot be fitted by the equation given by S. G. Je et al [66]. In this case, they performed

some numerical simulations with varying the damping constant and confirmed that the chiral nature of damping is responsible for this kind of DW dynamics. After applying the H_x, the magnetization inside the left and right side, DW rotates in opposite chirality and experiences a chirality-depending damping which acts as a dissipative SOT on the DWs. In this case, they have modified the v_0 neglecting DW energy contribution, as:

$$v_0(H_x, T) = \xi_0 f_0 e^{\frac{T_d}{T}} \tag{4.5}$$

where ξ_0 and f_0 are the pinning correlation length and attempt frequency, respectively. The f_0 is inversely proportional to the damping parameter, χ i.e. $f_0 \propto 1/\chi$ [182]. In 2017, Pellegren et al. argued that in the presence of H_x, the DW energy σ becomes anisotropic with respect to the DW orientation in the film plane and neglected the effect of v_0 [183]. They have considered that σ should be dispersive instead of non-dispersive and proposed a dispersive stiffness model, as $\tilde{\sigma} = \sigma + \sigma''$, with $\sigma'' = \frac{\partial^2 \sigma}{\partial \Theta^2}$, where Θ is the azimuthal angle of the DW normal. However, the H_d, obtained from the model, was found to be larger than the field where the minimum velocity is observed. Later, Hartmann et al. modified the model considering the change in the DW stiffness that occurred due to deformation as an angular shape [184]. Further, Lau et al. modified the characteristic speed v_0 in the model as [185],

$$v_0(H_x, T) = v_0^*[1 + \chi^* cos(\phi - \beta)] \tag{4.5}$$

where v_0^* is the modified velocity prefactor independent of H_x, χ^* is the chiral weight, ϕ is the internal magnetization orientation at DW w.r.t H_x and β is the angle between DW normal and H_x. Recently, Davydenko et al., observed the asymmetry in v_L and v_R w.r.t the minima without any cross-over in velocities at higher H_x [181]. They have proposed a model considering both effects in the DW i.e. DW stiffness as well as chiral damping effect. They have considered the

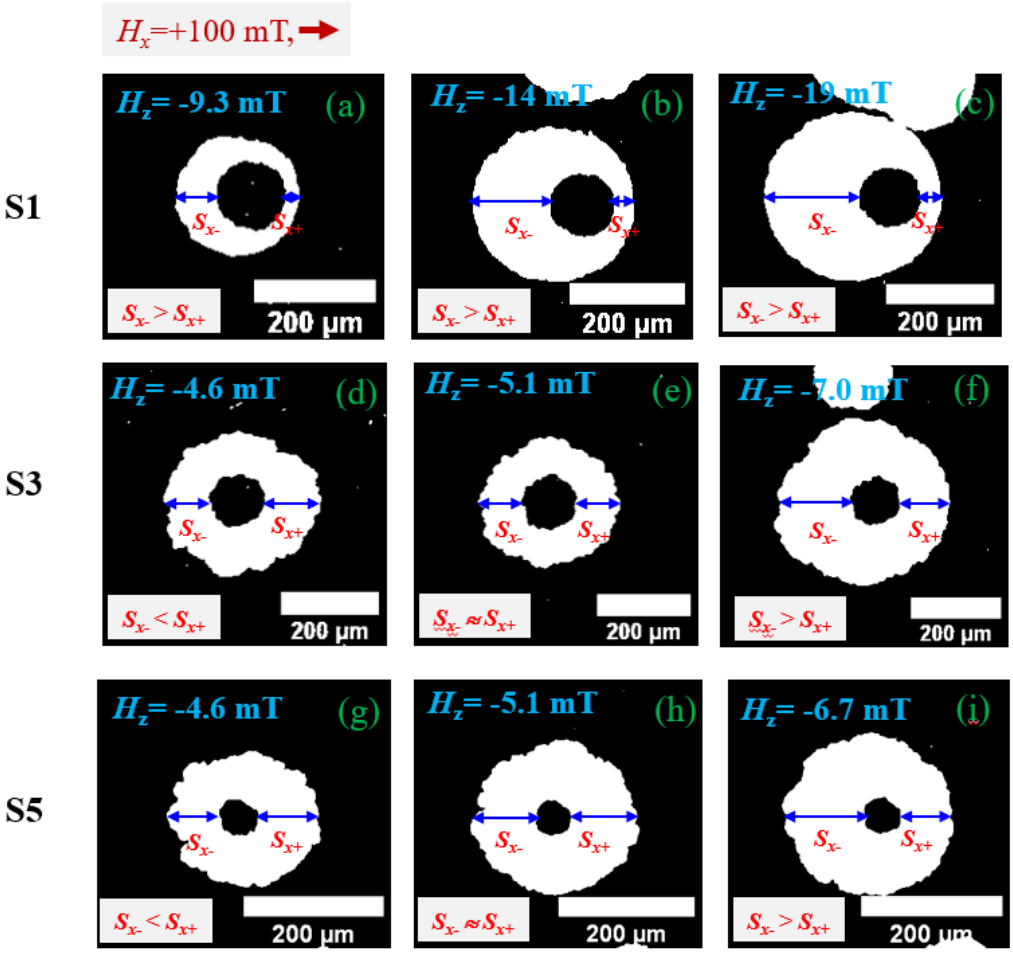

Figure 4.6: Subtracted domains of S1 at H_z=-9.3 mT (a), -14 mT (b), and -19 mT (c); for S3 at H_z=-4.6 mT (d), -5.1 mT (e) and -7.0 (f); for S5 at H_z=-4.6 mT (g), -5.1 mT (h) and -6.7 (i). Here, H_x = +100mT was fixed and the red arrow indicates the direction of H_x.

DW energy, $\tilde{\sigma}$ as proposed by Hartmann *et al.* [184], and the chiral weight, χ^*, as proposed by Lau et al. [185], and extracted the H_d matched well with the field in which DW velocity is minimal. Also, by varying the out-of-plane field (H_z) they have shown that velocity behaviour is independent of H_z. In our case, we have also observed a similar asymmetric nature in v_L and v_R without any velocity crossover for S1 and S2. However, we have seen that the shape of $v_L$or v_R depends on H_z beyond t_{Re}=0.5 nm (in S3, S4 and S5). So, the asymmetry in v_L or v_R might be due to the combined effect of chiral damping and DW stiffness. Most importantly, the chiral

weight, χ^*, may depend on the H_z which may be the reason behind the H_z dependency in v_L or v_R.

To get more insight about it, we have measured the DW velocity at a constant H_x (=100 mT) with varying H_z for samples S1, S3 and S5. First, the domain is nucleated and then H_x =100 mT (along +x) is applied during its propagation. Figure 4.6 shows the subtracted domain images at various H_z for S1 (a-c), S3 (d-f), and S5 (g-i). The DW displacement along +x and -x direction is represented by S_{x+} and S_{x-}, respectively. For S1, S_{x-} is always greater than S_{x+} irrespective of applied H_z. Due to this, the behaviour of v_L and v_R in S1(also in S2) is H_z independent as shown in figure 4.3. However, in S3, three different cases appear i.e. $S_{x-} < S_{x+}$ for lower H_z values (H_z<5.1 mT, as shown in figure 4.6(d)), $S_{x-} \approx S_{x+}$ for intermediate H_z values (H_z ~5.1 mT, as shown in figure 4.6(e)) and $S_{x-} > S_{x+}$ for higher H_z values (H_z >5.1 mT, as shown in figure 4.6(f)). At H_z ~5.1 mT, the DWs move very symmetrically indicating the minimal effect of H_x. Similar behaviour in DW motion is also observed in S5 as shown figure 4.6(g-i) and in S4. These three different scenarios can be correlated to the different behaviour of v_L and v_R in S3-S5.

In summary, a systematic study is performed in chapter 4, to investigate the effect of Re on the DW dynamics. The H_c as well as k_{eff} decreases with increasing the Re thickness up to 1 nm in the Pt/Co/Re(t_{Re})/Ta system. Further, DW dynamics is studied and is found that the pinning energy reduces with t_{Re}. The reduction in k_{eff} and pinning energy reflects in the enhancement of the DW velocity with Re thickness. Also, the insertion of Re in the system enhances the iDMI value significantly which also helps in domain wall velocity enhancement. An iDMI value of ~ 0.7 mJ/m^2 has been extracted from the Co/Re interface. The Pt/Co and Re/Co introduce opposite chirality in the system which basically gives additive effective iDMI. The observed asymmetry in velocity w.r.t the minima may arise due to the combined effect of chiral

damping and DW stiffness. Also, our study indicates that the chiral damping may depend on the out-of-plane field.

Sample name	$\mu_0 H_C$ (mT)	$\mu_0 H_S$ (T)	M_s (MA/m)	K_{eff} (MJ/m^3)	$\delta = \sqrt{\frac{A}{K_{eff}}}$ (nm), where A= 16 pJ/m	$\mu_0 H_{DMI}$ (mT)	$D_{eff} = \mu_0 H_{DMI} M_S \delta$ (mJ/m^2)
S1 (t_{Re}=0.0)	~13	1.25	1.21	0.75	4.62	~200	-1.10 ± 0.09
S2 (t_{Re}=0.2)	~10.58	1.0	1.24	0.62	5.08	~200	-1.25 ± 0.11
S3 (t_{Re}=0.5)	~7.47	0.85	1.26	0.53	5.49	~240	-1.65 ± 0.16
S4 (t_{Re}=1.0)	~7.47	0.76	1.27	0.48	5.77	~240	-1.75 ± 0.16
S5 (t_{Re}=2.0)	~7.47	0.74	1.28	0.47	5.83	~240	-1.78 ± 0.17

Table 4.1: Parameters of the Pt/Co/Re(t_{Re})/Ta multi-layered samples (S1-S5)

Chapter 5

Topological Hall effect in Pt/Co/X (X=Ta, Re) system:

Magnetic skyrmions are non-collinear, swirling, chiral topological spin textures. Recently, skyrmions have been immensely studied as they have high thermal stability, nanoscale size, and the requirement of low driving critical current density [7,8]. It is predicted that skyrmions could be used in next-generation data storage density, racetrack memory, logic devices, transistor-like devices, neuromorphic computing, etc. [7–9,14]. Through a complicated interplay of exchange interaction, magnetic anisotropy, interfacial Dzyaloshinskii-Moriya interaction (DMI), dipolar energy, and Zeeman energy, skyrmions stabilize in a thin film [72,172,186]. However, in specific circumstances, frustrated interaction, four-spin interaction, exchange bias, etc. also play a significant role in the formation of a skyrmion [82,84]. To meet the requirement of practical applications, skyrmions have been investigated in several ferromagnetic systems, ferromagnetic alloys, ferrimagnet, synthetic anti-ferromagnet, and recently in 2D materials [98,187,188]. The interaction of skyrmions with conduction electrons leads to exotic electrodynamics [189]. While a conduction electron (due to the applied current density) moves through chiral spin textures i.e., skyrmions, chiral domain walls, etc., the spin of the electron follows spatially varying local magnetization, if there is sufficient exchange interaction between the local magnetic moment and the conduction-electron spin. From the electron frame of reference, the electron experiences a time-dependent magnetic field due to a non-zero scalar spin chirality ($\chi_{ijk} \sim \boldsymbol{S}_i \cdot \boldsymbol{S}_j \times \boldsymbol{S}_k \neq 0$) i.e., the solid angle occupied by the non-coplanar magnetization directions which leads to a Berry phase in real

space [190,191]. Now the Berry phase deflects the conduction electron perpendicular to the current flow direction and adds an additional contribution to the Hall signal which is known as the topological Hall effect (THE). THE is a very useful and efficient tool to confirm the existence of skyrmion in a system. Therefore, while current pass through a sample the total Hall resistivity (ρ_{xy}) can be expressed as [74,191,192],

$$\rho_{xy} = \rho_{OHE} + \rho_{AHE} + \rho_{THE} = R_0 H + R_s M(H) + \rho_{THE} \quad (5.1)$$

where R_0 and R_s are the ordinary and anomalous Hall coefficient and $M(H)$ is the out-of-plane magnetization as a function of the applied field (H). The first and second term of the equation 5.1 is ordinary (ρ_{OHE}) and anomalous Hall resistivity (ρ_{AHE}), respectively. Thus, topological Hall resistivity (ρ_{THE}) can be quantified by subtracting the ρ_{OHE} and ρ_{AHE} from ρ_{xy}. At higher fields (above the saturation field) all the spins align along the field direction which leads to a ferromagnetic ground state and the ρ_{THE} vanishes. In this condition, ρ_{AHE} get saturated and ρ_{xy} varies linearly with the field. Thus, after correcting the slop of ρ_{xy} at higher field values, ordinary Hall contribution can be eliminated. Then the equation 5.1 can be modified as,

$$\rho_{xy} = R_s M(H) + \rho_{THE} \quad (5.2)$$

As above saturation field ρ_{AHE} saturates and ρ_{THE} = 0, then equation 5.2 modified as,

$$\rho_{xy}^{sat} = R_s M_s \quad (5.3)$$

Now, using the R_s value in the equation 5.2, the ρ_{THE} can be extracted,

$$\rho_{THE} = \rho_{xy} - \frac{\rho_{xy}^{sat}}{M_s} M(H) \quad (5.4)$$

First, THE was observed in non-centrosymmetric crystalline structures (B20-type bulk materials) [193]. Later, it has been also explored in thin film having iDMI [24,74,192,194]. Heavy metal (HM_1)/Ferromagnet (FM)/HM_2 is an ideal thin film system to stabilize skyrmion

and to study THE [24,194]. It has been predicted that the Pt/Co/Re system possesses a huge iDMI interaction (iDMI constant, D ~9.17 mJ/m^2) than any other thin film system like Pt/Co/W, etc. [177,178]. In the previous chapter, we have also observed that the iDMI value is enhanced from ~1.1 to ~1.8 mJ/m^2 after the insertion of Re in a Pt/Co/Re/Ta system. Also, the Pt and Re induce opposite chirality, and the iDMI arising from Pt/Co and Co/Re added up. Thus, it is very important to study the THE in such a system with an additive iDMI for fundamental study as well as for practical application purposes.

In this context, we have prepared Pt/Co/Ta and Pt/Co/Re thin films having PMA and have studied the THE. The topological Hall resistivity indicates the presence of skyrmions in the samples which has been confirmed by magnetic force microscopy (MFM) imaging. Further, topological Hall resistivity as a function of field has been studied. For a deeper understanding of the different types of Hall signatures, we conducted micromagnetic simulations. Further, simulating the hysteresis loops we predict iDMI value (D) present in the Pt/Co/Ta and Pt/Co/Re systems.

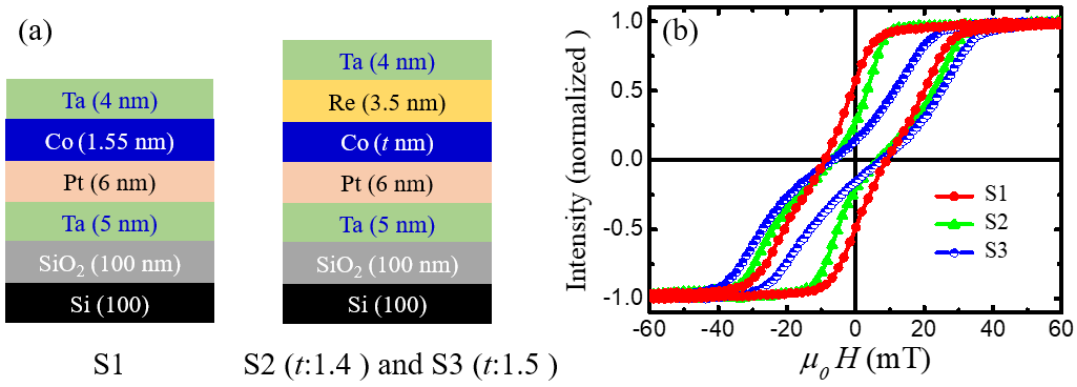

Figure 5.1 (a) Schematic of the sample structures. (b) Polar MOKE hysteresis loops of the samples S1-S3.

5.1 Sample details:

The samples Ta(5)/Pt(6)/Co(1.55)/Ta(4), Ta(5)/Pt(6)/Co(1.4)/Re(3.5)/Ta(4) and Ta(5)/Pt(6)/

Co(1.5)/Re(3.5)/Ta(4) have been prepared on 100 nm thermally oxidized Si substrates and named as S1, S2 and S3, respectively. The numbers in parenthesis refer to the thickness of different layers in nm. A schematic representation of the samples is shown in figure 5.1 (a). DC magnetron sputtering has been used to deposit the Ta, Pt, and Co layers, whereas RF magnetron sputtering has been used to prepare the Re layer with a base pressure $< 8 \times 10^{-8}$ mbar. The substrate table has been rotated with 10 rpm during the deposition to achieve uniform layers.

Sample	H_s (mT)	M_s (A/m)	K_{eff} (MJ/m^3)
S1	650 ± 30	(1.63 ± 0.14) × 10^6	0.53 ± 0.05
S2	720 ± 35	(1.51 ± 0.13) × 10^6	0.54 ± 0.05
S3	600 ± 30	(1.53 ± 0.12) × 10^6	0.46 ± 0.04

Table 5.1: The values of H_s, M_s, and K_{eff} of samples S1-S3 obtained from SQUID measurements.

5.2 Magnetic Characterization:

5.2.1 Magnetic reversal: Magneto optic Kerr effect (MOKE) based microscopy has been used to measure the hysteresis loops of the samples. Figure 5.1 (b) shows the polar MOKE hysteresis loops of the samples and confirms that the easy axis lies along the out-of-plane direction of the samples. Also, the low remanence slanted hysteresis loop indicates the presence of chiral textures in the samples. The effective anisotropy (K_{eff}) of the samples has been quantified using SQUID magnetometry. To evaluate the effective anisotropy (K_{eff}) we have used the equation, $K_{eff} = \frac{1}{2}\mu_0 H_s M_s$, where H_s is the in-plane saturation field and M_s is the saturation magnetization. The SQUID loops are shown in figure 5.2 and the values of H_s, M_s and K_{eff} are listed in table 5.1.

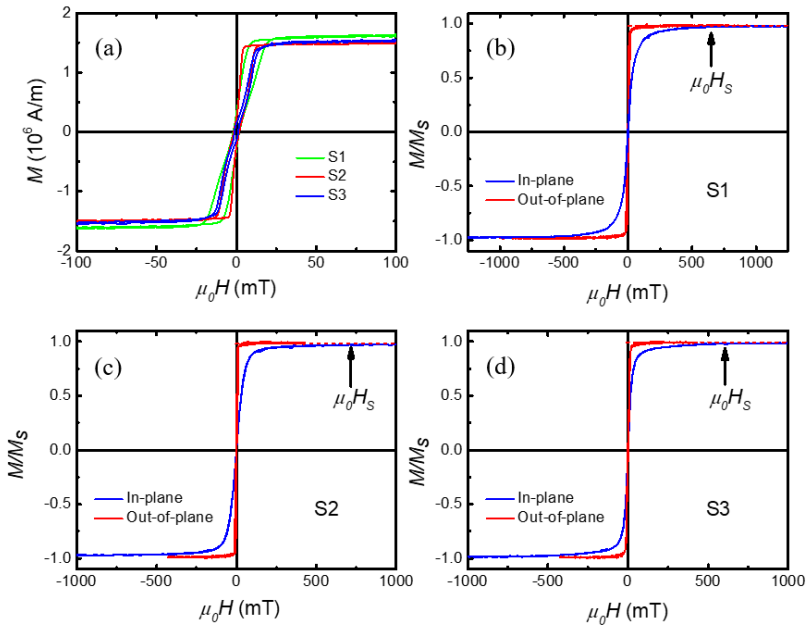

Figure 5.2: (a) Magnetization as a function of field for S1, S2 and S3. The out-of-plane and in-plane hysteresis loops of S1, S2 and S3 are shown in (b), (c) and (d), respectively.

5.2.2 Magnetic Force microscopy: Further, magnetic force microscopy has been used for imaging skyrmions in sample S1. The MFM measurements are performed at NISER, India using commercially purchased MFM tips (Nanosensor-SSS-MFMR). Figure 5.3 (a-d) shows the field evolution of skyrmion from a worm-like phase. At a demagnetized state worm-like domain is observed, as shown in figure 5.3 (a). Further, increasing the field the worm-like domains start to contract into isolated skyrmions figure 5.3 (c-d). At higher fields, skyrmion density got reduced and finally, a saturated state is achieved. It should be noted that MFM cannot provide any information about the internal magnetization profile of the created textures. Electrical measurement is one of the possible solutions to confirm the chiral nature of created textures. Thus, topological Hall effect (THE) has been performed which is explained in detail in the next section.

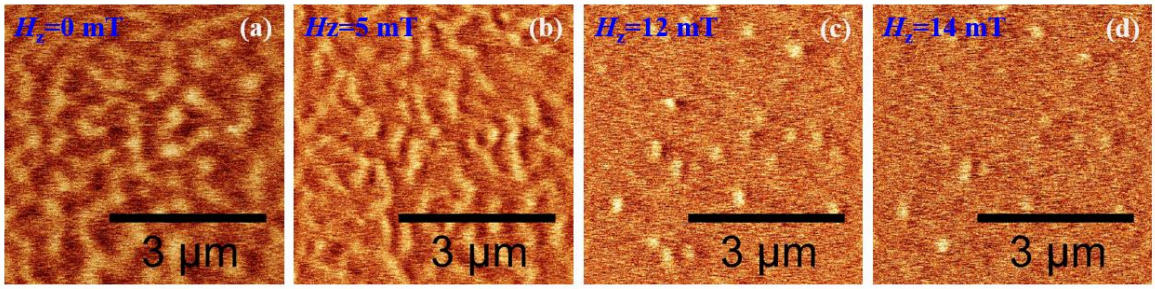

Figure 5.3: (a-d) Field-dependent MFM images for sample S1 exhibiting the process of skyrmion formation. The isolated skyrmions are observed at $H_z \geq 12$ mT.

We have also performed the MFM imaging for samples S2 and S3. However, due to higher stray field of the MFM tip, the textures are saturated during the scanning as shown in figure 5.4 (a) and (b) for samples S2 and S3, respectively.

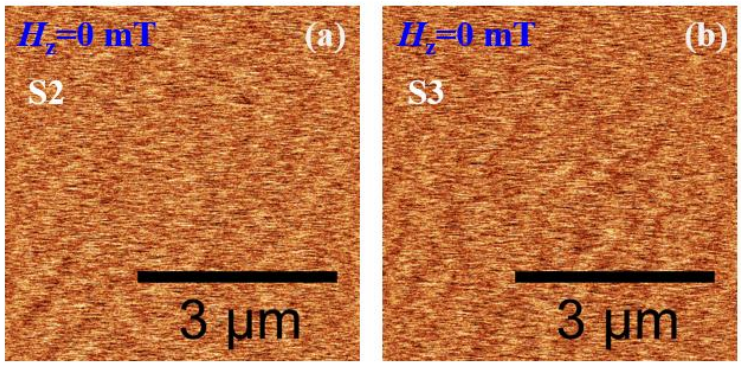

Figure 5.4: (a) and (b) MFM images of S2 and S3 at demagnetized states, respectively.

5.2.3 Topological Hall effect: THE measurements have been performed via a physical property measurement system (PPMS) in ± 3T field in the five probes geometry. The five probes geometry is explained in detail in chapter 2 (section 2.4) [151,195]. A small AC current density (~10^6 A/m^2) has been used for the transport measurements so that the spin textures do not get perturbed. In a FM material, the total Hall resistivity (ρ_{xy}) is the sum of three contributions i.e., ordinary (ρ_{OHE}), anomalous (ρ_{AHE}) and topological (ρ_{THE}) Hall resistivity. The ordinary Hall effect (OHE) is linearly proportional to the applied field. The anomalous

Hall effect (AHE) arises due to the time-reversal symmetry breaking in the FM and is linearly proportional to the magnetization. THE originated in a thin film due to the presence of nontrivial spin texture like skyrmions. [75,192,193]. Thus, ρ_{THE} can be extracted by subtracting the other two components from ρ_{xy}. Now, the OHE contribution has been subtracted from ρ_{xy} by fitting a linear function above 1.5 T and the remaining (AHE + THE) components as a function of *H* have been shown in figure 5.5 (a-c). At higher fields, the AHE contribution got saturated and the R_s can be deduced as, $R_S = \frac{\rho_{xy,saturation}}{M_S}$ [192,196]. Hence, the AHE components have been determined by scaling the *M-H* loops with R_s. Now, the ρ_{THE} is quantified after subtracting the AHE contributions from the remaining resistivity. The ρ_{THE} as a function of the field is shown in figure 5.5 (d-f) for all the samples. A maximum ρ_{THE} of ~ 0.08, ~ 0.12 and ~ 0.10 nΩ-m have been observed for the sample S1, S2 and S3, respectively. The topological Hall resistivity confirms the presence of chiral structures in the samples. The ρ_{THE} is proportional to the average topological charge or skyrmion number [192]:

$$\rho_{THE} = R_T \langle Q_{sk} \rangle \tag{5.5}$$

The average skyrmion number, $\langle Q_{sk} \rangle$, is the sum of the skyrmion numbers, Q_{sk}, of all individual objects present in the sample. The topological Hall coefficient, R_T, represents the carrier density and spin-polarization of the carriers. The Q_{sk} is defined as a product of vorticity (V) and core polarity (P) of the texture (i.e. $Q_{sk} = V \cdot P$). The vorticity, V= +1 for skyrmion. So, depending upon the core polarity (+1 or -1), Q_{sk} could be either +1 or -1 which basically defines two distinct phases of topological objects. It should be noted that during the field sweep from +ve to -ve saturation field (or vice versa), we have observed a single peak in ρ_{THE} for S1 (figure 5.5 (b)) which signifies only one type of texture. Whereas two peaks (one along +ve and another along -ve ρ_{THE} axis, in the rest of the chapter we called it as a double peak with opposite sign) have been noticed for samples S2 (figure 5.5 (d)) and S3 (figure 5.5 (f)) during the field sweep.

Now, a sign change in R_T is only possible by changing the temperature [192]. As all the measurements are performed at room temperature, for double peak, sign change in ρ_{THE} solely depends on Q_{sk}. During the field sweep, the core polarity switches, hence, two distinct textures could be observed in this case (later described in detail). Additionally, from MFM scanning on S1, it has been found that the chiral textures are skyrmions, as shown in figure 5.3. As the skyrmions are not imaged via MFM for S2 and S3, the MuMax simulations help to get an idea about the chiral textures.

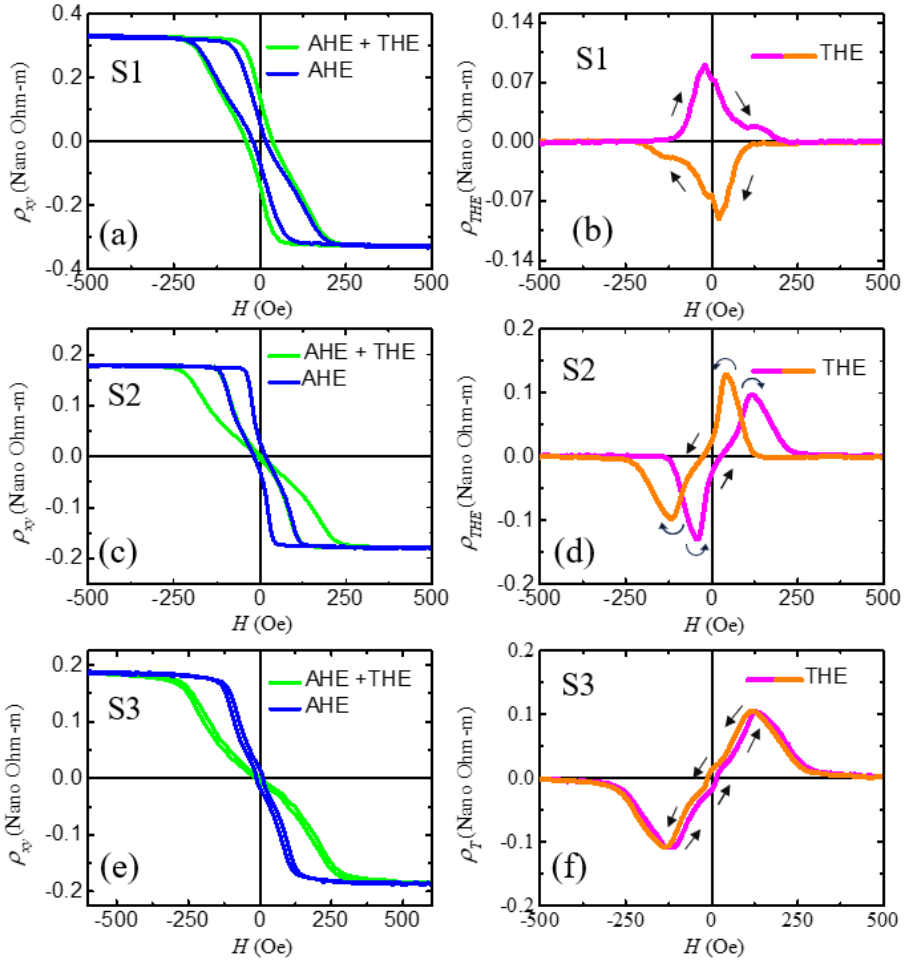

Figure 5.5: (a), (c), and (e) AHE+THE and AHE contribution in ρ_{xy} as a function of field for S1, S2 and S3, respectively. (b), (d) and (f) plots of ρ_{THE} vs field for S1, S2 and S3, respectively. The black arrow sign represents the field sweep direction.

5.3 MUMAX3 simulation: MuMax is a GPU-based micromagnetic simulator that is developed and maintained by the DyNaMat group at Ghent University [197,198]. It is a free and open-source software. It is designed using Go and CUDA languages, that is distributed under the GPLv3 license. It evaluates the space and time-varying magnetization dynamics over a range of nano to micrometer-scaled ferromagnet using a finite-difference (FD) discretization method. This method basically discretizes the space using 2D or 3D grids of orthorhombic cells. In MuMax3, input scripts are written in a language similar to a subset of Go. Simulations of a system can be performed quite sophistically with the software. Similar to OOMMF, in MuMax3, all space-dependent input and output values are saved in a ".OVF" format. MuMax3 calculates the time-dependent change in reduced magnetization $\vec{m}(r,t)$, by solving the LLG equation. The LLG equation is solved using a few explicit Runge-Kutta (RK) techniques, e.g., RK45, RK32, and RK23. To start a simulation, all the prior information like simulation area, cell size, boundary conditions, saturation magnetization, anisotropy, exchange constant, applied field range, etc. need to be mentioned in a script. At each step of the simulation, MuMax3 determines the minimum energy state of a system using a relax () function. In this chapter, MuMax3 is used to reproduce the experimentally obtained hysteresis loops and to understand the experimental results. The simulations are carried out at 0K, leading to a discrepancy between the experimental results and the simulations. Nevertheless, we have qualitatively reproduced the experimental findings. The simulation area was 2 μm × 2 μm. The cell size was 2 × 2 × 1.55 (or 1.4) nm^3. The values of M_s and K_{eff} used in the simulation are very close to experimentally obtained values. The exchange constant, A = 25 pJ/m has been considered in the simulation. To obtain a realistic response, the simulation region was divided into grains of size 10 nm using random Vorronoi tessellation [194,197,198]. We have also used periodic boundary conditions (PBC) in the simulations. We have simulated the hysteresis loops of S1 and S2 by considering the M_s and K_{eff} values very close to the experiment. The values of

M_s used for samples S1 and S2 in the simulation are 1.65×10^6 and 1.53×10^6 A/m, respectively. In addition, the values of K_{eff} used for samples S1 and S2 in the simulation are 0.53 and 0.54 MJ/m^3, respectively. The uniaxial anisotropy has been calculated using the relation, $K_u = K_{eff} + \frac{1}{2}\mu_0 M_s^2$. As a sizeable topological Hall resistivity has been found in the samples, therefore a finite iDMI value could be expected from these samples. Thus, several hysteresis loops have been simulated by varying the iDMI constant, D, with the fixed values of M_s and K_{eff}. It has been observed that for D = 1.05 (figure 5.6 (a)) and 1.2 mJ/m^3 (figure 5.6 (e)), the simulated hysteresis loops match well with the experimental ones as measured for samples S1 and S2, respectively.

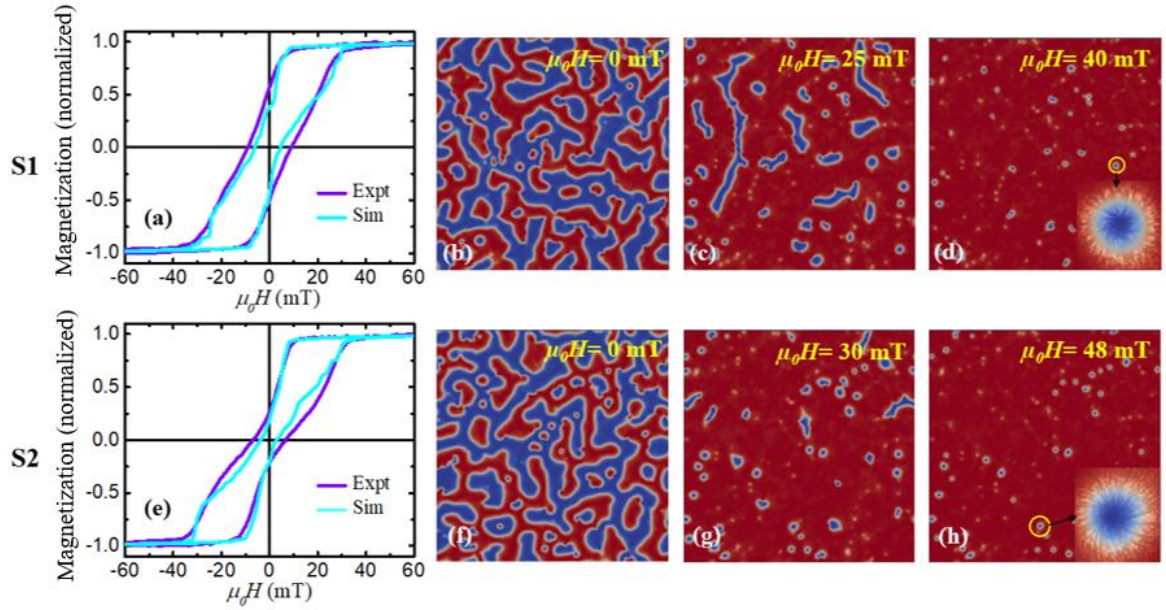

Figure 5.6: (a) and (e) simulated (cyan colour) and MOKE (violet colour) hysteresis loops of S1 and S2, respectively. (b-d) and (f-h) reveals the field-induced simulated domain images for S1 and S2, respectively.

Further, the evaluation of skyrmion as a function of field has been studied, as shown in figure 5.6 (b)-(d) and (f)-(h) for S1 and S2, respectively. In this case, we have considered the random magnetization as an initial magnetic configuration and then relaxed the system to obtain the

zero-field state (figure 5.6 (b) and 5.6 (f)). With increasing the field, the worm-like domains break into isolated skyrmion (figure 5.6 (d) and 5.6 (h)). However, the skyrmions are mixed phase (Néel+Bloch) in nature. With increasing the D up to 1.3 (for S1) and 1.5 mJ/m^2 (for S2), pure Néel skyrmions can be obtained. However, in such cases, the simulated hysteresis loops do not match with experiment. So, from the discussion, it can be predicted that the D should be ~ 1 and 1.2 mJ/m^2 in S1 and S2, respectively.

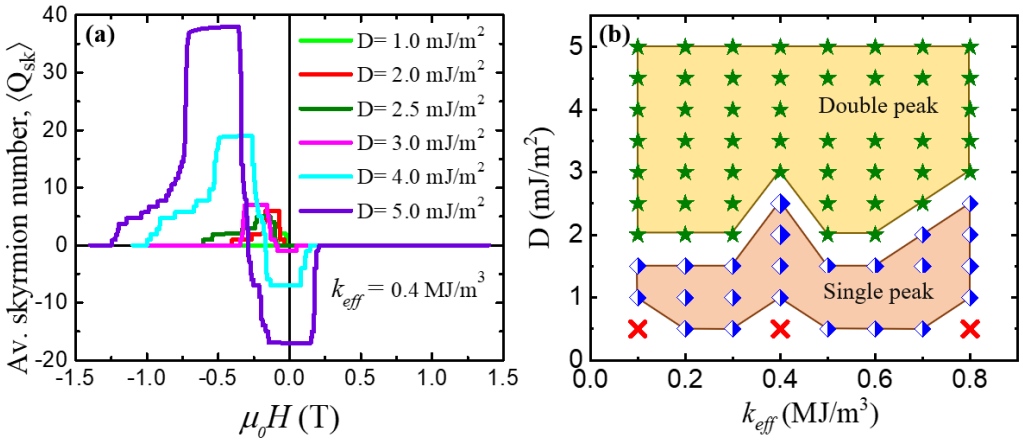

Figure 5.7: (a) Plot of $\langle Q_{sk} \rangle$ vs $\mu_0 H$ at a constant K_{eff}. (b) A phase plot of D vs K_{eff} which shows the single to double peak transition in $\langle Q_{sk} \rangle$ or ρ_{THE}. The red cross mark represents no skyrmion during the field sweep.

Further, the reason behind the different shapes of ρ_{THE} (figure 5.5 (b) and (d)) in samples S1 and S2, have also been understood via micromagnetic simulations. Previously, this kind of a single peak [199,200] or double peak (i.e., double peak with opposite sign) [24,74,201,202] in resistivity was already observed in different thin films. P. K. Sivakumar et al., have explained that a double peak (with the same sign) in topological resistivity comes due to the presence of skyrmions and anti-skyrmion having the same topological charge in a MgO (001)/Mn_2RhSn system [192]. However, why a single peak or double peak (with opposite sign) arises in the Hall signature, has not been explored yet. In the simulations, the magnetization of the system

has been changed from +ve to -ve saturation state by varying the applied field with a small step, and in every field value the average skyrmion number, $\langle Q_{sk} \rangle$, has been calculated using 'ext_topologicalcharge' command in Mumax3 [197,198]. It should be noted that $\langle Q_{sk} \rangle$ corresponds to the ρ_{THE} according to equation 5.5. Hence, $\langle Q_{sk} \rangle$ can provide information about the ρ_{THE} of a system. As iDMI defines the chirality of a system, we have varied the iDMI value, D, in a range of 0.5-5.0 mJ/m^3 considering M_s = 1.53 × 10^6 A/m and K_{eff} = 0.4 MJ/m^3.

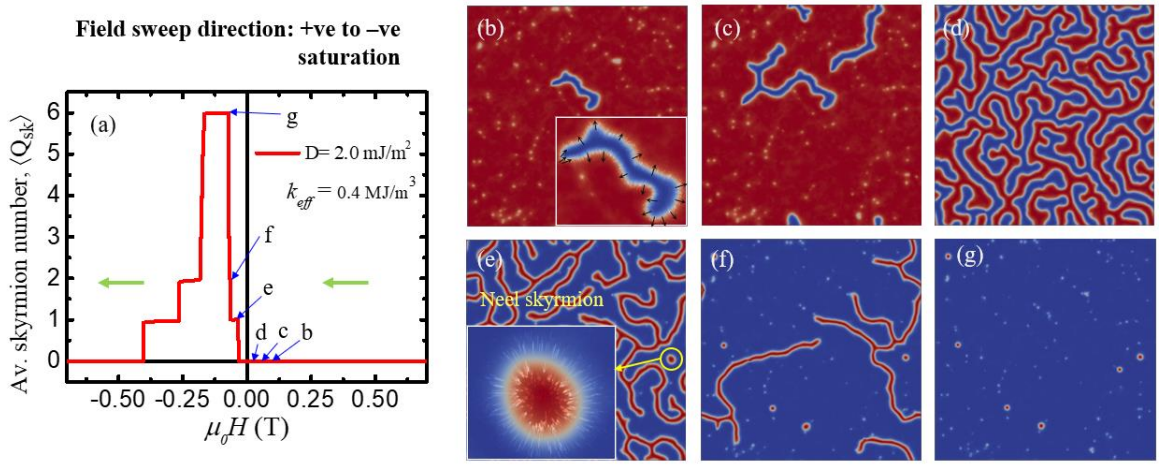

Figure 5.8: (a) A single peak in $\langle Q_{sk} \rangle$ for D= 2.0 mJ/m^2 and K_{eff}= 0.4 MJ/m^3. The blue arrows refer to the corresponding domain structures as shown in (b-g). The green arrow represents the field sweep direction.

Figure 5.7 (a) shows the $\langle Q_{sk} \rangle$ as a function of field. A single peak in $\langle Q_{sk} \rangle$ has been observed up to D = 2.5 mJ/m^3 and beyond it, double peaks have been observed. As the anisotropy of the system plays a major role in deciding the minimum energy state, the K_{eff} also has been varied in the simulation over a range of 0.1-0.8 MJ/m^3. A phase plot of D vs K_{eff} has been shown in figure 5.7 (b). It has been observed that the shape of $\langle Q_{sk} \rangle$ or ρ_{THE} depends on the D and K_{eff} and using a proper combination of them, single to double peak transition in ρ_{THE} can be achieved. Thus, the nature of the topological Hall signal of a system solely depends on the D and K_{eff} values.

For a single peak in $\langle Q_{sk} \rangle$ (figure 5.8 (a), considering D = 2 mJ/m^2 and K_{eff}= 0.4MJ/m^3), while the field has been reduced from a positive saturation, the reversed domain with Q_{sk} = 0 has been nucleated (see figure 5.8 (b)). Further, by reducing the field the reverse domain expands (figure 5.8 (c)) and is interconnected with neighbouring domains to form a work-like structure (figure 5.8 (d)). Now, the worm-like domain breaks into skyrmions with Q_{sk} = +1 (figure 5.8 (e)-(g)) with decreasing the field (i.e., increasing the field -ve direction) and contributing to Hall resistivity. At a higher field again oppositely saturated FM ground state has been achieved. Thus, it should be noted that the peak in $\langle Q_{sk} \rangle$ or ρ_{THE} comes due to only one type of topological object.

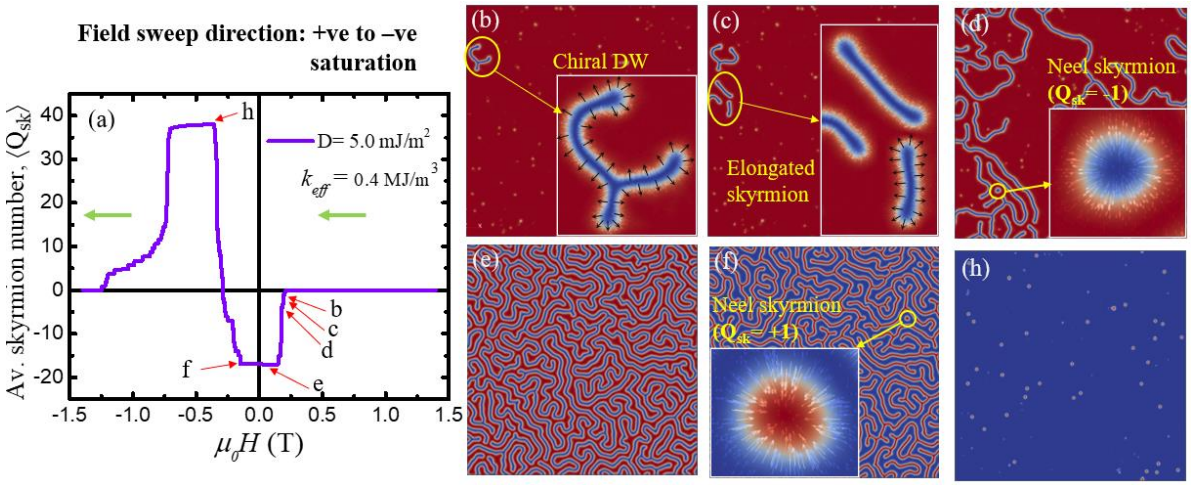

Figure 5.9 (a) A double peak with opposite sign in $\langle Q_{sk} \rangle$ for D= 5.0 mJ/m^2 and K_{eff} = 0.4 MJ/m^3. The red arrows refer to the corresponding domain structures as shown in (b-g). The green arrow represents the field sweep direction.

In the case of a double peak, (figure 5.9 (a), considering D= 5 mJ/m^2 and k_{eff}= 0.4MJ/m^3) while decreasing the field, several reverse nuclei occur in terms of chiral domain walls (DW), elongated skyrmions or skyrmions (due to presence of high iDMI) which contribute to Q_{sk} = -1. With increasing the field in the reverse direction, the nuclei expand and merge with nearby topological objects and a chiral worm-phase has been achieved giving a maximum value Q_{sk}=

-17 (figure 5.9 (e)). Further, with the field, the stripe phase again breaks into a skyrmion with opposite polarity i.e., Q_{sk} = +1 (figure 5.9 (f)), and finally, a state with maximum isolated skyrmions (Q_{sk} = +38) is achieved (figure 5.9 (h)). Therefore, the double peak in $\langle Q_{sk} \rangle$ or ρ_{THE} is formed by the contribution of two topological objects with opposite polarity. For the above discussion, it could be concluded that the k_{eff} is very similar in S1 and S2, however, DM interaction is higher in S2 than in S1, that might be induced the double peak in S2.

In summary, we have observed the skyrmion in Pt/Co/Ta and Pt/Co/Re systems. The chiral nature of texture is confirmed by performing the THE measurement. Two different types of behaviour in topological Hall resistivity are observed for the Pt/Co/Ta and Pt/Co/Re. As seen, the effective anisotropy (k_{eff}) and DMI interaction play a pivotal role in determining the topological Hall behaviour in a system. By choosing a proper combination of k_{eff} and iDMI value (D) of a system, one can achieve single to double peak transition. Also, by simulating the hysteresis loops we have predicted that the iDMI for Pt/Co/Ta and Pt/Co/Re system could be ~ 1.0 and 1.2 mJ/m^2.

Chapter 6

Current induced motion of skyrmion in Pt/CoFeB/MgO thin film:

From the experimental perspective, there are three major challenges in the field of skyrmion: (i) stabilization of skyrmions at room temperature, (ii) deterministic nucleation of skyrmions, and (iii) efficient motion of skyrmions under spin Hall effect (SHE). Over the last decade, many experimental works [72,74,187,203] have been focused in the aforementioned directions to achieve the ambitious goal of skyrmion-based device applications. Recent works have revealed that the skyrmions can be stabilized, nucleated, and driven using an external magnetic field [72,187], electrical field [204], spin-polarized current pulses [72,187,203], local field gradient [90], anisotropy gradient [205], etc. However, controlled nucleation and motion of individual skyrmions in nanotracks with low power consumption still remain a challenge. A crucial criterion for device applications is to drive the skyrmions at low power. This makes materials with low pinning energy landscape indispensable. Different mechanisms (i.e. particle model-based numerical analysis, current-driven motion of skyrmion via nanotrack, skyrmion defect interactions, etc.) suggest that a skyrmion can move around a defect as well as get pinned depending on the pinning sites, applied current density, etc [203,206]. Further, it is well established that at lower current densities, the effect of pinning on magnetic textures is more relevant than at larger current densities [207]. One way of optimizing material properties to minimize pinning is to use disordered systems [208]. However, in spite of several works in this field, the required threshold current density to drive the skyrmions has yet to reach the desired limit for real-life applications. In this context, we chose the combination of

$Pt/Co_{40}Fe_{40}B_{20}/MgO$ to investigate the current-driven dynamics of the skyrmions under the influence of SOT. CoFeB has been selected due to the presence of lower pinning potential in comparison to polycrystalline FM layers (viz., Co, Fe, etc.) [187]. In addition, it has been observed that a CoFeB-based perpendicular magnetic anisotropic system [209] exhibits the requirement of a lower threshold current density in current-induced Domain wall motion than a Co/Pt [210] or Co/Ni [211] system.

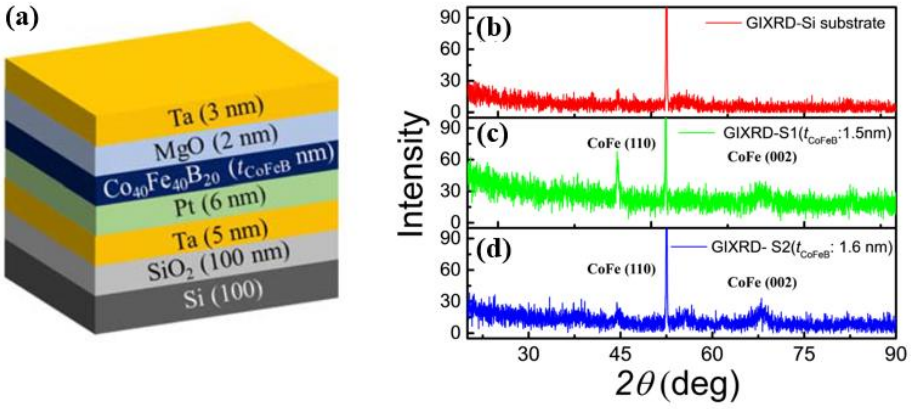

Figure 6.1: (a) Schematic of sample structure. GIXRD measurements of the bare substrate and the samples S1 and S2 are shown in (b), (c) and (d), respectively. For proper comparison, the intensity axis scale is the same for all the plots

6.1 Sample details: We have prepared Ta (5nm)/Pt (6nm)/$Co_{40}Fe_{40}B_{20}$ (t_{CoFeB})/MgO(2nm)/Ta (3nm) heterostructure, on thermally oxidized Si/SiO_2(100nm) substrates. The schematic of the sample structure is shown in figure 6.1(a). We choose SiO_2 100 nm, since it leads to better signal in the optical measurements. A Ta seed layer has been chosen to promote the (111) growth of Pt as well as to reduce the strain between Pt and the substrate. We also use a 3 nm Ta layer on the top as a capping layer. The samples are named as S1, S2 for t_{CoFeB} = 1.5 and 1.6 nm, respectively. However, initially t_{CoFeB} has been scanned from 1.1 to 1.7 nm to find the spin reorientation transition (SRT) and then we kept the t_{CoFeB} values close to the SRT to balance

the total energy of the system favourable to host skyrmions. The sample preparation was performed in a high-vacuum chamber consisting of sputtering and e-beam evaporators. The base pressure of the chamber was better than 8×10^{-8} mbar. Ta, Pt, and CoFeB layers were deposited using DC magnetron sputtering while the e-beam evaporation technique was employed to prepare the MgO layer. The substrate has been rotated with 10 rpm during deposition to improve the uniformity of the layers. Further, for deposition of CoFeB the Ar flow was kept at 10 sccm which allows uniform growth of the thin film. The growth pressure and rate of deposition for CoFeB were 8×10^{-4} mbar and 0.01 nm s^{-1}, respectively. We have used a commercially purchased $Co_{40}Fe_{40}B_{20}$ stoichiometric target to prepare our thin films. However, from the Energy Dispersive x-ray (EDX) analysis measurements for sample S2, it is observed that the amounts of Co, Fe, and B are found to be 43%, 41%, and 16%, respectively (see figure 6.2). The roughness of the sample is observed to be 0.20 nm from AFM measurements (see figure 6.5 (a)). In order to promote the interfacial perpendicular magnetic anisotropy (PMA), all the samples were annealed in-situ at 600°C for 1 h in a vacuum (~1×10^{-7} mbar), after deposition.

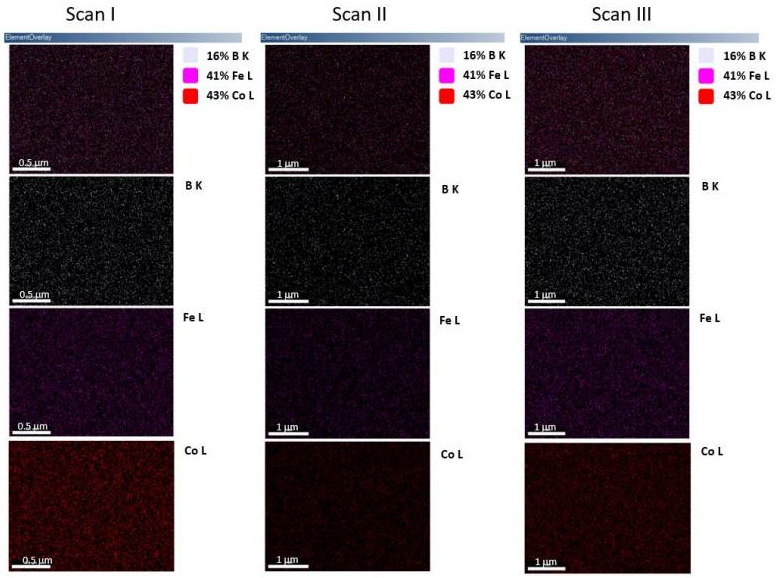

Figure 6.2: EDX scan on sample S2 (t_{CoFeB}=1.6 nm) at three different areas

6.2 Structural Characterization: The crystalline nature of the samples has been investigated using x-ray diffraction (XRD) measurements. From grazing incidence x-ray diffraction (GIXRD) data, we obtained peaks with low intensity in both the samples at ∼45° and ∼68° (figure 6.1 (c-d)), which are not present in the virgin substrate, as shown in figure 6.1 (b). These peaks have been associated to CoFe (110) and (002)-oriented bcc phase previously reported in the literature [212,213]. The partial crystallization of the CoFeB due to in situ annealing originates the perpendicular magnetic anisotropy in the system.

6.3 Magnetisation reversal: The hysteresis loops of the samples have been measured via the magneto-optical Kerr effect-based microscopy (MOKE) in polar mode at our laboratory LNMM, NISER. We observe that the sample with 1.10 nm thick CoFeB leads to PMA with a square hysteresis loop, whereas the sample with t_{CoFeB} = 1.7 nm shows hysteresis with in-plane anisotropy, as shown in figure 6.3. However, the shape of the hysteresis in figure 6.3(a) for samples t_{CoFeB} = 1.5 nm (S1) and t_{CoFeB} = 1.6 nm (S2) show a sharp change in magnetization (from one saturated state) followed by a relative slow variation before reaching the other saturated state. Usually, in the presence of a finite iDMI and vanishing magnetic anisotropy, such a hysteresis loop indicates the presence of a textured (stripes, bubbles, skyrmions) phase as the ground state in the sample [214]. Further, at the part of the hysteresis where the saturation is progressive after the initial drop in magnetization, skyrmion-like textures are likely to be stabilized under the presence of a finite external magnetic field. This has been further confirmed by imaging the magnetic states in samples S1 and S2. Further, to quantify the spontaneous magnetization (M_S) of the samples we have performed hysteresis measurements via a SQUID magnetometer. The M_S of samples S1 and S2 is determined to be 1.24×10^6 A/m and ∼ 1.27×10^6 A/m, respectively.

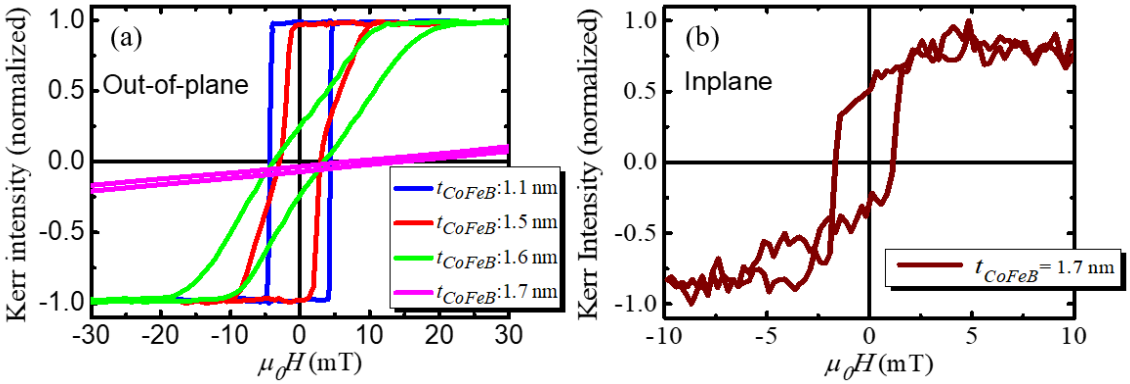

Figure 6.3: (a) MOKE hysteresis loop for the sample with t_{CoFeB}= 1.1-1.7 nm in polar mode. (b) Hysteresis loop for the sample with t_{CoFeB}= 1.7 nm measured at room temperature in the longitudinal mode.

6.4 interfacial DMI (iDMI) quantification: BLS measurements at Laboratoire de Physique des Solides (LPS) have been performed in Damon-Eshbach geometry to quantify the interfacial DMI (iDMI) in the samples [166,167]. Figure 6.4 (a) shows the schematic of the measurement geometry using Brillouin light scattering (BLS) in Damon Eshbach (DE) configuration. In this measurement, a horizontally polarized laser beam is incident on a sample surface where the incident photons interact with magnons. The 180◦ backscattered photons (arise due to inelastic scattering) are sent through a tandem Fabry-Perot (FP) interferometer to achieve a high spectral resolution and to extract the information about spin wave. Stokes (S) and Anti-stokes (AS) peaks arise due to creation and annihilation of the magnons, respectively, in the BLS spectra and the respective spin wave propagates in the opposite direction. The wave vector of the spin wave is represented as $k_{sw} = 4\pi\sin\theta/\lambda$, where θ is the incident angle, and λ (=532 nm) is the wavelength of incident laser light. Here, a magnetic field has been applied perpendicular to the incident plane of light. Figure 6.4 (b) shows the BLS spectra of the sample S2 measured at k_{sw}= 4.1 μm^{-1} and a constant applied field ($\mu_0 H$ = 371 mT).

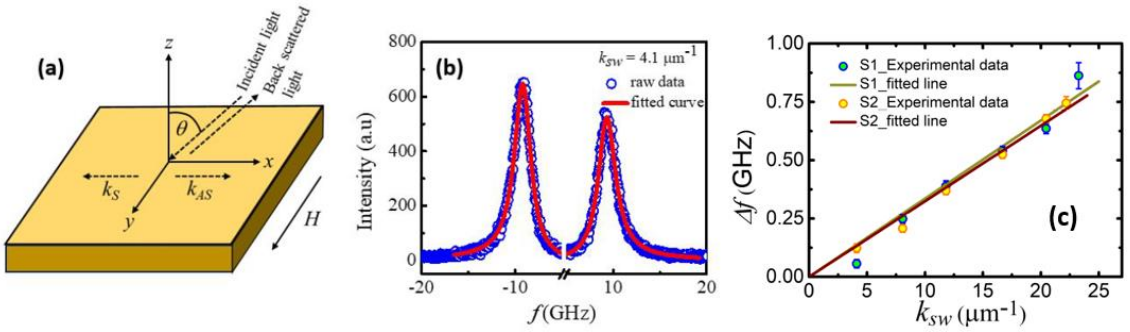

Figure 6.4: (a) Measurements geometry of BLS technique. (b) BLS spectra of sample S2 measured at a constant applied field ($\mu_0 H$ = 371 mT). (c) Plot of frequency difference (Δf) vs spin wave vector (k_{sw}).

The BLS data have been analysed using the following spin-wave dispersion relation in D-E mode [166,167],

$$f = f_0 \pm f_{DMI} = \frac{\gamma \mu 0}{2\pi}\sqrt{[H + Jk_{sw}^2 + P(k_{sw})M_S][H + Jk_{sw}^2 - P(k_{sw})M_S - H_u]} \pm \frac{\gamma}{\pi M_S} D_{eff} k_{sw} \quad (6.1)$$

where, γ is the absolute value of the gyromagnetic ratio [$\gamma/(2\pi) = g \times 13.996$ GHz/T, with g the Landé factor], μ_0 is the vacuum permeability, $J = 2A/(\mu_0 M_S)$ is the spin wave stiffness constant with A the micromagnetic exchange constant, D_{eff} is the effective DMI constant, H_u is the uniaxial anisotropy, $P(k_{sw}) = 1 - \frac{1-\exp(-|k_{sw}|t_{CoFeB})}{|k_{sw}|t}$. The first part of the above equation, $f_0 = \frac{f_S + f_{AS}}{2}$ (f_S and f_{AS} peak frequencies of S and AS lines of BLS measurements), represents the average spin wave frequency having no iDMI at the HM/FM interface whereas the second part arises due to iDMI.

From equation (6.1) the frequency difference between S and AS peaks can be written as:

$$\Delta f = f_S(-k) - f_{AS}(k) = \frac{2\gamma}{\pi M_S} D_{eff} k_{sw} \quad (6.2)$$

The equitation (6.2) shows, Δf has a linear relation with k_{sw}. Δf as a function of k_{sw} has been plotted in figure 6.4 (c) for all the samples. From the slope of linear fit, DMI constant D_{eff} can be deduced. The magnitude of iDMI constants are 0.33 ± 0.03 mJ/m^2 and 0.32 ± 0.02 mJ/m^2 for S1 and S2, respectively.

6.5 Magnetic force microscopy (MFM) measurements: To stabilize isolated skyrmions, we need to fine tune the domain wall (DW) energy [75] between two limiting cases: (a) a large positive energy which causes the collapse of the skyrmions, and (b) a large negative wall energy which destabilizes the collinear order, leading to isolated skyrmions only at a large external magnetic field. One way of achieving this is to keep the FM layer thickness near the SRT to reduce the effective anisotropy energy of the system to near zero. For this work, the thickness of the samples S1 (t_{CoFeB}= 1.5nm) and S2 (t_{CoFeB} = 1.6nm) are chosen close to the SRT. This is confirmed by the presence of skyrmionic states in samples S1 and S2 as observed using MFM. The MFM measurements are performed using a two-pass scan, one for the topography and one at a higher distance (20 nm) to get the magnetic signal from the phase of the tip oscillation. In such a measurement, tip-induced perturbation should occur during the topographic scan, when the tip to sample distance is the lowest. This is why we have used homemade tips that fix this problem. In addition to a magnetic coating (CoCr), we add a Cr capping layer. This last layer is not only meant to protect the magnetic coating but also increases the magnetic layer to sample distance during the topographic scan. This strategy has been successfully used in several studies [75,215,216] on magnetic solitons (skyrmions and domain walls) and prevents dramatic and irreversible perturbations. Here, a topography image of sample S1 is shown in figure 6.5(a)). Further, wormlike stripe domains are observed in the demagnetized state indicating

that the ground state is the spin spiral state (figure 6.5(b)). By applying OOP fields of 1 and 3mT (figures 6.5(c) and (d)), isolated skyrmions have been observed in the samples S1, and S2, respectively. The average size of the skyrmions (measured within the accuracy of the MFM) varies in the range of 200–500 nm and 150–300 nm for samples S1 and S2, respectively. We note from figures 6.5(c), and (d) that the shape of the skyrmions is significantly perturbed even by the stray field of the lowest moment magnetic tips. In the area marked by the cyan-coloured circle in figure 6.5(c), we note that there is a 'flat domain'∼500 nm on the left at the level of the skyrmion which is cut into two domains (skyrmions). This indicates that the skyrmions have jumped to a different pinning point for a few scanning lines. Further, it should be noted that the skyrmions are elongated along the slow scan axis (transverse axis/Y-axis). The reason for such elongation is that the skyrmion has 'more time' to interact with the magnetic tip along the slow scan axis and hence can be dragged progressively providing an elongated shape. Such significant tip-induced perturbations indicate the presence of a low pinning landscape in the samples.

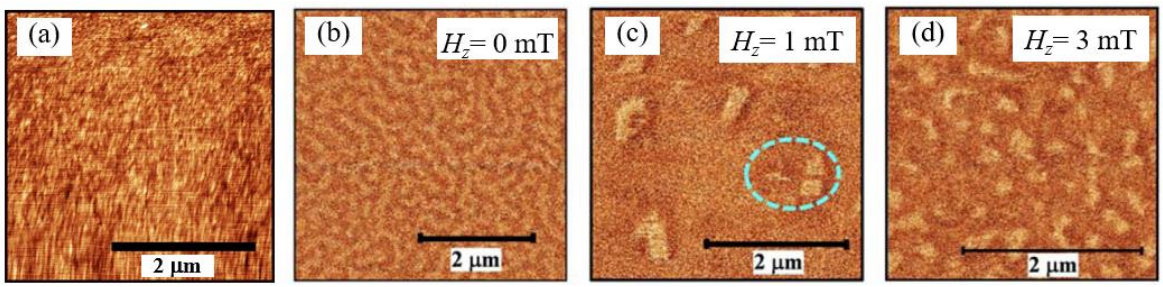

Figure 6.5: (a) an AFM image of sample S1. (b) and (c) MFM images of sample S1 at demagnetized state and at an applied out-of-plane field of 1 mT, respectively. (d) MFM image of sample S2 at an applied field of 3 mT. The cyan circled area in (c) is a guide to the eye for the distorted shape of the skyrmion induced by tip perturbation (horizontal scanning).

A detailed discussion of the moment of the MFM tips and their effect on the magnetic textures is discussed in the following. The consequences of the CoCr layer thickness on the images are

shown in figure 6.6. In this figure, we compare the same demagnetized state using two tips with CoCr(15 nm)/Cr(20 nm) [images 6.4(a) and 6.4(b)] and CoCr(5 nm)/Cr(20 nm) [image 6.4(c)] (same tip which is used for our measurements). The striking difference between the two

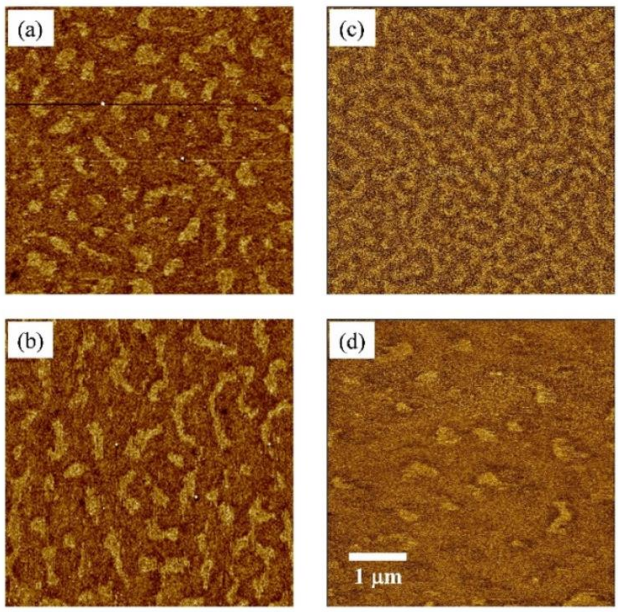

Figure 6.6: MFM image of the CoFeB sample in the demagnetized state (zero field) using a 15 nm/20 nm (a-b) and a 5 nm/20 nm (same tip as in the manuscript) (c) CoCr/Cr bilayers tip. Images (a) and (b) show significant perturbation whereas image (c) shows the expected stripe phase. Note that the different scan directions (respectively x and y fast scan axis) between images (a) and (b) highlight the deformations due to the magnetic tips that show magnetic textures elongated along the slow scan axis. (d) Image obtained with a 3 mT applied field of the skyrmion state, using the 5 nm/20 nm (c) CoCr/Cr bilayers tip. This image shows that in the skyrmion phase, perturbation cannot be avoided. A thinner magnetic coating prevents a good signal being obtained from the samples. The phase scale for all three images is the same (300 mDeg). The image scales are identical, with a scale bar shown in (d).

sets of images is that contrary to the expected stripe state observed with the thinnest CoCr layer tip, the other tip shows more compact structures. This is the result of a significant perturbation that slices the stripes into more compact domains. Changing the scan direction between the x

[image 6.4(a)] and y [image 6.4(b)] fast scan axis proves the perturbation since the observed textures are systematically elongated along the slow scan axis, probably due to a dragging effect by the magnetic tip. Note that if the thinnest CoCr layer tip produces minute perturbation on the stripe phase, the skyrmion state is still slightly perturbed [image 6.4(d) and image 6.3]. This behaviour is likely to be due to the low pinning landscape of the CoFeB thin films. In order to confirm that the tips (CoCr (15 nm)/Cr(20 nm)) used here are soft magnetic in nature we have performed, MFM with the same tips on our previous studied sample [75,214] of [Pt/Ni/Co/Ni/Au/Ni/Co/Ni/Pt] in which the skyrmions have been imaged without any perturbations (i.e. without any distortion).

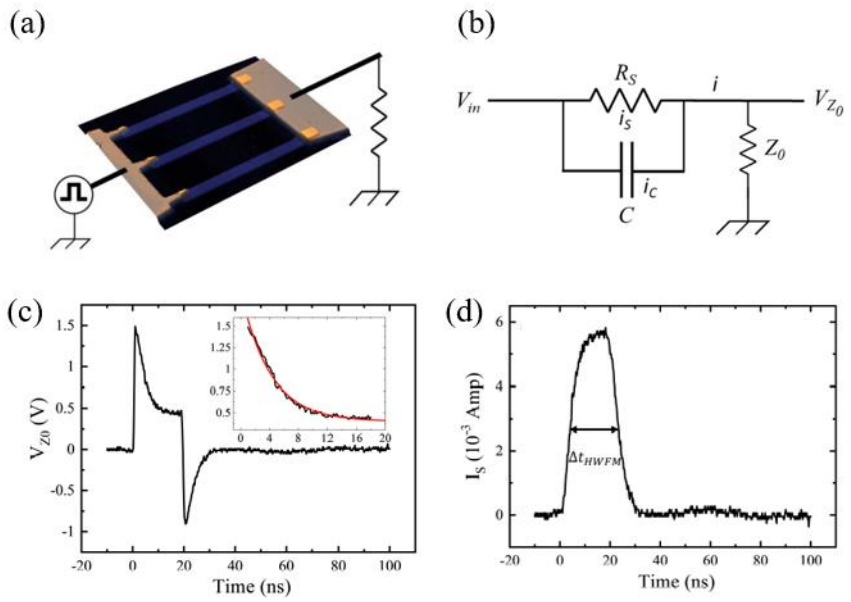

Figure 6.7: (a) Schematic of the setup for current induced motion experiment with the AFM image of three 1 μm wide nanotracks (blue) with Ti/Au contacts (light brown) microfabricated on sample S1 (t_{CoFeB}: 1.5 nm). (b) Circuit diagram of the sample considering capacitive short through the substrate. (c) Shape of the voltage pulse measured on the 50 Ω load of an oscilloscope and (d) processed current pulse flowing through the nanotracks, for a 20 ns long 2 V pulse (note that due to the impedance mismatch at the sample, 25% of the pulse is reflected before the sample and does not participate to the pulse).

The low pinning landscape of CoFeB can be understood from its structural characteristics which crystallizes into a bcc phase when annealed post deposition. It has been reported that the intrinsically amorphous CoFeB crystallizes into a bcc structure after annealing beyond 300 °C [209,217]. The presence of an amorphous phase (and subsequently crystallized bcc phase) may be expected to lead to a low-density structural defect acting as pinning sites in comparison to conventional fcc textured 3d ferromagnetic materials [187,211]. Burrows et al [217], reported that the depinning field in Ta/CoFeB/MgO films can be as low as 2–3 mT which is an order of magnitude lower than the depinning field for Co/Pt [218] or Co/Ni [217]. The mean spacing between the consecutive stable pinning sites in CoFeB is 300 nm [219]. This observed low pinning can be corroborated by the low interface roughness, low density of grain boundaries, and better structural coherence in the CoFeB films as compared to other materials hosting skyrmions [90,211].

6.6 Current induced skyrmion motion: The skyrmion dynamics were also studied via MFM at Laboratoire de Physique des Solides (LPS). Sample S1 is selected for the study of current-induced dynamics due to its lower pinning energy landscape and better control under applied magnetic fields. Figure 6.7(a) shows the schematic of the sample structure with the AFM images of the nanotracks (3 parallel tracks with width∼1.2 μm separated by∼2.8 μm from each other) along with Ti/Au contact pads. Microfabrication of the tracks and the contacts in the samples has been performed using a two-step electron beam lithography (EBL) and Ar ion etching. We deposited Ti (5nm) and Au (50nm) contact pads for transport measurements using e-beam evaporation. The current is injected in the tracks using the point-like contacts on the left and collected at the common ground. Current pulses through the sample through a 50 Ω

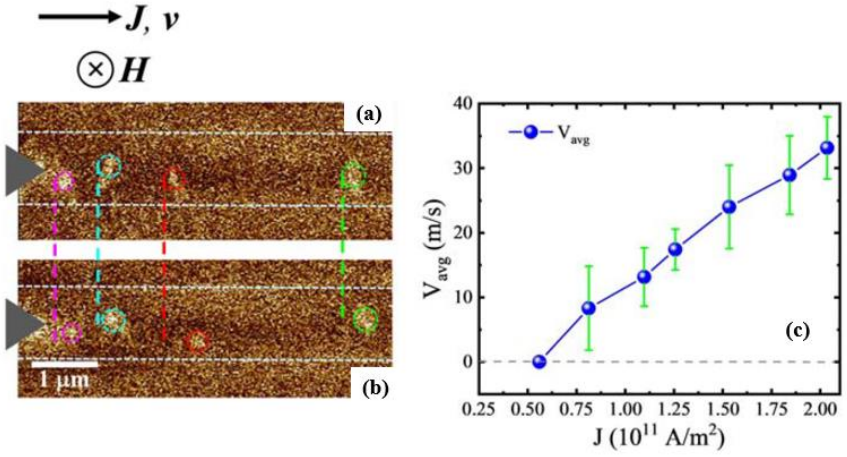

Figure 6.8: (a) and (b) show the position (by coloured circles) and displacement (by coloured lines) of the skyrmions before and after application of one current pulse. The white dashed lines indicate the boundary of a single nanotrack in the MFM image. Above these images, the arrows indicate the current *J*, velocity *v*, and applied field *H*. (c) shows the average skyrmion velocity vs current density plot. Blue lines + points are the measured average velocity. The standard deviation is shown by the green error bar.

impedance cable ended by a 50 Ω load to absorb the pulse power after transmission through the sample as shown in figure 6.7(b). The substrate used in the experiment is a Si (001) substrate with a resistivity of 0.01 Ω.cm, covered by 100 nm SiO2. The oxide layer is sufficient to isolate the tracks in DC. However, since the substrate resistance is much lower than the track resistance R_S, the current initially flows through the substrate, due to capacitive coupling between the track leads and the substrate, through the SiO_2 layer, as sketched in figure 6.7(b). The pulse measured on the 50 Ω load of an oscilloscope does not directly correspond to the current through the tracks, but to the sum of the currents through the substrate and the track. At the beginning of the pulse, the current flows directly through the capacitor and the voltage on the load is the one of the pulse. After the transient regime, the current through the capacitor is zero and the voltage on the load is $Z_0/(Z_0 + R_S)$. From the measurement in figure 6.7(c), a time constant of 4 ns and a track resistance R_S = 188Ω are deduced. The current pulse through the

sample can be deduced, as shown in figure 6.7(c). The pulse width is calculated as the full width at full maxima of the pulse, here 19 ns. The current density through the sample is subsequently calculated by dividing the current with the product of width and thickness of the nanotracks. We start from the demagnetized state and apply a small external field of 1.0 mT to stabilize the skyrmions in the tracks. Subsequently, we apply ∼19 ns current pulses with increasing amplitude. We observe that at J ∼ 0.56×10^{11}Am^{-2}, the skyrmions in the track do not move and beyond a threshold current density of ∼ 0.8×10^{11}Am^{-2}, the skyrmions start moving. The measurements for each current density are repeated in between 3-5 times depending on the number of skyrmions inside the tracks. The velocity of skyrmions is calculated by averaging the movement of these 4–7 number of skyrmions which move due to the pulses. The motion of the skyrmions, opposite to the electron motion direction, confirms the dynamics due to SOT [72,187,203]. In order to confirm that the stray field originating from the magnetic tip has minimal/no effect on the motion of the skyrmions, we have checked using no pulse applied where the skyrmions were stable. Figures 6.8(a) and (b) show the skyrmions displacements marked by different colours before and after the application of one current pulse. It should be noted that both at lower as well as at higher current densities, the displacements of all the skyrmions are not equal. This is the consequence of skyrmion hopping due to the presence of defects within the potential landscape [220]. The skyrmions advance in the track until they are either pinned or face strong skyrmion-skyrmion repulsion from another pinned skyrmion. We have plotted the average velocity of all the skyrmions present in the track for a particular current density (figure 6.8(c)). The error bar (green) in figure 6.8(c) corresponds to the standard deviation. The high current velocity data indicate, within the deviation range of the data, that a regime is reached, where defects play a minor role, analogue to a flow regime. We obtain skyrmion velocity up to∼40 ms^{-1} for a current density of∼2×10^{11}Am^{-2}. Application of higher current densities led to the burning of the contacts due to the application

Group	Authors	Sample structure	Threshould current density (A/m^2)	Velocity range (m/s)
1	Jiang et al. [72]	$Ta/CoFeB/TaO_x$	1.5×10^8	$(2.5-25) \times 10^{-6}$
	Yu et al. [221]	$Ta/CoFeB/TaO_x$	3.5×10^9	0.2 – 0.4
	Jiang et al. [73]	$Ta/CoFeB/TaO_x$	6.0×10^9	0.01 – 0.75
	Tolley et al. [222]	Ta/Pt/Co/Os/Pt/Ta	2.0×10^8	$(2.5-13) \times 10^{-6}$
2	Woo et al. [187]	$[Pt/Co/Ta]_{15}$ $[Pt/CoFeB/MgO]_{15}$	2.0×10^{11}	1– 45; 1– 100
	Legrand et al. [83]	$Ta/Co/[Pt/Ir/Co]_{10}/Pt$	2.4×10^{11}	15 – 47
	Hrabec et al. [75]	Pt/FM/Au/FM/Pt, FM=Ni/Co/Ni	2.6×10^{11}	10 – 60
	Woo et al. [87]	$Ta[Pt/CoFeB/MgO]_{20}/Ta$	1.5×10^{11}	5 – 40
	Akhter et al. [223]	Ta/Pt/CFA/MgO/Ta	1.6×10^{11}	10
	Juge et al. [224]	Ta/Pt/Co/MgO/Ta	3.5×10^{11}	15 – 100
	Litzius et al. [225]	$[Pt/CoFeB/MgO]_{15}$	3.2×10^{11}	1 – 35
	This work [226]	Ta/Pt/CoFeB/MgO/Ta	0.8×10^{11}	9 – 46

Table 6.1: Comparison of threshold current density with existing literature at room temperature. Two groups of results can be distinguished. In the first one, the measured velocities are well below 1 m/s, while in the second one, the velocities are larger than 10 m/s. In the second group, that concerns the fastest skyrmion, our work displays the smallest threshold current density.

of large (19 ns) current pulses through the tracks. The threshold current density reported in this work is lower than the ones reported in the literature (see table 6.1) whereas the corresponding velocity (>10ms^{-1}) is comparable to previous reports.

In conclusion, we have shown that skyrmions are stabilized at a very low field in Pt/CoFeB/MgO heterostructures at room temperature. We have quantified the iDMI value for our thin films which is similar to earlier reports. We observe significantly lower threshold current densities to drive the skyrmions. Larger skyrmion velocity under shorter current pulses can be expected in similar samples. Here, we have used a single set of optimized deposition conditions (growth pressure, deposition rate, and annealing temperature) to prepare the samples. However, the impact of various deposition conditions on pinning potential can be investigated in the future. We believe that the work presented here may be helpful to utilize such low-pinning materials for skyrmionic applications at low power consumption.

Chapter 7

Field induced evolution of domain structures in Ta/[Pt/Co/Ru]$_7$/Pt thin film:

To use skyrmion in a memory device, the thermal stability of it is very much essential otherwise the information may be lost in a skyrmion-based storage device [7,8]. Thus, the thermal fluctuations and stability are one more challenge in the field of skyrmions in thin film. Changing the temperature affects the iDMI, PMA, and exchange constant which play a pivotal role in destabilizing the skyrmions. Rozsa et al. demonstrated the temperature dependence of iDMI via green function formalism and it behaves similarly to the Heisenberg constant [227]. Recently, it has also been observed that the skyrmion density can be increased by increasing the temperature [228]. Although, for practical integration, the skyrmions should be stable at room temperature. The thermal stability of domain structures could be enhanced greatly by increasing the magnetic volume. Recently, Moreau-Luchaire et al., showed that increasing the HM/FM repetitions can increase the thermal stability of skyrmions as the magnetic volume enhances [85]. Another way to enhance the thermal stability of skyrmions is by using symmetric (HM1/FM/HM2/FM/HM1) superposition of FM layers [75]. In the previous chapter, we have seen that the skyrmions are easily perturbed in a single-layer FM thin film via the stray field of low moment tips which is not the case in repetitive layers due to higher dipolar energy [226]. Also, single-layer FM thin films typically have a narrow range of desired parameters for stabilizing skyrmions. However, increasing the repetition can enhance the dipolar coupling in the stack which favours the achiral Bloch wall [229]. As DMI energy

induces a fixed chirality in DWs and plays a pivotal role in stabilizing skyrmion [72,77,78], a fine-tuning of DMI and dipolar interaction is very much essential to stabilize a skyrmion in such repetitive layers.

In this context, we have prepared Ta/[Pt/Co/Ru]$_7$/Pt thin film having perpendicular magnetic anisotropy (PMA). We have studied the domain transformation as a function of the field in the thin film. Also, the chirality of the DWs has been explored. To mimic the experimental results, MuMax3 simulations have been performed.

5.1 Sample details:

We have deposited Ta(5 nm)/Pt(5 nm)/[Pt (1 nm)/Co (0.95 nm)/Ru (1.4 nm)]$_7$/Pt(4 nm) on a 100 nm thick thermally oxidized Si substrate. A schematic representation of the samples is shown in figure 7.1 (a). DC magnetron sputtering has been used to deposit the Ta, Pt, Ru and Co layers. The deposition rates of Ta, Pt, Ru and Co were 0.13, 0.3, 0.1 and 0.1 Å/s, respectively. Here, a Ta seed is deposited to grow Pt in (111) direction which helps to induce the perpendicular magnetic anisotropy. The base pressure of the chamber was ~ 8 × 10 $^{-8}$ mbar. The substrate table has been rotated at 10 rpm during the deposition to achieve uniform layers.

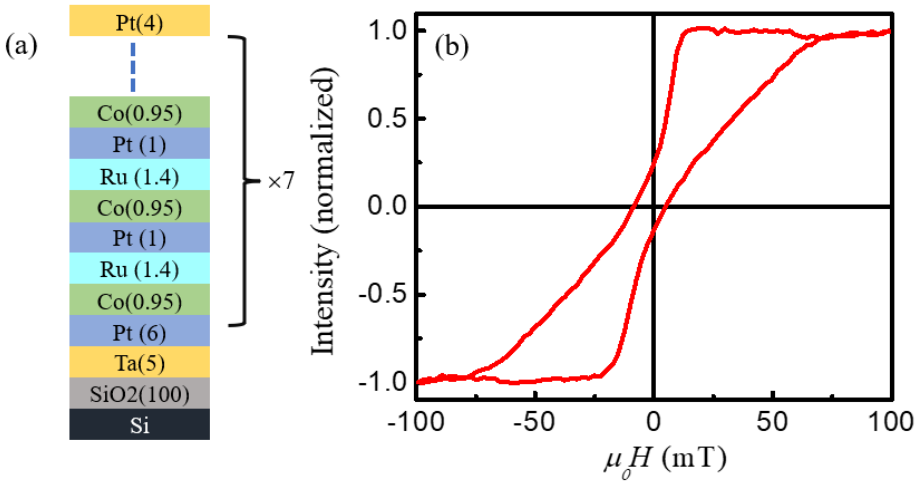

Figure 7.1: (a) Schematic of sample structure. (b) Polar-MOKE hysteresis loop of the sample.

5.2 Magnetic measurements:

5.2.1 Magnetic reversal: We have measured the hysteresis loops via polar-MOKE (as shown in figure 7.1(b)) and confirmed the easy axis along the out-of-plane direction. The low remanence and slanted hysteresis loop indicate the existence of spin textures in the sample. The saturation magnetization (M_s) and in-plane saturation field (H_s) have been quantified via SQUID magnetometry. The out-of-plane M-H loop is shown in figure 7.3 (b). The M_s and H_s are found to be 1.52 $\times 10^6$ A/m and 670 mT, respectively. The effective anisotropy of the sample is quantified using the relation, $K_{eff} = (1/2)\, H_s\, M_s$ and its value is 0.51 MJ/m^3.

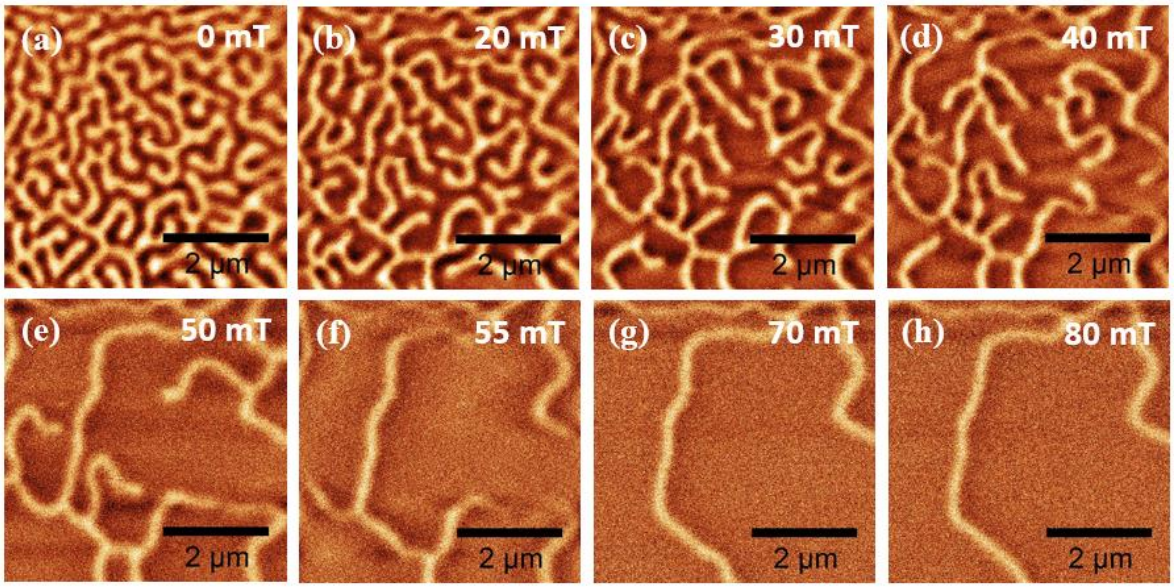

Figure 7.2: (a)-(h) Field evolution of the domain structure. A worm-like phase (a) changes to a thread-like domain at a higher field (g-h).

5.2.3 Magnetic force microscopy: To get an idea about the domain structure we have performed MFM measurements via an Attocube (Attodry 2100) AFM/MFM at NISER using commercially purchased MFM tips (Nanosensor-SSS-MFMR). All the measurements are performed at room temperature. Figure 7.2 (a-h) shows the field-evolution of the domain structures. At a demagnetized state (i.e. at H_z= 0 mT), a worm-like domain is observed, as

shown in figure 7.2(a). Further, increasing the field the density of the domain decreases and the worm-like phase transforms into a thread-like domain phase instead of skyrmions at $H_z \geq 70$ mT (figure 7.2(g-h)). For $H_z > 80$ mT, the magnetization aligned along the field direction and a saturated FM ground is achieved. As, in the sample, a repetition of [Pt/Co/Ru] is used, the dipolar energy may dominate than the DMI interaction which may prevent the formation of skyrmions in the sample. Later, we verified this hypothesis via micro-magnetic simulations.

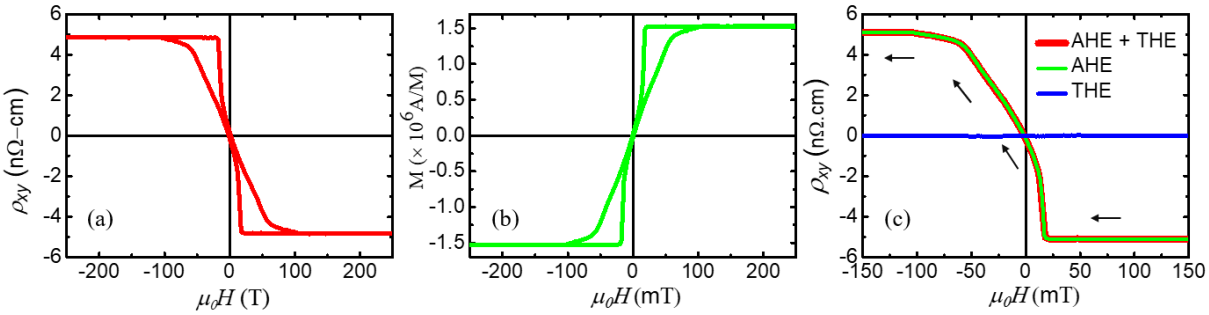

Figure 7.3: Total Hall resistivity (a) and magnetization (b) as a function of field. (c) Plot of different components of Hall resistivity *vs* field. The flat blue line indicates no signature of THE. The black arrow sign represents the field sweep direction.

5.3 Topological Hall effect: The chiral DWs induce a non-zero scaler spin chirality ($\chi_{ijk} \sim S_i \cdot (S_j \times S_k) \neq 0$) which leads to THE in the system [200,230,231]. Thus, to get an idea about the chirality of the DWs we have performed THE measurement via PPMS. The measurements are performed via five probe geometry as explained in chapter 2. The applied field is swept within ± 3T and an AC current of current density ~ 10^6 A/m^2 is used during the measurements. As explained in Chapter 5, the total Hall resistivity can be written as a sum of ordinary, anomalous, and topological Hall resistivity [191,193,200],

$$\rho_{xy} = \rho_{OHE} + \rho_{AHE} + \rho_{THE} = R_0 H + R_s M(H) + \rho_{THE} \qquad (7.1)$$

where R_0 and R_s are the ordinary and anomalous Hall coefficients and $M(H)$ is the out-of-plane magnetization as a function of the applied field (H). The total Hall resistivity (ρ_{xy}) and magnetization (M) as a function of the field is shown in figure 7.3(a) and (b), respectively. At high field, ρ_{AHE} becomes saturated and ρ_{THE} is zero. Thus, correcting the slop at a higher field (> 1.5 T) the ordinary Hall contribution has been eliminated. Therefore, only anomalous, and topological parts remain in the resistivity. Again, multiplying $R_s = \frac{\rho_{xy,saturation}}{M_s}$ with the magnetization of the sample, the ρ_{AHE} has been determined. The $\rho_{AHE+THE}$ and ρ_{AHE} are shown in the figure 7.3 (c). Now, after subtracting ρ_{AHE} from $\rho_{AHE+THE}$, we have not observed any peak in ρ_{THE} i.e. ρ_{THE} =0 for the sample (blue line in figure 7.3(c)). So, it can be concluded that the DWs are achiral in nature.

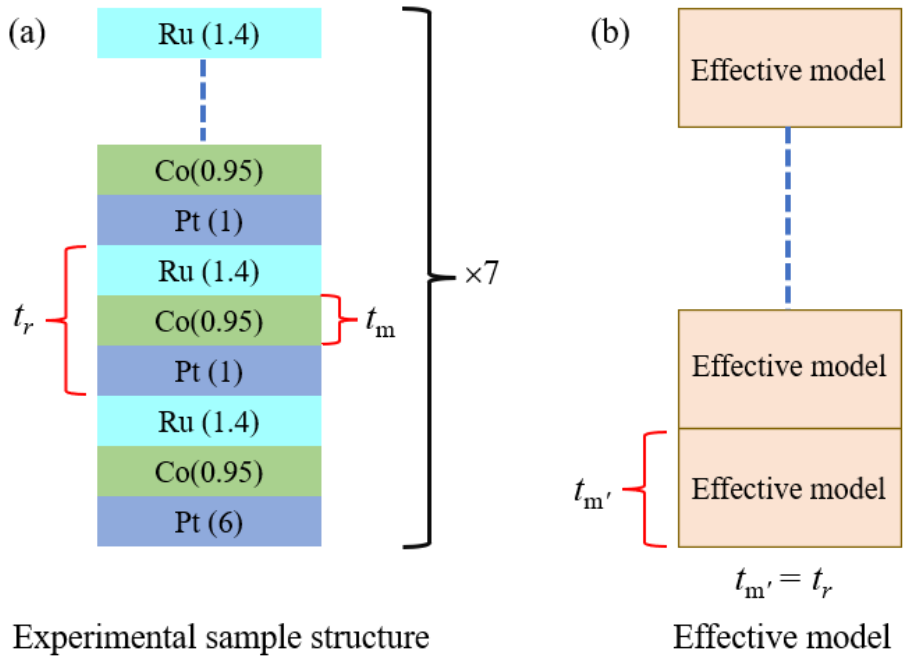

Figure 7.4: Sample stack (a) experimentally prepared, and (b) considered in the simulation. Here, t_m is the thickness (0.95 nm) of the single FM layer, whereas t_r is the thickness of one repetition of the Pt (1.0nm)/Co (0.95nm)/Ru (1.4 nm) layer. This t_r is considered as the thickness of the effective FM layer (t_m') in the simulation.

5.4 Micromagnetic simulation: We have performed micromagnetic simulations to mimic the hysteresis loops and domain images via MuMax3 [197,198]. As the sample consists of repetitive layers, we have considered an effective model to perform the simulation. Here, t_m and t_r are the magnetic layer thickness and the repetitive layer thickness, respectively. So, t_m= t_{Co}= 0.95 nm and $t_r = t_{Pt} + t_{Co} + t_{Ru}$ = 1+0.95+1.4=3.35 nm. In the effective model, the effective

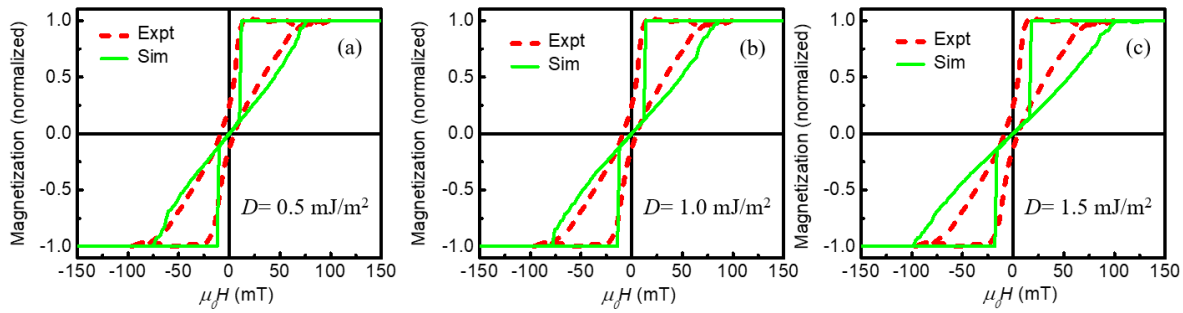

Figure 7.5: Red-coloured (dotted) hysteresis loops are p-MOKE hysteresis loops. The green-colored loops are simulated hysteresis loops for D= 0.5 mJ/m^2 (a), 1.0 mJ/m^2 (b), 1.5 mJ/m^2 (c).

FM thickness ($t_{m'}$) is considered to be the same as t_r, to achieve a homogeneously magnetic medium for the simulation. The values of M_s and K_{eff} are taken from the experiment. The exchange constant, A = 25 pJ/m has been considered in the simulation. To achieve a realistic configuration, the simulation region was split into grains of size 10 nm using random Vorronoi tessellation. The periodic boundary conditions (PBC) have been used in the simulations along the x and y axes. To minimize the total energy of the system at every step, a built-in function minimize () is used. Using a relax () function, the initial relaxed state is obtained by considering the initial magnetization in the out-of-plane direction. Woo et al., have shown that the effective model gives a similar response in a simulation like a 3-D model while the simulation parameters are scaled as [187],

$$\frac{M_S^{'}}{M_S} = \frac{A^{'}}{A} = \frac{K_{eff}^{'}}{K_{eff}} = \frac{D^{'}}{D} = \frac{t_m}{t_m^{'}} = \frac{t_m}{t_r} = f \qquad (7.2)$$

Further, the uniaxial anisotropy can be scaled as,

$$K_U^{'} = K_U f - \frac{\mu_0 M_S^2}{2}(f - f^2) \tag{7.3}$$

So, all the parameters are scaled according to the scaling law equations 7.2 and 7.3, and used in the effective model simulation. The simulation area was 2μm × 2μm × (7 t_r) nm and cell size was 2nm × 2nm × (7 t_r) nm. As this is an asymmetric sample structure, so iDMI value (D) is expected from this system. So, we have tuned the D value to mimic the MOKE hysteresis loop.

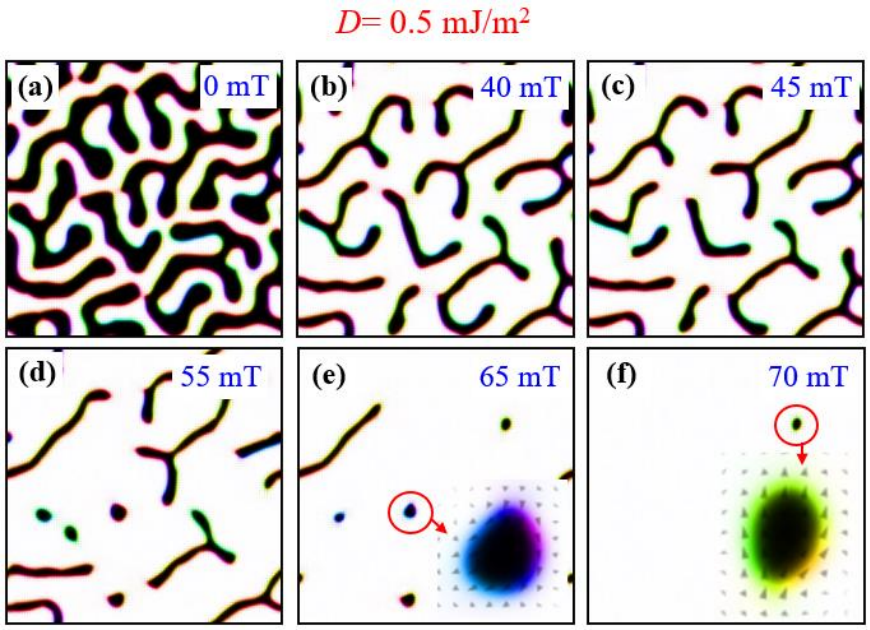

Figure 7.6: (a)-(f) reveals the field-induced simulated domain images. Worm–thread–achiral bubble domain transformation is observed as a function of field.

By comparing simulated and experimental hysteresis loops, we can predict the DMI value. However, using this method to estimate effective DMI may introduce errors in the calculated iDMI value. Consequently, while this approach may not provide an exact iDMI value, it can offer a qualitative understanding of the DMI present in the sample. In our simulation, we have considered the other parameters like M_s and K_{eff} from experiments, while varying only the DMI value to replicate hysteresis loops and domain images. Additionally, we have tried to

investigate why worm-like domains do not break into skyrmions with increasing out-of-plane field via simulations [232,233]. Thus, we have tried to match the switching and saturation field of the simulated loop with MOKE loops as the switching field mainly depends on anisotropy energy and the tails of hysteresis saturate depending upon the DMI and dipolar interactions [233]. For D=0.5 and 1 mJ/m^2, the simulated hysteresis loops match well with the experimentally observed MOKE loops, as shown in figure 7.5(a) and (b), respectively. However, for D=1.5 mJ/m^2, both the nucleation and saturation field of the simulated loops do not follow the MOKE loops (figure 7.5(c)). So, it can be concluded that the D value present in the sample is over a range of 0.5-1.0 mJ/m^2. However, the simulated domain images can give a more clear idea about the iDMI value.

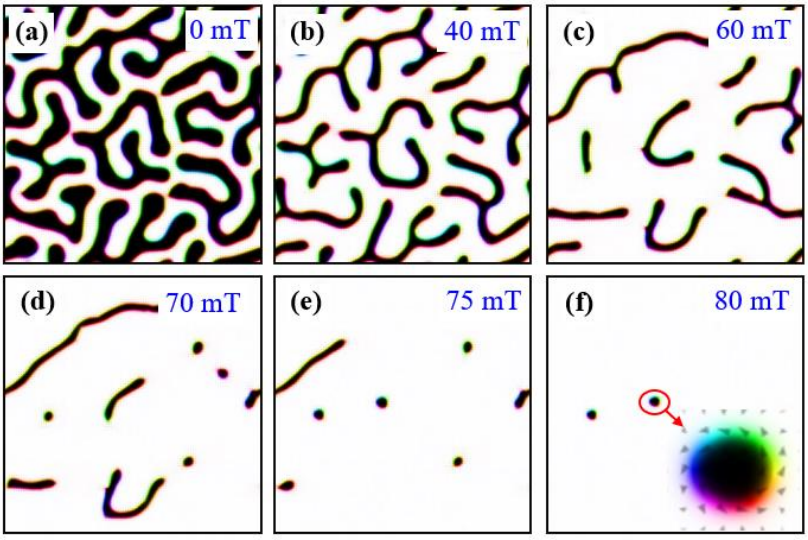

Figure 7.7: (a)-(f) reveals the field-induced simulated domain images. Worm phase–thread phase–chiral textures (mixed phase skyrmion) transformation is observed as a function of the field.

Further, we have studied the simulated domain structures with varying fields. Figure 7.6 (a-f) shows the snap-shots of domain images for D=0.5 mJ/m^2. At H_z = 0 mT, worm-like domain structures are observed (see figure 7.6(a)) which is very similar to the experiment (see figure

7.2(a)). With increasing the field worm-like phase converts to a thread-like phase (see figure 7.6 (d)) and finally to a small bubble domain (see figure 7.6 (e-f)). The inset image of figure 7.6 (e-f) clearly indicates that the domains are achiral in nature.

For D=1.0 mJ/m^2, we have also observed a worm-like phase at H_z = 0 mT (see figure 7.7(a)). With increasing the field, the worm-like phase converted into a thread-like phase (see figure 7.7 (c-d)). However, at higher fields, the thread-like phase converted to the chiral textures (mixed-phased skyrmions) (see figure 7.7 (f)). Further, pure Néel skyrmions could be observed considering the higher D value in the simulations.

Therefore, from the above discussion it has been observed that for D=0.5 mJ/m^2 the simulated hysteresis loop as well as the transformation of domain structure match well with the experiment. Also, the domains are achiral in nature as observed via THE. However, for D=1.0 mJ/m^2, the simulated hysteresis loop behaves similarly to MOKE loops but the domains are chiral in nature. So, it can be concluded that the D value is ~0.5 mJ/m^2 present in the sample and the presence of low iDMI in this sample prevents the skyrmion formation.

In summary, to enhance the thermal stability of skyrmions we have prepared a repetitive multilayer of [Pt/Co/Ru]$_7$ thin film. We have observed a worm-to-thread-like domain transformation with increasing the field. THE measurements confirm that the DWs achiral in nature. Further, by mimicking the hysteresis loops and simulating the domain structures, we have confirmed that the D value present in the system is ~ 0.5 mJ/m^2. The presence of such low iDMI value prevents the skyrmion formation in the sample. Further, by enhancing the iDMI value skyrmions can be stabilized in this system. Therefore, the iDMI value can be enhanced by reducing the Co thickness or by increasing the bottom Pt thickness in the system.

Chapter 8

Summary and conclusion:

Perpendicular magnetic anisotropic (PMA) thin films have been immensely investigated experimentally as well as theoretically in the field of spintronics and magnetism due to their higher thermal stability, narrow domain width, and higher storage capacity. Recently, it has been predicted that domain wall (DW) and skyrmion based racetrack memory in PMA based system can be used in future storage technology. Further, DW and skyrmion have proven potential applications in logic devices, transistor-like devices, neuromorphic computing, etc. Thus, the focus of the thesis work is to study the DW and skyrmion dynamics in heavy metal (HM_1)/ ferromagnet (FM)/ Oxide or HM_2. The structural symmetry of the thin films has been broken by introducing different HM or oxide on the top of the FM which allows to induce the iDMI in the system. iDMI plays a pivotal role in stabilizing the chiral spin structures in a system. Also, it has a significant impact on DW and skyrmion dynamics. In this thesis Pt is choosen as HM_1, and Re or Ru are considered as HM_2. As an oxide layer, MgO is deposited. Co or CoFeB are taken as a FM. All the thin films have been prepared using magnetron sputtering and e-beam evaporation. The nano tracks of the sample have been prepared via EBL. The structural properties i.e. crystalline quality, thickness of each layer, roughness, and surface topography have been investigated using various techniques such as XRD, XRR, and AFM. The saturation magnetization and effective anisotropy of the samples have been quantified via SQUID magnetometry. The field-dependent hysteresis loops and the corresponding domain images have been measured via MOKE microscopy. The symmetric and asymmetric DW

motion has been studied via a pulsed magnetic field in combination with the Kerr microscope. The skyrmion imaging and its dynamics have been investigated via MFM. The topological Hall resistivity has been quantified via PPMS. Further, the iDMI constant has been determined via BLS technique. In addition, mumax3 software is used to perform micromagnetic simulations in order to better understand the experimental results.

Due to the presence of less pinning sites and low Gilbert damping, CoFeB is a very promising FM alloy in the field of spintronics. So, we have studied a Ta/Pt/CoFeB (1.2 nm)/MgO/Ta thin film on a 100 nm thermally oxidized Si substrate. The easy axis of the sample along the out-of-plane direction has been confirmed from the square-shaped hysteresis loop. The DW motion of the sample increases with applied the field. When the field increases from zero, near the depinning field (H_d), the DW velocity is found to be higher than the expected creep law. This phenomenon is known as "excess velocity" which is explained by a modified creep law. In this modified creep law, a dimensionless and material-dependent parameter p is introduced whose boundary limit should be less than 1. This boundary limit of p allows us to predict the range of depinning parameters i.e. H_d, depinning temperature, and velocity at H_d. The H_d is found to be over a range of 16-19 mT for the CoFeB-based thin film which is much lower than a Co-based thin film. Further, the iDMI constant is quantified to be 0.39 ± 0.03 mJ/m^2. Our results indicate the importance of low pinning in the ferromagnetic film in the field of spintronics.

The Pt/CoFeB interface introduces a low DMI interaction in the thin films. However, higher DMI can stabilize smaller size chiral textures in thin films which is very useful from the practical application point of view. It has been predicted that Re/Co interface can induce a huge iDMI in a system. In this context, in the 4th chapter, we have shown our results about the effect of Re insertion on DW dynamics in Ta/Pt/Co/Re (t_{Re})/Ta thin films. The DW velocity is enhanced in the thin films with Re thickness (t_{Re}). This enhancement can be corroborated with

the reduction in effective anisotropy and pinning potentials. Further, it has been observed that iDMI value increases from 1.10 to 1.78 mJ/m^2 after the insertion of Re and Re/Co interface gives iDMI ~0.7 mJ/m^2. This increment in DMI interaction also plays a key role in faster DW motion. An asymmetry in the left (v_L) and right (v_L) sides of DW velocity (as a function in-plane field, H_x) w.r.t the minima of velocity arise might be due to a combined effect of the chiral damping and DW stiffness. Also, the chiral damping may depend on the out-of-plane field (H_z) and consequently, it changes the behaviour of DW dynamics.

As inserting a Re layer in between Co and Ta layers in Pt/Co/Ta system enhances the iDMI, hence, the skyrmion has been stabilized in Pt/Co/Ta and Pt/Co/Re systems tuning the thickness of Co layers near to spin reorientation transition in the systems. Further, THE confirms the chiral natures of the observed textures, and different behaviour in topological Hall resistivity is observed for the Pt/Co/Ta and Pt/Co/Re. Mumax simulations confirm that the effective anisotropy (k_{eff}) and DMI interaction play a pivotal role in determining the topological Hall behaviour in a system. Additionally, by simulating the hysteresis loops we predicted that the iDMI for Pt/Co/Ta and Pt/Co/Re systems might be ~1.0 and ~1.2 mJ/m^2, respectively.

Further, we have studied skyrmion dynamics in another popular ferromagnetic system i.e. CoFeB. As seen, the CoFeB-based system exhibits low pinning energy in comparison to polycrystalline FM layers (viz., Co, Fe, etc.), so we have also stabilized the skyrmion in Pt/CoFeB/MgO heterostructures at a very low field and room temperature. The iDMI value of the thin films is found to be 0.33 ± 0.03 mJ/m^2 which is similar to earlier reports. Further, we have studied the current induced dynamics of the skyrmion through a nanotrack. We observe significantly lower threshold current densities to drive the skyrmions than the earlier reports. The work presented here may assist in utilizing such low-pinning materials at low power consumption for skyrmionic applications in the future.

Thermal fluctuations and stability are another issue in using the skyrmions for practical integration. Thus, to enhance the thermal stability of skyrmions we have prepared a repetitive multilayer of $[Pt/Co/Ru]_7$ thin film. The worm-like domain phase is observed at a demagnetizing state. At higher fields, the worm-like domain converted to a thread-like domain instead of skyrmion. The DWs are achiral in nature in this case. By mimicking the hysteresis loop via MuMax3 with the MOKE loop, an iDMI value of ~0.5mJ/m^2 has been determined. Such a low DMI in the stacks restricts the skyrmion formation. It has been found that by enhancing the iDMI value, skyrmion can be stabilized in the system.

Future Outlook:

In this thesis work, we have studied the statics and dynamics of DWs and skyrmion in Pt/CoFeB and Pt/Co thin film. During the course of our study, we have identified several open questions that need to be addressed in the future, as outlined below.

i. As, so far, the excess velocity is only observed in Pt/Co, Pt/Co/Ni, and Pt/CoFeB systems, more work is needed in different systems to determine if this modified creep law explains excess velocity in ferromagnetic systems universally.

ii. Like the Pt/CoFeB system, skyrmion dynamics can be studied in Pt/Co/Re system, as it shows a high and additive iDMI.

iii. The influence of different deposition conditions on the pinning potential as well in skyrmion dynamics can be investigated.

iv. A multilayer of $[Pt/Co/Ru]_N$ thin film with a bit higher thickness of Pt can be prepared to study the statics and dynamic properties of skyrmion. The skyrmion density, topological Hall resistivity, and skyrmion motion can be studied with the repetition number (N).

v. As CoFeB thin film shows low pinning potential and Co/Re gives a sizeable iDMI, so skyrmions dynamics can be studied in a $[Pt/CoFeB/Re]_N$ stack.

References:

[1] N. A. Siberman and A. A. Bauer, *The Oxford Companion to Archaeology*.

[2] S. N. Piramanayagam, *Perpendicular Recording Media for Hard Disk Drives*, J Appl Phys **102**, (2007).

[3] B. Tudu and A. Tiwari, *Recent Developments in Perpendicular Magnetic Anisotropy Thin Films for Data Storage Applications*, Vacuum **146**, 329 (2017).

[4] C. P. Bean and undJ D. Livingston, *Superparamagnetism*, J Appl Phys **30**, S120 (1959).

[5] D. Kumar, T. Jin, R. Sbiaa, M. Kläui, S. Bedanta, S. Fukami, D. Ravelosona, S.-H. Yang, X. Liu, and S. N. Piramanayagam, *Domain Wall Memory: Physics, Materials, and Devices*, Phys Rep **958**, 1 (2022).

[6] S. Parkin and S.-H. Yang, *Memory on the Racetrack*, Nat Nanotechnol **10**, 195 (2015).

[7] A. Fert, N. Reyren, and V. Cros, *Magnetic Skyrmions: Advances in Physics and Potential Applications*, Nat Rev Mater **2**, 17031 (2017).

[8] K. Everschor-Sitte, J. Masell, R. M. Reeve, and M. Kläui, *Perspective: Magnetic Skyrmions—Overview of Recent Progress in an Active Research Field*, J Appl Phys **124**, (2018).

[9] R. Tomasello, E. Martinez, R. Zivieri, L. Torres, M. Carpentieri, and G. Finocchio, *A Strategy for the Design of Skyrmion Racetrack Memories*, Sci Rep **4**, 6784 (2014).

[10] S. S. P. Parkin, M. Hayashi, and L. Thomas, *Magnetic Domain-Wall Racetrack Memory*, Science (1979) **320**, 190 (2008).

[11] D. A. Allwood, G. Xiong, C. C. Faulkner, D. Atkinson, D. Petit, and R. P. Cowburn, *Magnetic Domain-Wall Logic*, Science (1979) **309**, 1688 (2005).

[12] N. Locatelli, V. Cros, and J. Grollier, *Spin-Torque Building Blocks*, Nat Mater **13**, 11 (2014).

[13] M. Sharad, C. Augustine, G. Panagopoulos, and K. Roy, *Spin-Based Neuron Model with Domain-Wall Magnets as Synapse*, IEEE Trans Nanotechnol **11**, 843 (2012).

[14] S. Luo and L. You, *Skyrmion Devices for Memory and Logic Applications*, APL Mater **9**, (2021).

[15] S. Li, W. Kang, Y. Huang, X. Zhang, Y. Zhou, and W. Zhao, *Magnetic Skyrmion-Based Artificial Neuron Device*, Nanotechnology **28**, 31LT01 (2017).

[16] F. J. A. Den Broeder, W. Hoving, and P. J. H. Bloemen, *Magnetic Anisotropy of Multilayers*, J Magn Magn Mater **93**, 562 (1991).

[17] P. F. Carcia, *Perpendicular Magnetic Anisotropy in Pd/Co and Pt/Co Thin-Film Layered Structures*, J Appl Phys **63**, 5066 (1988).

[18] R. Sbiaa, H. Meng, and S. N. Piramanayagam, *Materials with Perpendicular Magnetic Anisotropy for Magnetic Random Access Memory*, Physica Status Solidi (RRL)–Rapid Research Letters **5**, 413 (2011).

[19] H. Meng, R. Sbiaa, S. Y. H. Lua, C. C. Wang, M. A. K. Akhtar, S. K. Wong, P. Luo, C. J. P. Carlberg, and K. S. A. Ang, *Low Current Density Induced Spin-Transfer Torque Switching in CoFeB–MgO Magnetic Tunnel Junctions with Perpendicular Anisotropy*, J Phys D Appl Phys **44**, 405001 (2011).

[20] A.-C. Sun, J.-H. Hsu, P. C. Kuo, H. L. Huang, H. C. Lu, and S. F. Wang, *Thickness Limit in Perpendicular Magnetic Anisotropy L10 FePt (0 0 1) Thin Film*, J Magn Magn Mater **310**, 2650 (2007).

[21] S. Esho, *Perpendicular Magnetic Anisotropy in Sputtered GdCo Films*, J Appl Phys **50**, 1006 (1979).

[22] M. Kisielewski, A. Maziewski, T. Polyakova, and V. Zablotskii, *Wide-Scale Evolution of Magnetization Distribution in Ultrathin Films*, Phys Rev B **69**, 184419 (2004).

[23] J. Choi, J. Wu, C. Won, Y. Z. Wu, A. Scholl, A. Doran, T. Owens, and Z. Q. Qiu, *Magnetic Bubble Domain Phase at the Spin Reorientation Transition of Ultrathin Fe/Ni/Cu (001) Film*, Phys Rev Lett **98**, 207205 (2007).

[24] M. He et al., *Evolution of Topological Skyrmions across the Spin Reorientation Transition in Pt/Co/Ta Multilayers*, Phys Rev B **97**, 174419 (2018).

[25] S. Blundell, *Magnetism in Condensed Matter* (OUP Oxford, 2001).

[26] M. Getzlaff, *Fundamentals of Magnetism* (Springer Science & Business Media, 2007).

[27] M. T. Johnson, P. J. H. Bloemen, F. J. A. Den Broeder, and J. J. De Vries, *Magnetic Anisotropy in Metallic Multilayers*, Reports on Progress in Physics **59**, 1409 (1996).

[28] B. D. Cullity and C. D. Graham, *Introduction to Magnetic Materials* (John Wiley & Sons, 2011).

[29] J. Mathon, D. M. Edwards, R. B. Muniz, and M. S. Phan, *Theory of Oscillatory Exchange Coupling in Magnetic Multilayers*, J Magn Magn Mater **104**, 1721 (1992).

[30] S. S. P. Parkin, N. More, and K. P. Roche, *Oscillations in Exchange Coupling and Magnetoresistance in Metallic Superlattice Structures: Co/Ru, Co/Cr, and Fe/Cr*, Phys Rev Lett **64**, 2304 (1990).

[31] eg P. Bruno and C. Chappert, *Oscillatory Coupling between Ferromagnetic Layers Separated by a Nonmagnetic Metal Spacer*, Phys Rev Lett **67**, 1602 (1991).

[32] M. Getzlaff, *Fundamentals of Magnetism* (Springer Science & Business Media, 2007).

[33] I. Dzyaloshinsky, *A Thermodynamic Theory of "Weak" Ferromagnetism of Antiferromagnetics*, Journal of Physics and Chemistry of Solids **4**, 241 (1958).

[34] T. Moriya, *Anisotropic Superexchange Interaction and Weak Ferromagnetism*, Phys. Rev. **120**, 91 (1960).

[35] A. Fert and P. M. Levy, *Role of Anisotropic Exchange Interactions in Determining the Properties of Spin-Glasses*, Phys. Rev. Lett. **44**, 1538 (1980).

[36] Weiss Pierre, *L'hypothèse Du Champ Moléculaire et La Propriété Ferromagnétique*, J. Phys. Theor. Appl. **6**, 661 (1907).

[37] L. D. Landau and E. Lifshitz, *On the Theory of the Dispersion of Magnetic permeability in Ferromagnetic Bodies*, Phys. Z. Sowjet. **8**, 153 (1935).

[38] A. Hubert, R. Schäfer, A. Hubert, and R. Schäfer, *Domain Theory*, Magnetic Domains: The Analysis of Magnetic Microstructures 99 (1998).

[39] F. Bloch, *Zur Theorie Des Austauschproblems Und Der Remanenzerscheinung Der Ferromagnetika*, Zeitschrift Für Physik **74**, 295 (1932).

[40] M. Heide, G. Bihlmayer, and S. Blügel, *Dzyaloshinskii-Moriya Interaction Accounting for the Orientation of Magnetic Domains in Ultrathin Films: Fe/W (110)*, Phys Rev B **78**, 140403 (2008).

[41] T. L. Gilbert, *A Phenomenological Theory of Damping in Ferromagnetic Materials*, IEEE Trans Magn **40**, 3443 (2004).

[42] P. J. Metaxas, J. P. Jamet, A. Mougin, M. Cormier, J. Ferré, V. Baltz, B. Rodmacq, B. Dieny, and R. L. Stamps, *Creep and Flow Regimes of Magnetic Domain-Wall Motion in Ultrathin Pt/Co/Pt Films with Perpendicular Anisotropy*, Phys Rev Lett **99**, 217208 (2007).

[43] V. Jeudy, R. D. Pardo, W. S. Torres, S. Bustingorry, and A. B. Kolton, *Pinning of Domain Walls in Thin Ferromagnetic Films*, Phys Rev B **98**, 54406 (2018).

[44] S. Lemerle, J. Ferré, C. Chappert, V. Mathet, T. Giamarchi, and P. Le Doussal, *Domain Wall Creep in an Ising Ultrathin Magnetic Film*, Phys Rev Lett **80**, 849 (1998).

[45] K. J. A. Franke, B. de Wiele, Y. Shirahata, S. J. Hämäläinen, T. Taniyama, and S. van Dijken, *Reversible Electric-Field-Driven Magnetic Domain-Wall Motion*, Phys Rev X **5**, 11010 (2015).

[46] P. Chureemart, R. F. L. Evans, and R. W. Chantrell, *Dynamics of Domain Wall Driven by Spin-Transfer Torque*, Phys Rev B **83**, 184416 (2011).

[47] Z. Li and S. Zhang, *Domain-Wall Dynamics Driven by Adiabatic Spin-Transfer Torques*, Phys Rev B **70**, 24417 (2004).

[48] P. Gambardella and I. M. Miron, *Current-Induced Spin–Orbit Torques*, Philosophical Transactions of the Royal Society A: Mathematical, Physical and Engineering Sciences **369**, 3175 (2011).

[49] N. L. Schryer and L. R. Walker, *The Motion of 180 Domain Walls in Uniform Dc Magnetic Fields*, J Appl Phys **45**, 5406 (1974).

[50] A. Mougin, M. Cormier, J. P. Adam, P. J. Metaxas, and J. Ferré, *Domain Wall Mobility, Stability and Walker Breakdown in Magnetic Nanowires*, Europhys Lett **78**, 57007 (2007).

[51] D. A. Huse, C. L. Henley, and D. S. Fisher, *Huse, Henley, and Fisher Respond*, Phys Rev Lett **55**, 2924 (1985).

[52] D. A. Huse and C. L. Henley, *Pinning and Roughening of Domain Walls in Ising Systems Due to Random Impurities*, Phys Rev Lett **54**, 2708 (1985).

[53] D. S. Fisher, *Interface Fluctuations in Disordered Systems: 5- Expansion and Failure of Dimensional Reduction*, Phys Rev Lett **56**, 1964 (1986).

[54] M. Kardar, G. Parisi, and Y.-C. Zhang, *Dynamic Scaling of Growing Interfaces*, Phys Rev Lett **56**, 889 (1986).

[55] G. Blatter, M. V Feigel'man, V. B. Geshkenbein, A. I. Larkin, and V. M. Vinokur, *Vortices in High-Temperature Superconductors*, Rev Mod Phys **66**, 1125 (1994).

[56] V. Jeudy, A. Mougin, S. Bustingorry, W. S. Torres, J. Gorchon, A. B. Kolton, A. Lema\^\itre, and J.-P. Jamet, *Universal Pinning Energy Barrier for Driven Domain Walls in Thin Ferromagnetic Films*, Phys Rev Lett **117**, 57201 (2016).

[57] M. V Feigel'Man, V. B. Geshkenbein, A. I. Larkin, and V. M. Vinokur, *Theory of Collective Flux Creep*, Phys Rev Lett **63**, 2303 (1989).

[58] T. Nattermann, *Scaling Approach to Pinning: Charge Density Waves and Giant Flux Creep in Superconductors*, Phys Rev Lett **64**, 2454 (1990).

[59] P. Chauve, T. Giamarchi, and P. Le Doussal, *Creep and Depinning in Disordered Media*, Phys Rev B **62**, 6241 (2000).

[60] N. B. Caballero et al., *Excess Velocity of Magnetic Domain Walls Close to the Depinning Field*, Phys Rev B **96**, 224422 (2017).

[61] R. D. Pardo, N. Moisan, L. J. Albornoz, A. Lema\^\itre, J. Curiale, and V. Jeudy, *Common Universal Behavior of Magnetic Domain Walls Driven by Spin-Polarized Electrical Current and Magnetic Field*, Phys Rev B **100**, 184420 (2019).

[62] S. Bustingorry, A. B. Kolton, and T. Giamarchi, *Thermal Rounding of the Depinning Transition*, Europhys Lett **81**, 26005 (2007).

[63] R. D. Pardo, W. S. Torres, A. B. Kolton, S. Bustingorry, and V. Jeudy, *Universal Depinning Transition of Domain Walls in Ultrathin Ferromagnets*, Phys Rev B **95**, 184434 (2017).

[64] G. Chen, T. Ma, A. T. N'Diaye, H. Kwon, C. Won, Y. Wu, and A. K. Schmid, *Tailoring the Chirality of Magnetic Domain Walls by Interface Engineering*, Nat Commun **4**, 2671 (2013).

[65] G. Chen et al., *Novel Chiral Magnetic Domain Wall Structure in Fe/Ni/Cu (001) Films*, Phys Rev Lett **110**, 177204 (2013).

[66] S.-G. Je, D.-H. Kim, S.-C. Yoo, B.-C. Min, K.-J. Lee, and S.-B. Choe, *Asymmetric Magnetic Domain-Wall Motion by the Dzyaloshinskii-Moriya Interaction*, Phys Rev B **88**, 214401 (2013).

[67] A. Hrabec, N. A. Porter, A. Wells, M. J. Benitez, G. Burnell, S. McVitie, D. McGrouther, T. A. Moore, and C. H. Marrows, *Measuring and Tailoring the Dzyaloshinskii-Moriya Interaction in Perpendicularly Magnetized Thin Films*, Phys Rev B **90**, 20402 (2014).

[68] T. H. R. Skyrme, *A Unified Field Theory of Mesons and Baryons*, Nuclear Physics **31**, 556 (1962).

[69] A. N. Bogdanov and U. K. Rößler, *Chiral Symmetry Breaking in Magnetic Thin Films and Multilayers*, Phys Rev Lett **87**, 37203 (2001).

[70] A. Bogdanov and A. Hubert, *The Stability of Vortex-like Structures in Uniaxial Ferromagnets*, J Magn Magn Mater **195**, 182 (1999).

[71] S. Mühlbauer, B. Binz, F. Jonietz, C. Pfleiderer, A. Rosch, A. Neubauer, R. Georgii, and P. Böni, *Skyrmion Lattice in a Chiral Magnet*, Science (1979) **323**, 915 (2009).

[72] W. Jiang et al., *Blowing Magnetic Skyrmion Bubbles*, Science (1979) **349**, 283 (2015).

[73] W. Jiang et al., *Direct Observation of the Skyrmion Hall Effect*, Nat Phys **13**, 162 (2017).

[74] A. Soumyanarayanan et al., *Tunable Room-Temperature Magnetic Skyrmions in Ir/Fe/Co/Pt Multilayers*, Nat Mater **16**, 898 (2017).

[75] A. Hrabec, J. Sampaio, M. Belmeguenai, I. Gross, R. Weil, S. M. Chérif, A. Stashkevich, V. Jacques, A. Thiaville, and S. Rohart, *Current-Induced Skyrmion Generation and Dynamics in Symmetric Bilayers*, Nat Commun **8**, 15765 (2017).

[76] G. P. Müller, M. Hoffmann, C. Dißelkamp, D. Schürhoff, S. Mavros, M. Sallermann, N. S. Kiselev, H. Jónsson, and S. Blügel, *Spirit: Multifunctional Framework for Atomistic Spin Simulations*, Phys Rev B **99**, 224414 (2019).

[77] S. Rohart and A. Thiaville, *Skyrmion Confinement in Ultrathin Film Nanostructures in the Presence of Dzyaloshinskii-Moriya Interaction*, Phys Rev B **88**, 184422 (2013).

[78] A. Thiaville, S. Rohart, É. Jué, V. Cros, and A. Fert, *Dynamics of Dzyaloshinskii Domain Walls in Ultrathin Magnetic Films*, EPL (Europhysics Letters) **100**, 57002 (2012).

[79] N. Nagaosa and Y. Tokura, *Topological Properties and Dynamics of Magnetic Skyrmions*, Nat Nanotechnol **8**, 899 (2013).

[80] W. Legrand, Crafting Magnetic Skyrmions at Room Temperature: Size, Stability and Dynamics in Multilayers, Université Paris Saclay (COmUE), 2019.

[81] T. Okubo, S. Chung, and H. Kawamura, *Multiple-q States and the Skyrmion Lattice of the Triangular-Lattice Heisenberg Antiferromagnet under Magnetic Fields*, Phys Rev Lett **108**, 17206 (2012).

[82] S. Heinze, K. Von Bergmann, M. Menzel, J. Brede, A. Kubetzka, R. Wiesendanger, G. Bihlmayer, and S. Blügel, *Spontaneous Atomic-Scale Magnetic Skyrmion Lattice in Two Dimensions*, Nat Phys **7**, 713 (2011).

[83] W. Legrand, D. Maccariello, N. Reyren, K. Garcia, C. Moutafis, C. Moreau-Luchaire, S. Collin, K. Bouzehouane, V. Cros, and A. Fert, *Room-Temperature Current-Induced Generation and Motion of Sub-100 Nm Skyrmions*, Nano Lett **17**, 2703 (2017).

[84] N. Romming, A. Kubetzka, C. Hanneken, K. von Bergmann, and R. Wiesendanger, *Field-Dependent Size and Shape of Single Magnetic Skyrmions*, Phys Rev Lett **114**, 177203 (2015).

[85] C. Moreau-Luchaire et al., *Additive Interfacial Chiral Interaction in Multilayers for Stabilization of Small Individual Skyrmions at Room Temperature*, Nat Nanotechnol **11**, 444 (2016).

[86] N. Romming, C. Hanneken, M. Menzel, J. E. Bickel, B. Wolter, K. von Bergmann, A. Kubetzka, and R. Wiesendanger, *Writing and Deleting Single Magnetic Skyrmions*, Science (1979) **341**, 636 (2013).

[87] S. Woo et al., *Spin-Orbit Torque-Driven Skyrmion Dynamics Revealed by Time-Resolved X-Ray Microscopy*, Nat Commun **8**, 15573 (2017).

[88] S. Emori, U. Bauer, S.-M. Ahn, E. Martinez, and G. S. D. Beach, *Current-Driven Dynamics of Chiral Ferromagnetic Domain Walls*, Nat Mater **12**, 611 (2013).

[89] G. Chen, *Skyrmion Hall Effect*, Nat Phys **13**, 112 (2017).

[90] A. Casiraghi, H. Corte-León, M. Vafaee, F. Garcia-Sanchez, G. Durin, M. Pasquale, G. Jakob, M. Kläui, and O. Kazakova, *Individual Skyrmion Manipulation by Local Magnetic Field Gradients*, Commun Phys **2**, 1 (2019).

[91] L. Liu, O. J. Lee, T. J. Gudmundsen, D. C. Ralph, and R. A. Buhrman, *Current-Induced Switching of Perpendicularly Magnetized Magnetic Layers Using Spin Torque from the Spin Hall Effect*, Phys Rev Lett **109**, 96602 (2012).

[92] L. Liu, C.-F. Pai, Y. Li, H. W. Tseng, D. C. Ralph, and R. A. Buhrman, *Spin-Torque Switching with the Giant Spin Hall Effect of Tantalum*, Science (1979) **336**, 555 (2012).

[93] C.-F. Pai, L. Liu, Y. Li, H. W. Tseng, D. C. Ralph, and R. A. Buhrman, *Spin Transfer Torque Devices Utilizing the Giant Spin Hall Effect of Tungsten*, Appl Phys Lett **101**, (2012).

[94] R. Ramaswamy, X. Qiu, T. Dutta, S. D. Pollard, and H. Yang, *Hf Thickness Dependence of Spin-Orbit Torques in Hf/CoFeB/MgO Heterostructures*, Appl Phys Lett **108**, (2016).

[95] A. A. Thiele, *Applications of the Gyrocoupling Vector and Dissipation Dyadic in the Dynamics of Magnetic Domains*, J Appl Phys **45**, 377 (1974).

[96] A. A. Thiele, *Steady-State Motion of Magnetic Domains*, Phys Rev Lett **30**, 230 (1973).

[97] X. Zhang, Y. Zhou, and M. Ezawa, *Magnetic Bilayer-Skyrmions without Skyrmion Hall Effect*, Nat Commun **7**, 10293 (2016).

[98] W. Legrand, D. Maccariello, F. Ajejas, S. Collin, A. Vecchiola, K. Bouzehouane, N. Reyren, V. Cros, and A. Fert, *Room-Temperature Stabilization of Antiferromagnetic Skyrmions in Synthetic Antiferromagnets*, Nat Mater **19**, 34 (2020).

[99] S. Woo et al., *Current-Driven Dynamics and Inhibition of the Skyrmion Hall Effect of Ferrimagnetic Skyrmions in GdFeCo Films*, Nat Commun **9**, 959 (2018).

[100] T. M. Besmann, D. P. Stinton, and R. A. Lowden, *Chemical Vapor Deposition Techniques*, MRS Bull **13**, 45 (1988).

[101] J. E. Mahan, *Physical Vapor Deposition of Thin Films* (2000).

[102] P. Sigmund, *Theory of Sputtering. I. Sputtering Yield of Amorphous and Polycrystalline Targets*, Physical Review **184**, 383 (1969).

[103] J. Musil, *Recent Advances in Magnetron Sputtering Technology*, Surf Coat Technol **100**, 280 (1998).

[104] P. J. Kelly and R. D. Arnell, *Magnetron Sputtering: A Review of Recent Developments and Applications*, Vacuum **56**, 159 (2000).

[105] D. Depla, S. Mahieu, and J. E. Greene, *Sputter Deposition Processes*, in *Handbook of Deposition Technologies for Films and Coatings* (Elsevier, 2010), pp. 253–296.

[106] K. S. Harsha, *Principles of Vapor Deposition of Thin Films* (Elsevier, 2005).

[107] D. O. Smith, M. S. Cohen, and G. P. Weiss, *Oblique-Incidence Anisotropy in Evaporated Permalloy Films*, J Appl Phys **31**, 1755 (1960).

[108] R. F. W. Pease, *Electron Beam Lithography*, Contemp Phys **22**, 265 (1981).

[109] A. A. Tseng, K. Chen, C. D. Chen, and K. J. Ma, *Electron Beam Lithography in Nanoscale Fabrication: Recent Development*, IEEE Transactions on Electronics Packaging Manufacturing **26**, 141 (2003).

[110] T. P. Russell, *X-Ray and Neutron Reflectivity for the Investigation of Polymers*, Materials Science Reports **5**, 171 (1990).

[111] E. S. Ameh, *A Review of Basic Crystallography and X-Ray Diffraction Applications*, The International Journal of Advanced Manufacturing Technology **105**, 3289 (2019).

[112] W. H. Bragg and W. L. Bragg, *The Reflection of X-Rays by Crystals*, Proceedings of the Royal Society of London. Series A, Containing Papers of a Mathematical and Physical Character **88**, 428 (1913).

[113] M. A. Omar, *Elementary Solid State Physics: Principles and Applications* (Pearson Education India, 1975).

[114] *SmartLab, Rigaku Corporation*, https://www.rigaku.com/products/xrd/smartlab.

[115] K. Inaba, *X-Ray Thin-Film Measurement Techniques*, The Rigaku Journal **24**, 10 (2008).

[116] *D8-Advance Reflectometer, Bruker* , https://www.bruker.com/en/products-and-solutions/diffractometers-and-x-ray-microscopes/x-ray-diffractometers/d8-advance-family.html.

[117] I. W. Hamley and J. S. Pedersen, *Analysis of Neutron and X-Ray Reflectivity Data. I. Theory*, J Appl Crystallogr **27**, 29 (1994).

[118] Y. Fujii and others, *Recent Developments in the X-Ray Reflectivity Analysis for Rough Surfaces and Interfaces of Multilayered Thin Film Materials*, J Mater **2013**, 678361 (2013).

[119] M. Björck and G. Andersson, *GenX: An Extensible X-Ray Reflectivity Refinement Program Utilizing Differential Evolution*, J Appl Crystallogr **40**, 1174 (2007).

[120] A. Glavic and M. Björck, *GenX 3: The Latest Generation of an Established Tool*, J Appl Crystallogr **55**, (2022).

[121] A. Barone, *Principles and Applications of Superconducting Quantum Interference Devices* (World Scientific, 1992).

[122] R. L. Fagaly, *Superconducting Quantum Interference Device Instruments and Applications*, Review of Scientific Instruments **77**, (2006).

[123] R. C. Jaklevic, J. Lambe, A. H. Silver, and J. E. Mercereau, *Quantum Interference Effects in Josephson Tunneling*, Phys Rev Lett **12**, 159 (1964).

[124] *SQUID Magnetometer, Quantum Design MPMS®3*, https://www.qdusa.com/products/mpms3.html.

[125] R. Schäfer, *Investigation of Domains and Dynamics of Domain Walls by the Magneto-Optical Kerr-Effect*, Handbook of Magnetism and Advanced Magnetic Materials (2007).

[126] Z. Q. Qiu and S. D. Bader, *Surface Magneto-Optic Kerr Effect*, Review of Scientific Instruments **71**, 1243 (2000).

[127] D. A. Allwood, G. Xiong, M. D. Cooke, and R. P. Cowburn, *Magneto-Optical Kerr Effect Analysis of Magnetic Nanostructures*, J Phys D Appl Phys **36**, 2175 (2003).

[128] W. Rave, R. Schäfer, and A. Hubert, *Quantitative Observation of Magnetic Domains with the Magneto-Optical Kerr Effect*, J Magn Magn Mater **65**, 7 (1987).

[129] J. Kerr, *XLIII. On Rotation of the Plane of Polarization by Reflection from the Pole of a Magnet*, The London, Edinburgh, and Dublin Philosophical Magazine and Journal of Science **3**, 321 (1877).

[130] J. Kerr, *XXIV. On Reflection of Polarized Light from the Equatorial Surface of a Magnet*, The London, Edinburgh, and Dublin Philosophical Magazine and Journal of Science **5**, 161 (1878).

[131] P. S. Pershan, *Magneto-Optical Effects*, J Appl Phys **38**, 1482 (1967).

[132] S. Sugano and N. Kojima, *Magneto-Optics*, Vol. 128 (Springer Science & Business Media, 2013).

[133] *Magneto-Optical Kerr Microscope & Magnetometer, Evico Magnetics,* https://evicomagnetics.com/productss/magneto-optical-kerr-microscope-magnetometer/.

[134] I. V Soldatov and R. Schäfer, *Selective Sensitivity in Kerr Microscopy*, Review of Scientific Instruments **88**, (2017).

[135] S. S. P. Parkin, M. Hayashi, and L. Thomas, *Magnetic Domain-Wall Racetrack Memory*, Science (1979) **320**, 190 (2008).

[136] D. A. Allwood, G. Xiong, C. C. Faulkner, D. Atkinson, D. Petit, and R. P. Cowburn, *Magnetic Domain-Wall Logic*, Science (1979) **309**, 1688 (2005).

[137] M. Sharad, C. Augustine, G. Panagopoulos, and K. Roy, *Spin-Based Neuron Model with Domain-Wall Magnets as Synapse*, IEEE Trans Nanotechnol **11**, 843 (2012).

[138] B. Ojha, B. B. Singh, M. Sharma, S. Mallick, V. Jeudy, A. Thiaville, S. Rohart, and S. Bedanta, *Unusual Domain Wall Motion in the Vicinity of the Depinning Field in a Pt/CoFeB/MgO Film*, Applied Physics A **129**, 688 (2023).

[139] A. Thiaville, S. Rohart, É. Jué, V. Cros, and A. Fert, *Dynamics of Dzyaloshinskii Domain Walls in Ultrathin Magnetic Films*, Europhys Lett **100**, 57002 (2012).

[140] S.-G. Je, D.-H. Kim, S.-C. Yoo, B.-C. Min, K.-J. Lee, and S.-B. Choe, *Asymmetric Magnetic Domain-Wall Motion by the Dzyaloshinskii-Moriya Interaction*, Phys Rev B **88**, 214401 (2013).

[141] A. Hrabec, N. A. Porter, A. Wells, M. J. Benitez, G. Burnell, S. McVitie, D. McGrouther, T. A. Moore, and C. H. Marrows, *Measuring and Tailoring the Dzyaloshinskii-Moriya Interaction in Perpendicularly Magnetized Thin Films*, Phys Rev B **90**, 20402 (2014).

[142] P. M. Shepley, H. Tunnicliffe, K. Shahbazi, G. Burnell, and T. A. Moore, *Magnetic Properties, Domain-Wall Creep Motion, and the Dzyaloshinskii-Moriya Interaction in Pt/Co/Ir Thin Films*, Phys Rev B **97**, 134417 (2018).

[143] E. Pandey, B. Ojha, and S. Bedanta, *Emergence of Sizeable Interfacial Dzyaloshinskii-Moriya Interaction at Cobalt/Fullerene Interface*, Phys Rev Appl **19**, 44013 (2023).

[144] H. J. Hug et al., *Quantitative Magnetic Force Microscopy on Perpendicularly Magnetized Samples*, J Appl Phys **83**, 5609 (1998).

[145] P. Grütter, H. J. Mamin, and D. Rugar, *Magnetic Force Microscopy (MFM)*, in *Scanning Tunneling Microscopy II: Further Applications and Related Scanning Techniques* (Springer, 1992), pp. 151–207.

[146] M. R. Koblischka and U. Hartmann, *Recent Advances in Magnetic Force Microscopy*, Ultramicroscopy **97**, 103 (2003).

[147] A. K. Chaurasiya, S. Choudhury, J. Sinha, and A. Barman, *Dependence of Interfacial Dzyaloshinskii-Moriya Interaction on Layer Thicknesses in Ta/Co- Fe- B/TaO x Heterostructures from Brillouin Light Scattering*, Phys Rev Appl **9**, 14008 (2018).

[148] S. Tacchi, R. E. Troncoso, M. Ahlberg, G. Gubbiotti, M. Madami, J. Åkerman, and P. Landeros, *Interfacial Dzyaloshinskii-Moriya Interaction in Pt/CoFeB Films: Effect of the Heavy-Metal Thickness*, Phys Rev Lett **118**, 147201 (2017).

[149] M. Belmeguenai, J.-P. Adam, Y. Roussigné, S. Eimer, T. Devolder, J.-V. Kim, S. M. Cherif, A. Stashkevich, and A. Thiaville, *Interfacial Dzyaloshinskii-Moriya Interaction in Perpendicularly Magnetized Pt/Co/AlO x Ultrathin Films Measured by Brillouin Light Spectroscopy*, Phys Rev B **91**, 180405 (2015).

[150] H. T. Nembach, J. M. Shaw, M. Weiler, E. Jué, and T. J. Silva, *Linear Relation between Heisenberg Exchange and Interfacial Dzyaloshinskii–Moriya Interaction in Metal Films*, Nat Phys **11**, 825 (2015).

[151] *Physical Property Measurement System, Quantum Design PPMS®*, https://www.qdusa.com/products/ppms.html.

[152] D. W. F. James and R. G. Jones, *On the Four-Probe Method of Resistivity Measurement*, J Sci Instrum **42**, 283 (1965).

[153] J. H. Scofield, *Ac Method for Measuring Low-Frequency Resistance Fluctuation Spectra*, Review of Scientific Instruments **58**, 985 (1987).

[154] A. A. Ramadan, R. D. Gould, and A. Ashour, *On the Van Der Pauw Method of Resistivity Measurements*, Thin Solid Films **239**, 272 (1994).

[155] P. M. Hemenger, *Measurement of High Resistivity Semiconductors Using the van Der Pauw Method*, Review of Scientific Instruments **44**, 698 (1973).

[156] S. Lemerle, J. Ferré, C. Chappert, V. Mathet, T. Giamarchi, and P. Le Doussal, *Domain Wall Creep in an Ising Ultrathin Magnetic Film*, Phys Rev Lett **80**, 849 (1998).

[157] M. Müller, D. A. Gorokhov, and G. Blatter, *Velocity-Force Characteristics of a Driven Interface in a Disordered Medium*, Phys Rev B **63**, 184305 (2001).

[158] L. Laurson, X. Illa, S. Santucci, K. Tore Tallakstad, K. J. Måløy, and M. J. Alava, *Evolution of the Average Avalanche Shape with the Universality Class*, Nat Commun **4**, 2927 (2013).

[159] L. B. Ioffe and V. M. Vinokur, *Dynamics of Interfaces and Dislocations in Disordered Media*, Journal of Physics C: Solid State Physics **20**, 6149 (1987).

[160] J. Ferré, P. J. Metaxas, A. Mougin, J.-P. Jamet, J. Gorchon, and V. Jeudy, *Universal Magnetic Domain Wall Dynamics in the Presence of Weak Disorder*, C R Phys **14**, 651 (2013).

[161] C. E. Patton and F. B. Humphrey, *Mobility and Loss Mechanisms for Domain Wall Motion in Thin Ferromagnetic Films*, J Appl Phys **37**, 4269 (1966).

[162] L. D. Landau and E. M. Lifshitz, *ON THE THEORY OF THE DISPERSION OF MAGNETIC PERMEABILITY IN FERROMAGNETIC BODIES*, in (1935).

[163] S. DuttaGupta, S. Fukami, C. Zhang, H. Sato, M. Yamanouchi, F. Matsukura, and H. Ohno, *Adiabatic Spin-Transfer-Torque-Induced Domain Wall Creep in a Magnetic Metal*, Nat Phys **12**, 333 (2016).

[164] D.-H. Kim, S.-B. Choe, and S.-C. Shin, *Direct Observation of Barkhausen Avalanche in Co Thin Films*, Phys Rev Lett **90**, 87203 (2003).

[165] J. Gorchon, S. Bustingorry, J. Ferré, V. Jeudy, A. B. Kolton, and T. Giamarchi, *Pinning-Dependent Field-Driven Domain Wall Dynamics and Thermal Scaling in an Ultrathin Pt/Co/Pt Magnetic Film*, Phys Rev Lett **113**, 27205 (2014).

[166] M. Belmeguenai, J.-P. Adam, Y. Roussigné, S. Eimer, T. Devolder, J.-V. Kim, S. M. Cherif, A. Stashkevich, and A. Thiaville, *Interfacial Dzyaloshinskii-Moriya Interaction in Perpendicularly Magnetized Pt/Co/AlOx Ultrathin Films Measured by Brillouin Light Spectroscopy*, Phys Rev B **91**, 180405 (2015).

[167] S. Tacchi, R. E. Troncoso, M. Ahlberg, G. Gubbiotti, M. Madami, J. Åkerman, and P. Landeros, *Interfacial Dzyaloshinskii-Moriya Interaction in Pt/CoFeB Films: Effect of the Heavy-Metal Thickness*, Phys Rev Lett **118**, 147201 (2017).

[168] K. Di, V. L. Zhang, H. S. Lim, S. C. Ng, M. H. Kuok, X. Qiu, and H. Yang, *Asymmetric Spin-Wave Dispersion Due to Dzyaloshinskii-Moriya Interaction in an Ultrathin Pt/CoFeB Film*, Appl Phys Lett **106**, 52403 (2015).

[169] M. Sinha, R. K. Gupta, P. Dasilva, P. Mercere, and M. H. Modi, *Modification of Optical Properties of Magnesium Oxide (MgO) Thin Film under the Influence of Ambience*, in *AIP Conference Proceedings*, Vol. 2265 (2020).

[170] H. S. Craft, R. Collazo, M. D. Losego, Z. Sitar, and J.-P. Maria, *Surface Water Reactivity of Polycrystalline MgO and CaO Films Investigated Using X-Ray Photoelectron Spectroscopy*, Journal of Vacuum Science & Technology A **26**, 1507 (2008).

[171] E. E. Ferrero, S. Bustingorry, A. B. Kolton, and A. Rosso, *Numerical Approaches on Driven Elastic Interfaces in Random Media*, C R Phys **14**, 641 (2013).

[172] A. Fert, V. Cros, and J. Sampaio, *Skyrmions on the Track*, Nat Nanotechnol **8**, 152 (2013).

[173] D. Mancilla-Almonacid, R. Jaeschke-Ubiergo, A. S. Núñez, and S. Allende, *Ultrafast Domain Wall Propagation Due to the Interfacial Dzyaloshinskii–Moriya Interaction*, Nanotechnology **31**, 125707 (2020).

[174] D. Khadka, S. Karayev, and S. X. Huang, *Dzyaloshinskii–Moriya Interaction in Pt/Co/Ir and Pt/Co/Ru Multilayer Films*, J Appl Phys **123**, (2018).

[175] B.-E. Mokhtari et al., *Interfacial Dzyaloshinskii-Moriya Interaction, Interface-Induced Damping and Perpendicular Magnetic Anisotropy in Pt/Co/W Based Multilayers*, J Appl Phys **126**, (2019).

[176] F. Ajejas, Y. Sassi, W. Legrand, S. Collin, J. P. Garcia, A. Thiaville, S. Pizzini, N. Reyren, V. Cros, and A. Fert, *Interfacial Potential Gradient Modulates Dzyaloshinskii-Moriya Interaction in Pt/Co/Metal Multilayers*, Phys Rev Mater **6**, L071401 (2022).

[177] A. Fakhredine, A. Wawro, and C. Autieri, *Huge Dzyaloshinskii-Moriya Interactions in Re_Co_Pt Thin Films*, ArXiv Preprint ArXiv:2310.03638 (2023).

[178] P. Jadaun, L. F. Register, and S. K. Banerjee, *The Microscopic Origin of DMI in Magnetic Bilayers and Prediction of Giant DMI in New Bilayers*, NPJ Comput Mater **6**, 88 (2020).

[179] A. Nomura, T. Gao, S. Haku, and K. Ando, *Additive Dzyaloshinskii–Moriya Interaction in Pt/Co/Re Films*, AIP Adv **12**, (2022).

[180] A. Cao, R. Chen, X. Wang, X. Zhang, S. Lu, S. Yan, B. Koopmans, and W. Zhao, *Enhanced Interfacial Dzyaloshinskii—Moriya Interactions in Annealed Pt/Co/MgO Structures*, Nanotechnology **31**, 155705 (2020).

[181] A. V Davydenko, A. G. Kozlov, M. E. Stebliy, A. G. Kolesnikov, N. I. Sarnavskiy, I. G. Iliushin, and A. P. Golikov, *Dzyaloshinskii-Moriya Interaction and Chiral Damping Effect in Symmetric Epitaxial Pd/Co/Pd (111) Trilayers*, Phys Rev B **103**, 94435 (2021).

[182] E. Jué et al., *Chiral Damping of Magnetic Domain Walls*, Nat Mater **15**, 272 (2016).

[183] J. P. Pellegren, D. Lau, and V. Sokalski, *Dispersive Stiffness of Dzyaloshinskii Domain Walls*, Phys Rev Lett **119**, 27203 (2017).

[184] D. M. F. Hartmann, R. A. Duine, M. J. Meijer, H. J. M. Swagten, and R. Lavrijsen, *Creep of Chiral Domain Walls*, Phys Rev B **100**, 94417 (2019).

[185] D. Lau, J. P. Pellegren, H. T. Nembach, J. M. Shaw, and V. Sokalski, *Disentangling Factors Governing Dzyaloshinskii Domain-Wall Creep in Co/Ni Thin Films Using Pt x Ir 1- x Seed Layers*, Phys Rev B **98**, 184410 (2018).

[186] A. Fert, N. Reyren, and V. Cros, *Magnetic Skyrmions: Advances in Physics and Potential Applications*, Nat Rev Mater **2**, 1 (2017).

[187] S. Woo et al., *Observation of Room-Temperature Magnetic Skyrmions and Their Current-Driven Dynamics in Ultrathin Metallic Ferromagnets*, Nat Mater **15**, 501 (2016).

[188] Y. Wu et al., *Néel-Type Skyrmion in WTe2/Fe3GeTe2 van Der Waals Heterostructure*, Nat Commun **11**, 3860 (2020).

[189] T. Schulz, R. Ritz, A. Bauer, M. Halder, M. Wagner, C. Franz, C. Pfleiderer, K. Everschor, M. Garst, and A. Rosch, *Emergent Electrodynamics of Skyrmions in a Chiral Magnet*, Nat Phys **8**, 301 (2012).

[190] N. Kanazawa, Y. Onose, T. Arima, D. Okuyama, K. Ohoyama, S. Wakimoto, K. Kakurai, S. Ishiwata, and Y. Tokura, *Large Topological Hall Effect in a Short-Period Helimagnet MnGe*, Phys Rev Lett **106**, 156603 (2011).

[191] S. X. Huang and C. L. Chien, *Extended Skyrmion Phase in Epitaxial FeGe (111) Thin Films*, Phys Rev Lett **108**, 267201 (2012).

[192] P. K. Sivakumar et al., *Topological Hall Signatures of Two Chiral Spin Textures Hosted in a Single Tetragonal Inverse Heusler Thin Film*, ACS Nano **14**, 13463 (2020).

[193] A. Neubauer, C. Pfleiderer, B. Binz, A. Rosch, R. Ritz, P. G. Niklowitz, and P. Böni, *Topological Hall Effect in the A Phase of MnSi*, Phys Rev Lett **102**, 186602 (2009).

[194] A. Mourkas, A. Markou, P. Swekis, and I. Panagiotopoulos, *Topological Hall Effect in Pt/Co/W Multilayers with Different Anisotropies*, J Magn Magn Mater **530**, 167937 (2021).

[195] C. Singh, V. Singh, G. Pradhan, V. Srihari, H. K. Poswal, R. Nath, A. K. Nandy, and A. K. Nayak, *Pressure Controlled Trimerization for Switching of Anomalous Hall Effect in Triangular Antiferromagnet Mn 3 Sn*, Phys Rev Res **2**, 43366 (2020).

[196] Y. Li, L. Zhang, Q. Zhang, C. Li, T. Yang, Y. Deng, L. Gu, and D. Wu, *Emergent Topological Hall Effect in La0. 7Sr0. 3MnO3/SrIrO3 Heterostructures*, ACS Appl Mater Interfaces **11**, 21268 (2019).

[197] A. Vansteenkiste and B. de Wiele, *MuMax: A New High-Performance Micromagnetic Simulation Tool*, J Magn Magn Mater **323**, 2585 (2011).

[198] A. Vansteenkiste, J. Leliaert, M. Dvornik, M. Helsen, F. Garcia-Sanchez, and B. Van Waeyenberge, *The Design and Verification of MuMax3*, AIP Adv **4**, (2014).

[199] P. Li et al., *Topological Hall Effect in a Topological Insulator Interfaced with a Magnetic Insulator*, Nano Lett **21**, 84 (2020).

[200] K. K. Meng et al., *Robust Emergence of a Topological Hall Effect in MnGa/Heavy Metal Bilayers*, Phys Rev B **97**, 60407 (2018).

[201] A. S. Ahmed et al., *Spin-Hall Topological Hall Effect in Highly Tunable Pt/Ferrimagnetic-Insulator Bilayers*, Nano Lett **19**, 5683 (2019).

[202] S. Budhathoki et al., *Room-Temperature Skyrmions in Strain-Engineered FeGe Thin Films*, Phys Rev B **101**, 220405 (2020).

[203] J. Sampaio, V. Cros, S. Rohart, A. Thiaville, and A. Fert, *Nucleation, Stability and Current-Induced Motion of Isolated Magnetic Skyrmions in Nanostructures*, Nat Nanotechnol **8**, 839 (2013).

[204] C. Ma, X. Zhang, J. Xia, M. Ezawa, W. Jiang, T. Ono, S. N. Piramanayagam, A. Morisako, Y. Zhou, and X. Liu, *Electric Field-Induced Creation and Directional Motion of Domain Walls and Skyrmion Bubbles*, Nano Lett **19**, 353 (2018).

[205] R. Tomasello, S. Komineas, G. Siracusano, M. Carpentieri, and G. Finocchio, *Chiral Skyrmions in an Anisotropy Gradient*, Phys Rev B **98**, 24421 (2018).

[206] C. Reichhardt, D. Ray, and C. J. O. Reichhardt, *Collective Transport Properties of Driven Skyrmions with Random Disorder*, Phys Rev Lett **114**, 217202 (2015).

[207] C. Hanneken, A. Kubetzka, K. Von Bergmann, and R. Wiesendanger, *Pinning and Movement of Individual Nanoscale Magnetic Skyrmions via Defects*, New J Phys **18**, 55009 (2016).

[208] J.-V. Kim and M.-W. Yoo, *Current-Driven Skyrmion Dynamics in Disordered Films*, Appl Phys Lett **110**, 132404 (2017).

[209] S. Fukami, T. Suzuki, Y. Nakatani, N. Ishiwata, M. Yamanouchi, S. Ikeda, N. Kasai, and H. Ohno, *Current-Induced Domain Wall Motion in Perpendicularly Magnetized CoFeB Nanowire*, Appl Phys Lett **98**, 82504 (2011).

[210] T. A. Moore, I. M. Miron, G. Gaudin, G. Serret, S. Auffret, B. Rodmacq, A. Schuhl, S. Pizzini, J. Vogel, and M. Bonfim, *High Domain Wall Velocities Induced by Current in Ultrathin Pt/Co/AlOx Wires with Perpendicular Magnetic Anisotropy*, Appl Phys Lett **93**, 262504 (2008).

[211] S. Fukami, Y. Nakatani, T. Suzuki, K. Nagahara, N. Ohshima, and N. Ishiwata, *Relation between Critical Current of Domain Wall Motion and Wire Dimension in Perpendicularly Magnetized Co/Ni Nanowires*, Appl Phys Lett **95**, 232504 (2009).

[212] J. Kanak, P. Wiśniowski, T. Stobiecki, A. Zaleski, W. Powroźnik, S. Cardoso, and P. P. Freitas, *X-Ray Diffraction Analysis and Monte Carlo Simulations of CoFeB-MgO Based Magnetic Tunnel Junctions*, J Appl Phys **113**, 23915 (2013).

[213] T. Huang, X. Cheng, X. Guan, and X. Miao, *Effect of Ultrathin Inserted Ag Layer on Perpendicular Magnetic Anisotropy of CoFeB Thin Film*, IEEE Trans Magn **50**, 1 (2014).

[214] S. Mallick, S. Panigrahy, G. Pradhan, and S. Rohart, *Current-Induced Nucleation and Motion of Skyrmions in Zero Magnetic Field*, Phys Rev Appl **18**, 64072 (2022).

[215] J.-Y. Chauleau, R. Weil, A. Thiaville, and J. Miltat, *Magnetic Domain Walls Displacement: Automotion versus Spin-Transfer Torque*, Phys. Rev. B **82**, 214414 (2010).

[216] J. Torrejon, G. Malinowski, M. Pelloux, R. Weil, A. Thiaville, J. Curiale, D. Lacour, F. Montaigne, and M. Hehn, *Unidirectional Thermal Effects in Current-Induced Domain Wall Motion*, Phys. Rev. Lett. **109**, 106601 (2012).

[217] C. Burrowes et al., *Low Depinning Fields in Ta-CoFeB-MgO Ultrathin Films with Perpendicular Magnetic Anisotropy*, Appl Phys Lett **103**, 182401 (2013).

[218] P. J. Metaxas, J. P. Jamet, A. Mougin, M. Cormier, J. Ferré, V. Baltz, B. Rodmacq, B. Dieny, and R. L. Stamps, *Creep and Flow Regimes of Magnetic Domain-Wall Motion in Ultrathin Pt/Co/Pt Films with Perpendicular Anisotropy*, Phys Rev Lett **99**, 217208 (2007).

[219] J.-P. Tetienne et al., *Nanoscale Imaging and Control of Domain-Wall Hopping with a Nitrogen-Vacancy Center Microscope*, Science (1979) **344**, 1366 (2014).

[220] K.-J. Kim, J.-C. Lee, S.-M. Ahn, K.-S. Lee, C.-W. Lee, Y. J. Cho, S. Seo, K.-H. Shin, S.-B. Choe, and H.-W. Lee, *Interdimensional Universality of Dynamic Interfaces*, Nature **458**, 740 (2009).

[221] G. Yu et al., *Room-Temperature Skyrmion Shift Device for Memory Application*, Nano Lett **17**, 261 (2017).

[222] R. Tolley, S. A. Montoya, and E. E. Fullerton, *Room-Temperature Observation and Current Control of Skyrmions in Pt/Co/Os/Pt Thin Films*, Phys Rev Mater **2**, 44404 (2018).

[223] W. Akhtar et al., *Current-Induced Nucleation and Dynamics of Skyrmions in a Co-Based Heusler Alloy*, Phys Rev Appl **11**, 34066 (2019).

[224] R. Juge et al., *Current-Driven Skyrmion Dynamics and Drive-Dependent Skyrmion Hall Effect in an Ultrathin Film*, Phys Rev Appl **12**, 44007 (2019).

[225] K. Litzius et al., *The Role of Temperature and Drive Current in Skyrmion Dynamics*, Nat Electron **3**, 30 (2020).

[226] B. Ojha, S. Mallick, S. Panigrahy, M. Sharma, A. Thiaville, S. Rohart, and S. Bedanta, *Driving Skyrmions with Low Threshold Current Density in Pt/CoFeB Thin Film*, Phys Scr **98**, 35819 (2023).

[227] L. Rózsa, U. Atxitia, and U. Nowak, *Temperature Scaling of the Dzyaloshinsky-Moriya Interaction in the Spin Wave Spectrum*, Phys Rev B **96**, 94436 (2017).

[228] H. Y. Kwon, K. M. Song, J. Jeong, A.-Y. Lee, S.-Y. Park, J. Kim, C. Won, B.-C. Min, H. J. Chang, and J. W. Choi, *High-Density Néel-Type Magnetic Skyrmion Phase Stabilized at High Temperature*, NPG Asia Mater **12**, 86 (2020).

[229] V. Baltz, A. Marty, B. Rodmacq, and B. Dieny, *Magnetic Domain Replication in Interacting Bilayers with Out-of-Plane Anisotropy: Application to Co/ Pt Multilayers*, Phys Rev B **75**, 14406 (2007).

[230] M. J. Benitez, A. Hrabec, A. P. Mihai, T. A. Moore, G. Burnell, D. McGrouther, C. H. Marrows, and S. McVitie, *Magnetic Microscopy and Topological Stability of Homochiral Néel Domain Walls in a Pt/Co/AlO x Trilayer*, Nat Commun **6**, 8957 (2015).

[231] J. Jiang et al., *Concurrence of Quantum Anomalous Hall and Topological Hall Effects in Magnetic Topological Insulator Sandwich Heterostructures*, Nat Mater **19**, 732 (2020).

[232] A. G. Kozlov, A. G. Kolesnikov, M. E. Stebliy, A. P. Golikov, and A. V Davydenko, *Domain-Period Method for Determination of the Energy of the Dzyaloshinskii-Moriya Interaction in [Co/Pd (111)] 5 Superlattices*, Phys Rev B **102**, 144411 (2020).

[233] A. V Davydenko, A. G. Kozlov, A. G. Kolesnikov, M. E. Stebliy, G. S. Suslin, Y. E. Vekovshinin, A. V Sadovnikov, and S. A. Nikitov, *Dzyaloshinskii-Moriya Interaction in Symmetric Epitaxial [Co/Pd (111)] N Superlattices with Different Numbers of Co/Pd Bilayers*, Phys Rev B **99**, 14433 (2019).